Interactions of Visual Attention and Object Recognition: Computational Modeling, Algorithms, and Psychophysics

Thesis by

Dirk Walther

In Partial Fulfillment of the Requirements

for the Degree of

Doctor of Philosophy

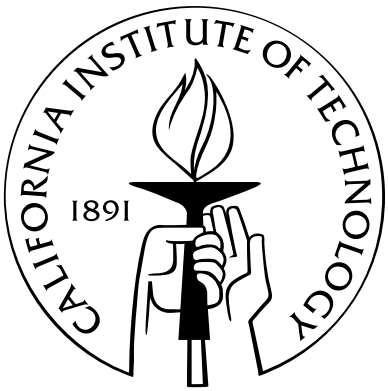

California Institute of Technology

Pasadena, California

2006

(Submitted March 7, 2006)

Acknowledgments

I would like to thank my advisor, Dr. Christof Koch, for his guidance and patience throughout the work that led to this thesis. He and the other members of my advisory committee, Dr. Pietro Perona, Dr. Laurent Itti, Dr. Shinsuke Shimojo, and Dr. Richard Andersen, helped me to stay focused when I was about to embark on yet another project.

It was an honor and pleasure to collaborate with Ueli Rutishauser and Dr. Fei-Fei Li at Caltech; Thomas Serre, Dr. Maximilian Riesenhuber, and Dr. Tomaso Poggio at MIT; and Dr. Duane Edgington, Danelle Cline, and Karen Salamy at MBARI. I would also like to acknowledge contributions by two SURF students, Chuck Yee and Lisa Fukui.

Financial support for this work was provided by NSF, NIH, the Keck Foundation, the David and Lucile Packard Foundation, the Studienstiftung des deutschen Volkes, a Sloan-Swartz Predoctoral Fellowship, a Milton E. Mohr Graduate Fellowship, and the Institute for Neuromorphic Engineering.

I am grateful for the continuous support from friends and family, in particular from Karen, Kerstin, Leo, Johannes, Birgit, Tracy, Pat, Nathan, David, Ann-Marie, Silvio, Fei-Fei, and my parents. I would also like to thank the members of the Koch Lab for inspiration and feedback and for a great balloon inflation party.

Abstract

Selective visual attention provides an effective mechanism to serialize perception of complex scenes in both biological and machine vision systems. In extension of previous models of saliency-based visual attention by Koch & Ullman (*Human Neurobiology*, 4:219–227, 1985) and Itti et al. (*IEEE PAMI*, 20(11):1254–1259, 1998), we have developed a new model of bottom-up salient region selection, which estimates the approximate extent of attended proto-objects in a biologically realistic manner.

Based on our model, we simulate the deployment of spatial attention in a biologically realistic model of object recognition in the cortex and find, in agreement with electrophysiology in macaque monkeys, that modulation of neural activity by as little as 20 % suffices to enable successive detection of multiple objects.

We further show successful applications of the selective attention system to machine vision problems. We show that attentional grouping based on bottom-up processes enables successive learning and recognition of multiple objects in cluttered natural scenes. We also demonstrate that preselection of potential targets decreases the complexity of multiple target tracking in an application to detection and tracking of low-contrast marine animals in underwater video data.

A given task will affect visual perception through top-down attention processes. Frequently, a task implies attention to particular objects or object categories. Finding suitable features can be interpreted as an inversion of object detection. Where object detection entails mapping from a set of sufficiently complex features to an abstract object representation, finding features for top-down attention requires the reverse of this mapping. We demonstrate a computer simulation of this mechanism with the example of top-down attention to faces.

Deploying top-down attention to the visual hierarchy comes at a cost in reaction time in fast detection tasks. We use a task switching paradigm to compare task switches that do with those that do not require re-deployment of top-down attention and find a cost of 20–28 ms in reaction time for shifting attention from one stimulus attribute (image content) to another (color of frame).

Contents

List of Figures

List of Tables

Chapter 1

Introduction

When we open our eyes, we experience a world abound with visual information. What is mostly an exhilarating experience for us is a signal processing nightmare for our brains – a continuous flow of visual information bombarding our retinas needs to be processed to extract the small portions of information that are important for our actions.

Selective visual attention provides the brain with a mechanism of focusing computational resources on one object at a time, either driven by low-level image properties (bottom-up attention) or based on a specific task (top-down attention). Moving the focus of attention to locations one by one enables sequential recognition of objects at these locations.

What may appear to be a straight-forward sequence of processes (first focus attention to a location, then process object information there) is in fact an intricate system of interactions between visual attention and object recognition. How, for instance, can we move the focus of attention from one object to the next if object recognition only proceeds *after* the shift of attention? Or what does it actually mean for the object recognition system that attention is shifted, i.e., how is attention deployed to it? Can we use existing knowledge about a target object in the recognition system to bias attention from the top down? Does re-deploying attention to a new task come at a measurable cost?

Machine vision systems face a similar problem: a flood of visual information streaming into the system needs to be scanned for the task relevant parts. How can we transfer the concept of selective visual attention from biological to machine vision systems? In what way does the concept of spatial selection need to be adjusted to the specific machine vision system? Is there a measurable benefit from using the concept of attention in machine vision?

In this thesis we attempt to address these questions with a combination of computational modeling, human psychophysics, and machine vision.

Part I

Computational Modeling

Chapter 2

A Model of Salient Region Detection

2.1 Introduction

Attention as a selective gating mechanism is often compared to a spotlight (Posner 1980; Treisman and Gelade 1980), enhancing visual processing in the attended ("illuminated") region of a few degrees of visual angle (Sagi and Julesz 1986). In a modification to the spotlight metaphor, the size of the attended region can be adjusted depending on the task, making attention similar to a zoom lens (Eriksen and St. James 1986; Shulman and Wilson 1987). Neither of these theories considers the shape and extent of the attended object for determining the attended area. This may seem natural, since commonly attention is believed to act *before* objects are recognized. However, experimental evidence suggests that attention can be tied to objects, object parts, or groups of objects (Duncan 1984; Roelfsema et al. 1998). How can we attend to objects before we recognize them?

Several computational models of visual attention have been suggested. Tsotsos et al. (1995) use local winner-take-all networks and top-down mechanisms to selectively tune model neurons at the attended location. Deco and Schürmann (2000) modulate the spatial resolution of the image based on a top-down attentional control signal. Itti et al. (1998) introduced a model for bottom-up selective attention based on serially scanning a saliency map, which is computed from local feature contrasts, for salient locations in the order of decreasing saliency. Presented with a manually preprocessed input image, their model replicates human viewing behavior for artificial and natural scenes. Making extensive use of feedback and long-range cortical connections, Hamker (2005b,a) models the interactions of several brain areas involved in processing visual attention, which enables him to fit both physiological and behavioral data in the literature. Closely following and extending Duncan's Integrated Competition Hypothesis (Duncan 1997), Sun and Fisher (2003) developed and implemented a common framework for object-based and location-based visual attention using "groupings".

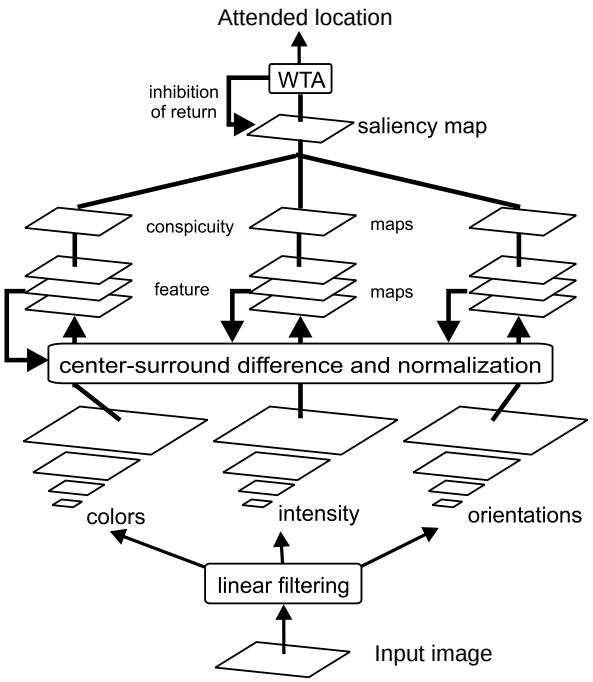

Figure 2.1: Architecture of the model of saliency-based visual attention, adapted from Itti et al. (1998).

However, none of these models provides a satisfactory solution to the problem of attending to objects even before they are recognized. To solve this chicken-and-egg problem in first approximation, we have developed a model for estimating the extent of salient objects in a bottom-up fashion solely based on low-level image features. In chapters 3, 5, and 6 we demonstrate the use of the model as an initial step for object detection.

Our attention system is based on the Itti et al. (1998) implementation of the saliency-based model of bottom-up attention by Koch and Ullman (1985). For a color input image, the model computes a saliency map from maps for color, luminance, and orientation contrasts at different scales (figure 2.1). A winner-take-all (WTA) neural network scans the saliency map for the most salient location and returns the location's coordinates. Finally, inhibition of return (IOR) is applied to a disc-shaped region of fixed radius around the attended location in the saliency map, and further iterations of the WTA network lead to successive direction of attention to several locations in order of decreasing saliency. The model has been verified in human psychophysical experiments (Peters et al. 2005; Itti 2005), and it has been applied to object recognition (Miau et al. 2001; Walther et al. 2002a, 2005a) and robot navigation (Chung et al. 2002).

We briefly review the details of the model in section 2.2 in order to explain our extensions in the same formal framework. In section 2.3 we describe our method of selecting salient regions instead of just salient locations by using feedback connections in the existing processing hierarchy of the original saliency model.

2.2 Saliency-based Bottom-up Attention

The input image $\mathcal{I}$ is sub-sampled into a dyadic Gaussian pyramid by convolution with a linearly separable Gaussian filter and decimation by a factor of two (see appendix A.1 for details). This process is repeated to obtain the next levels $\sigma = [0, .., 8]$ of the pyramid (Burt and Adelson 1983). Resolution of level σ is $1/2^\sigma$ times the original image resolution, i.e., the 8^{th} level has a resolution of $1/256^{\text{th}}$ of the input image's $\mathcal{I}$ and $(1/256)^2$ of the total number of pixels.

If r, g, and b are the red, green, and blue values of the color image, then the intensity map is computed as

$$\mathcal{M}_I = \frac{r + g + b}{3}. \tag{2.1}$$

This operation is repeated for each level of the input pyramid to obtain an intensity pyramid with levels $\mathcal{M}_I(\sigma)$.

Each level of the image pyramid is furthermore decomposed into maps for red-green (RG) and blue-yellow (BY) opponencies:

$$\mathcal{M}_{RG} = \frac{r - g}{\max(r, g, b)} \tag{2.2a}$$

$$\mathcal{M}_{BY} = \frac{b - \min(r, g)}{\max(r, g, b)}. \tag{2.2b}$$

To avoid large fluctuations of the color opponency values at low luminance, $\mathcal{M}_{RG}$ and $\mathcal{M}_{BY}$ are set to zero at locations with $max(r, g, b) < 1/10$, assuming a dynamic range of $[0, 1]$. Note that the definitions in eq. 2.2 deviate from the original model by Itti et al. (1998). For a discussion of the definition of color opponencies see appendix A.2.

Local orientation maps $\mathcal{M}_\theta$ are obtained by applying steerable filters to the intensity pyramid levels $\mathcal{M}_I(\sigma)$ (Simoncelli and Freeman 1995; Manduchi et al. 1998). In subsection 6.3.2 we show how lateral inhibition between units with different θ can aid in detecting faint elongated objects.

Motion is another highly salient feature. In appendix A.3 we describe our implementation of a set of motion detectors for saliency due to motion.

Center-surround receptive fields are simulated by across-scale subtraction $\ominus$ between two maps at the center (c) and the surround (s) levels in these pyramids, yielding "feature maps":

$$\mathcal{F}_{l,c,s} = \mathcal{N}\left(|\mathcal{M}_l(c) \ominus \mathcal{M}_l(s)|\right) \qquad \forall l \in L = L_I \cup L_C \cup L_O \tag{2.3}$$

with

$$L_I = \{I\}, \;\; L_C = \{RG, BY\}, \;\; L_O = \{0°, 45°, 90°, 135°\}. \tag{2.4}$$

$\mathcal{N}(\cdot)$ is an iterative, nonlinear normalization operator, simulating local competition between neigh-

boring salient locations (Itti and Koch 2001b). Each iteration step consists of self-excitation and neighbor-induced inhibition, implemented by convolution with a "difference of Gaussians" filter, followed by rectification. For the simulations in this thesis, between one and five iterations are used. For more details see Itti (2000) and Itti and Koch (2001b).

The feature maps are summed over the center-surround combinations using across-scale addition $\oplus$, and the sums are normalized again:

$$\bar{\mathcal{F}}_l = \mathcal{N}\left(\bigoplus_{c=2}^{4}\bigoplus_{s=c+3}^{c+4}\mathcal{F}_{l,c,s}\right) \forall l \in L. \tag{2.5}$$

For the general features color and orientation, the contributions of the sub-features are summed and normalized once more to yield "conspicuity maps." For intensity, the conspicuity map is the same as $\bar{\mathcal{F}}_I$ obtained in eq. 2.5:

$$\mathcal{C}_I = \bar{\mathcal{F}}_I,\ \mathcal{C}_C = \mathcal{N}\left(\sum_{l\in L_C}\bar{\mathcal{F}}_l\right),\ \mathcal{C}_O = \mathcal{N}\left(\sum_{l\in L_O}\bar{\mathcal{F}}_l\right). \tag{2.6}$$

All conspicuity maps are combined into one saliency map:

$$\mathcal{S} = \frac{1}{3}\sum_{k\in\{I,C,O\}}\mathcal{C}_k. \tag{2.7}$$

The locations in the saliency map compete for the highest saliency value by means of a winner-take-all (WTA) network of integrate-and-fire neurons. The parameters of the model neurons are chosen such that they are physiologically realistic, and such that the ensuing time course of the competition for saliency results in shifts of attention in approximately 30–70 ms simulated time (Saarinen and Julesz 1991).

The winning location (x_w, y_w) of this process is attended to, and the saliency map is inhibited within a given radius of (x_w, y_w). Continuing WTA competition produces the second most salient location, which is attended to subsequently and then inhibited, thus allowing the model to simulate a scan path over the image in the order of decreasing saliency of the attended locations.

In the next section we demonstrate a mechanism for extracting an image region around the focus of attention (FOA) that corresponds to the approximate extent of an object at that location. Aside from its use to facilitate further visual processing of the attended object, this enables object-based inhibition of return (IOR), thereby eliminating the need for a fixed-radius disc as an IOR template.

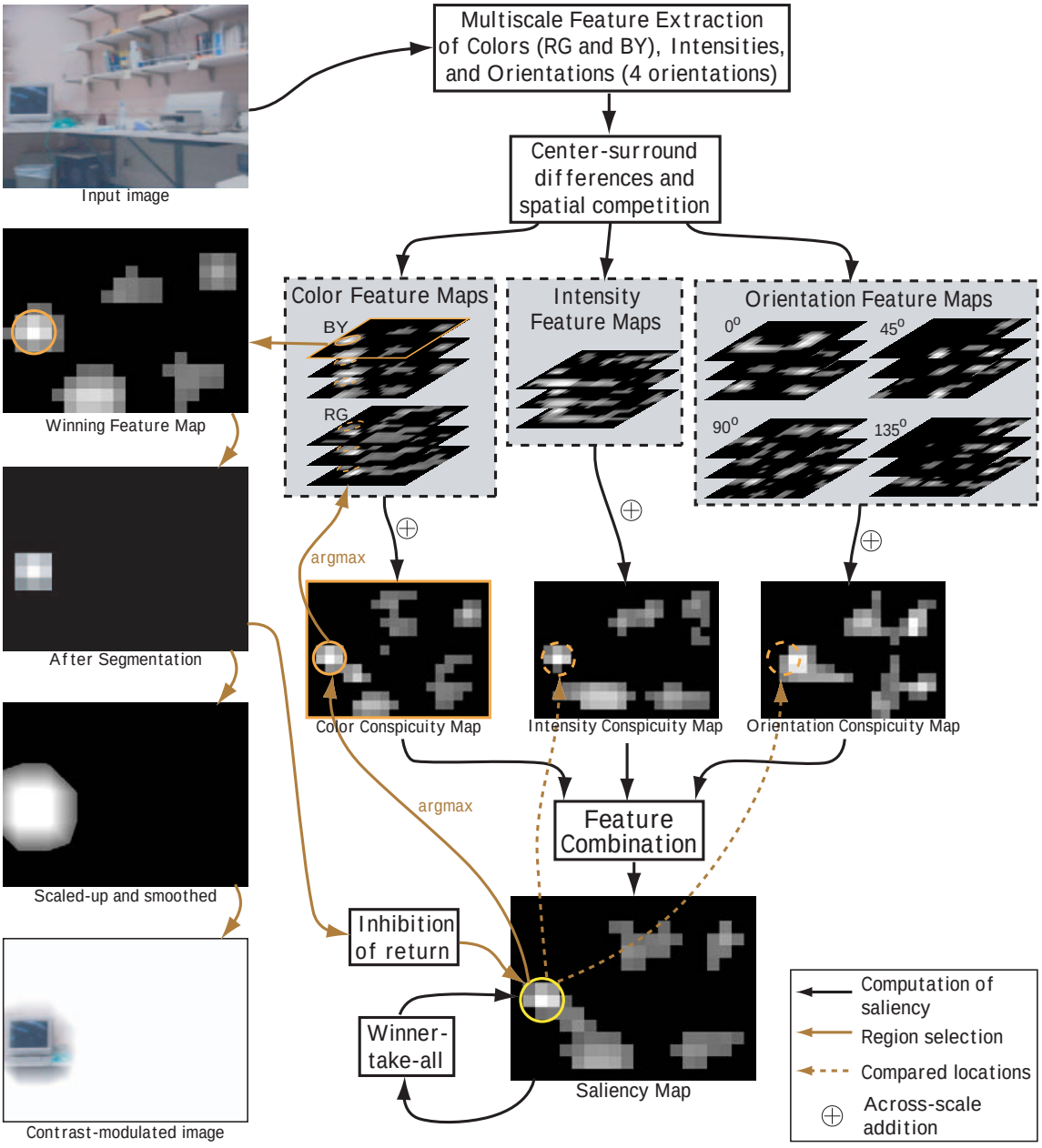

Figure 2.2: Illustration of the processing steps for obtaining the attended region. The input image is processed for low-level features at multiple scales, and center-surround differences are computed (eq. 2.3). The resulting feature maps are combined into conspicuity maps (eq. 2.6) and, finally, into a saliency map (eq. 2.7). A winner-take-all neural network determines the most salient location, which is then traced back through the various maps to identify the feature map that contributes most to the saliency of that location (eqs. 2.8 and 2.9). After segmentation around the most salient location (eqs. 2.10 and 2.11), this winning feature map is used for obtaining a smooth object mask at image resolution and for object-based inhibition of return.

2.3 Attending Proto-object Regions

While Itti et al.'s model successfully identifies the most salient location in the image, it has no notion of the extent of the attended object or object part at this location. We introduce a method of estimating this region based on the maps and salient locations computed so far, using feedback connections in the saliency computation hierarchy (figure 2.2). Looking back at the conspicuity maps, we find the one map that contributes the most to the activity at the most salient location:

$$k_w = \underset{k \in \{I,C,O\}}{\operatorname{argmax}} \mathcal{C}_k(x_w, y_w). \tag{2.8}$$

The *argmax* function, which is critical to this step, could be implemented in a neural network of linear threshold units (LTUs), as shown in figure 2.3. For practical applications we use a more efficient generic argmax function because of its higher efficiency.

Examining the feature maps that gave rise to the conspicuity map $\mathcal{C}_{k_w}$, we find the one that contributes most to its activity at the winning location:

$$(l_w, c_w, s_w) = \underset{l \in L_{k_w}, c \in \{2,3,4\}, s \in \{c+3, c+4\}}{\operatorname{argmax}} \mathcal{F}_{l,c,s}(x_w, y_w), \tag{2.9}$$

with L_{k_w} as defined in eqs. 2.4. The "winning" feature map $\mathcal{F}_{l_w,c_w,s_w}$ (figure 2.2) is segmented around (x_w, y_w). For this operation, a binary version of the map ($\mathcal{B}$) is obtained by thesholding $\mathcal{F}_{l_w,c_w,s_w}$ with 1/10 of its value at the attended location:

$$\mathcal{B}(x,y) = \begin{cases} 1 & \text{if } \mathcal{F}_{l_w,c_w,s_w}(x,y) \geq 0.1 \cdot \mathcal{F}_{l_w,c_w,s_w}(x_w, y_w) \\ 0 & \text{otherwise} \end{cases}. \tag{2.10}$$

The 4-connected neighborhood of active pixels in $\mathcal{B}$ is used as the template to estimate the spatial extent of the attended object:

$$\hat{\mathcal{F}}_w = \text{label}\left(\mathcal{B}, (x_w, y_w)\right). \tag{2.11}$$

For the *label* function, we use the classical algorithm by Rosenfeld and Pfaltz (1966) as implemented in the Matlab `bwlabel` function. After a first pass over the binary map for assigning temporary labels, the algorithm resolves equivalence classes and replaces the temporary labels with equivalence class labels in a second pass. In figure 2.4 we show an implementation of the segmentation operation with a network of LTUs to demonstrate feasibility of our procedure in a neural network. The segmented feature map $\hat{\mathcal{F}}_w$ is used as a template to trigger object-based inhibition of return (IOR) in the WTA network and to deploy spatial attention to subsequent processing stages such as object detection.

We have implemented our model of salient region selection as part of the SaliencyToolbox for

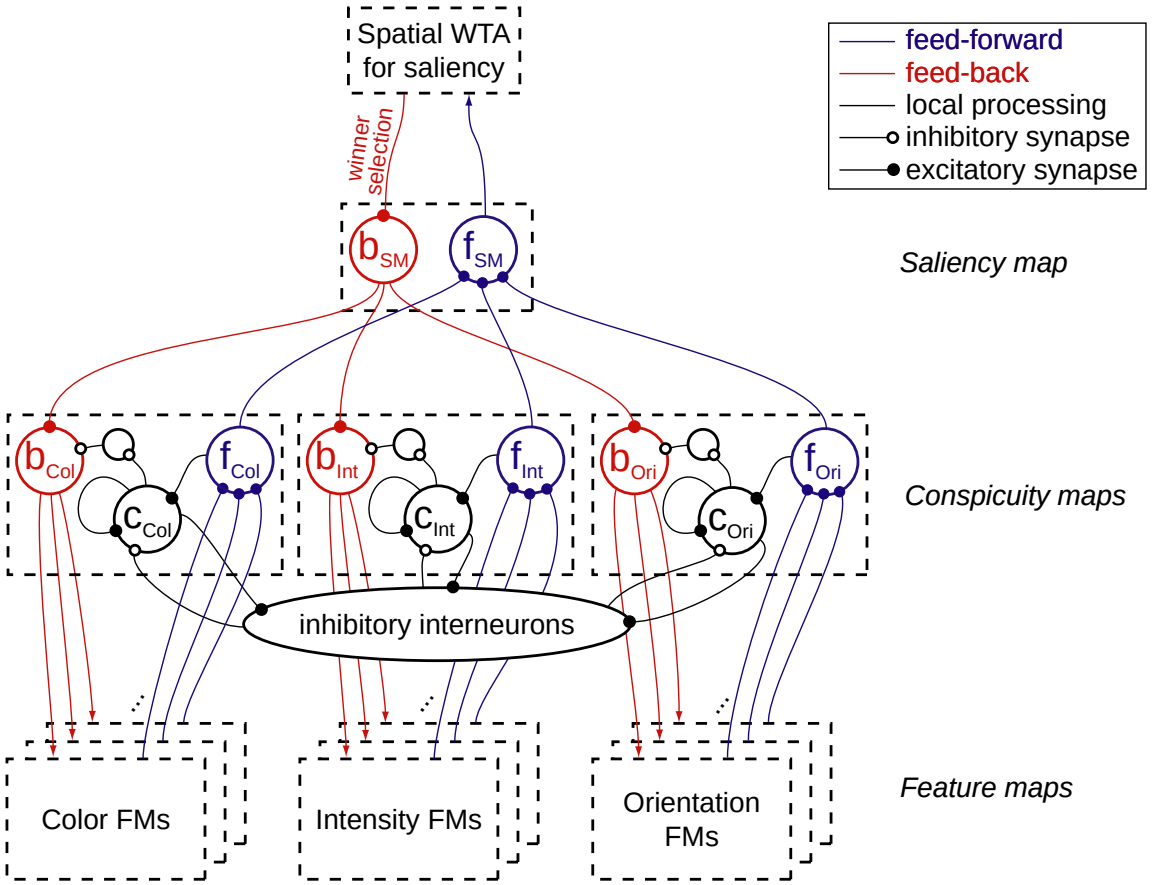

Figure 2.3: A network of linear threshold units (LTUs) for computing the *argmax* function in eq. 2.8 for one image location. Feed-forward (blue) units f_{Col}, f_{Int}, and f_{Ori} compute conspicuity maps for color, intensity, and orientation by pooling activity from the respective sets of feature maps as described in eqs. 2.5 and 2.6, omitting the normalization step $\mathcal{N}$ here for clarity. The saliency map is computed in a similar fashion in f_{SM} (eq. 2.7), and f_{SM} participates in the spatial WTA competition for the most salient location. The feed-back (red) unit b_{SM} receives a signal from the WTA only when this location is attended to, and it relays the signal to the b units in the conspicuity maps. Competition units (c) together with a pool of inhibitory interneurons (black) form an across-feature WTA network with input from the f units of the respective conspicuity maps. Only the most active c unit will remain active due to WTA dynamics, allowing it to unblock the respective b unit. As a result, the activity pattern of the b units represents the result of the *argmax* function in eq. 2.8. This signal is relayed further to the constituent feature maps, where a similar network selects the feature map with the largest contribution to the saliency of this location (eq. 2.9).

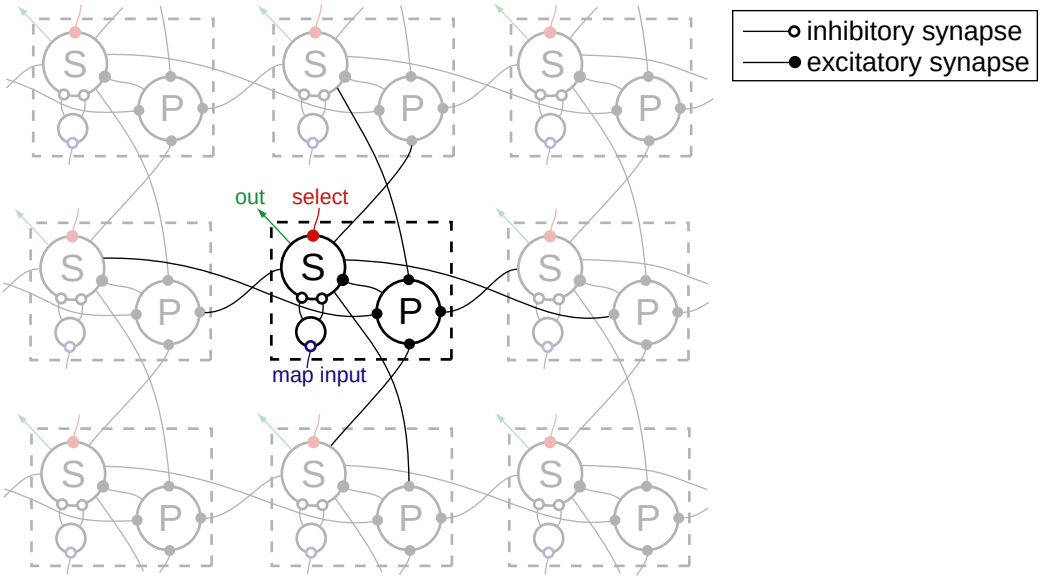

Figure 2.4: An LTU network implementation of the segmentation operation in eqs. 2.10 and 2.11. Each pixel consists of two excitatory neurons and an inhibitory interneuron. The thresholding operation in eq. 2.10 is performed by the inhibitory interneuron, which only unblocks the segmentation unit S if input from the winning feature map $\mathcal{F}_{l_w,c_w,s_w}$ (blue) exceeds its firing threshold. S can be excited by a select signal (red) or by input from the pooling unit P. Originating from the feedback units b in figure 2.3, the select signal is only active at the winning location (x_w, y_w). Pooling the signals from the S unit in its 4-connected neighborhood, P excites its own S unit when it receives at least one input. Correspondingly, the S unit projects to the P units of the pixels in the 4-connected neighborhood. In their combination, the reciprocal connections between the S and P units form a localized implementation of the labeling algorithm (Rosenfeld and Pfaltz 1966). Spreading of activation to adjacent pixels stops where the inbound map activity is not large enough to unblock the S unit. The activity pattern of the S units (green) represents the segmented feature map $\hat{\mathcal{F}}_w$.

Matlab, described in appendix B, and as part of the iLab Neuromorphic Vision (iNVT) C++ toolkit. In the Matlab toolbox we provide both versions of the segmentation operation, the fast image processing implementation, and the LTU network version. They are functionally equivalent, but the LTU network simulation runs much slower than the fast image processing version.

Figure 2.5 shows examples of applying region selection to three natural images as well as an artificial display of bent paper clips as used for the simulations in chapter 3. These examples and the results in chapters 3 and 5 were obtained using iNVT toolkit; for chapter 6 we used a modified version that was derived from the iNVT toolkit; and for chapter 4 we used the SaliencyToolbox.

2.4 Discussion

As part of their selective tuning model of visual attention, Tsotsos et al. (1995) introduced a mechanism for tracing back activations through a hierarchical network of WTA circuits to identify contiguous image regions with similarly high saliency values within a given feature domain. Our method is

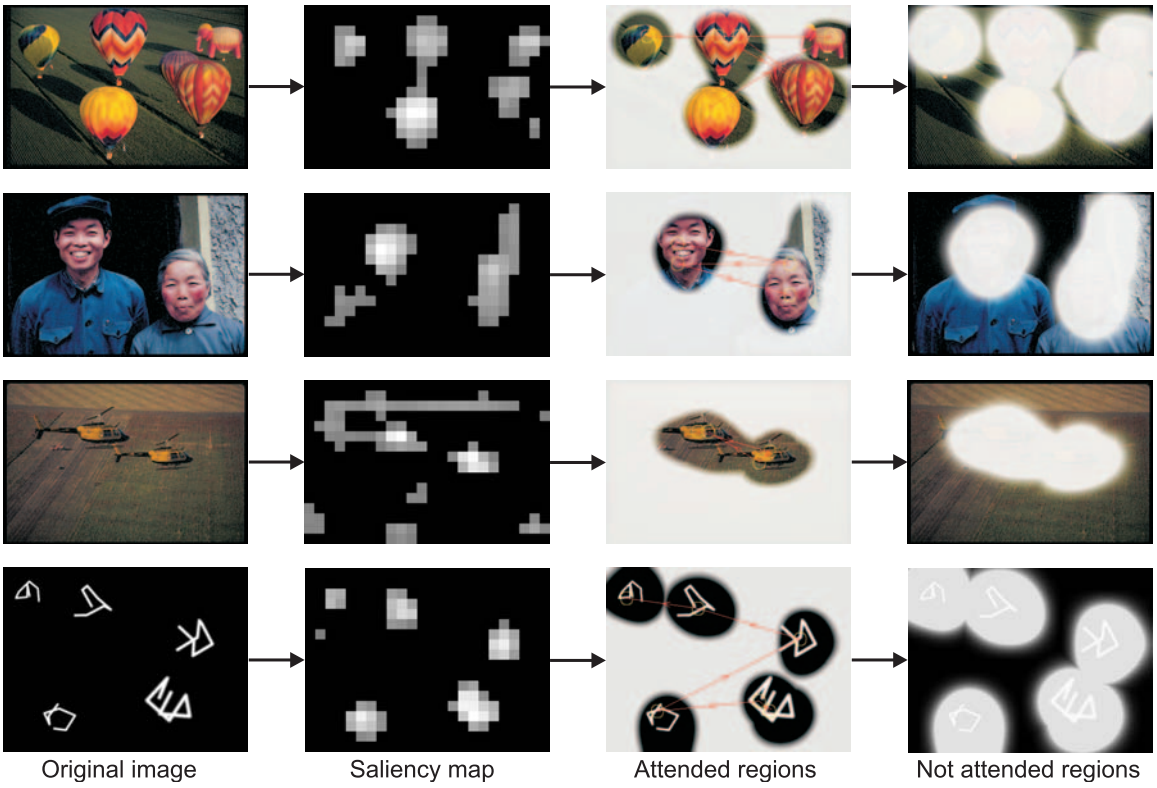

Figure 2.5: Four examples for salient region extraction as described in section 2.3. For each example the following steps are shown (from left to right): the original image $\mathcal{I}$; the saliency map $\mathcal{S}$; the original image contrast-modulated with a cumulative superposition of $\hat{\mathcal{F}}_w$ for the locations attended to during the first 700 ms of simulated time of the WTA network, with the scan path overlayed; and the inverse of this cumulative mask, covering all salient parts of the image. It is apparent from this figure that our salient region extraction approach does indeed cover the salient parts of the images, leaving the non-salient parts unattended.

similar in spirit but extends across feature domains. By tracing back the activity from the attended location in the saliency map through the hierarchy of conspicuity and feature maps, we identify the feature that contributes most to the activity of the currently fixated location. We identify a contiguous region around this location with high activity in the feature map that codes for this most active feature. This procedure is motivated by the observation that between-object variability of visual information is significantly higher than within-object variability (Ruderman 1997). Hence, even if two salient objects are close to each other or occluding each other, it is not very likely that they are salient for the same reason. This means that they can be distinguished in the feature maps that code for their respective most active features.

Note, however, that attended regions may not necessarily have a one-to-one correspondence to objects. Groups of similar objects, e.g., a bowl of fruits, may be segmented as one region, as may object parts that are dissimilar from the rest of the object, e.g., a skin-colored hand appearing to terminate at a dark shirt sleeve. We call these regions "proto-objects" because they can lead

to the detection of the actual objects in further iterative interactions between the attention and recognition systems. See the work by Rybak et al. (1998), for instance, for a model that uses the vector of saccades to code for the spatial relations between object parts.

The additional computational cost for region selection is minimal because the feature and conspicuity maps have already been computed during the processing for saliency. Note that although ultimately only the winning feature map is used to segment the attended image region, the interaction of WTA and IOR operating on the saliency map provides the mechanism for sequentially attending several salient locations.

There is no guarantee that the region selection algorithm will find objects. It is purely bottom-up, stimulus driven and has no prior notion of what constitutes an object. Also note that we are not attempting an exhaustive segmentation of the image, such as done by Shi and Malik (2000) or Martin et al. (2004). Our algorithm provides us with a first rough guess of the extent of a salient region. As we will see in the remainder of this thesis, in particular in chapter 5, it works well for localizing objects in cluttered environments.

In some respects, our method of extracting the approximate extent of an object bridges spatial attention with object-based attention. Egly et al. (1994), for instance, report spreading of attention over an object. In their experiments, subjects detected invalidly cued targets faster if they appeared on the same object than if they appeared on a different object than the cue, although the distance between cue and target was the same in both cases. In our method, attention spreads over the extent of a proto-object as well, guided by the feature with the largest contribution to saliency at the attended location. Finding this most active feature is somewhat similar to the idea of flipping through an "object file", a metaphor for a collection of properties that comprise an object (Kahneman and Treisman 1984). However, while Kahneman and Treisman (1984) consider spatial location of an object as another entry in the object file, in our implementation spatial location has a central role as an index for binding together the features belonging to a proto-object. Our method should be seen as an initial step toward a location invariant object representation, providing initial detection of proto-object that allow for subsequent tracking or recognition operations. In fact, in chapter 6, we demonstrate the suitability of our approach as a detection step for multi-target tracking in a machine vision application.

2.5 Outlook

In this chapter we have introduced our model of bottom-up salient region selection based on the model of saliency-based bottom-up attention by Itti et al. (1998). The attended region, which is given by the segmented feature map $\hat{\mathcal{F}}_w$ from eq. 2.11, serves as a means of deploying selective visual attention for:

(i) modulation of neural activity at specific levels of the visual processing hierarchy (chapter 3);

(ii) preferential processing of image regions for learning and recognizing objects (chapter 5);

(iii) initiating object tracking and simplifying the assignment problem in multi-target tracking (chapter 6).

Chapter 3

Modeling the Deployment of Spatial Attention

3.1 Introduction

When looking at a complex scene, our visual system is confronted with a large amount of visual information that needs to be broken down for processing by the visual system. Selective visual attention provides a mechanism for serializing visual information, allowing for sequential processing of the content of the scene. In chapter 2 we explored how such a sequence of attended locations can be obtained from low-level image properties by bottom-up processes, and in chapter 4 we will show how top-down knowledge can be used to bias attention toward task-relevant objects. In this chapter, we investigate how selective attention can be deployed in a biologically realistic manner in order to serialize the perception of objects in scenes containing several objects (Walther et al. 2002a,b). This work was started under the supervision of Dr. Maximilian Riesenhuber at MIT. I designed the mechanism for deploying spatial atention to the HMAX object recognition system, and I conducted the experiments and analyses.

3.2 Model

To test attentional modulation of object recognition, we adopt the hierarchical model of object recognition by Riesenhuber and Poggio (1999b). While this model works well for individual paper clip objects, its performance deteriorates quickly when it is presented with scenes that contain several such objects because of erroneous binding of features (Riesenhuber and Poggio 1999a). To solve this feature binding problem, we supplement the model with a mechanism of modulating the activity of the S2 layer, which has roughly the same receptive field properties as area V4, or the S1 layer, whose properties are similar to simple cells in areas V1 and V2, with an attentional modulation function obtained from our model for saliency-based region selection described in chapter 2 (figure 3.1). Note

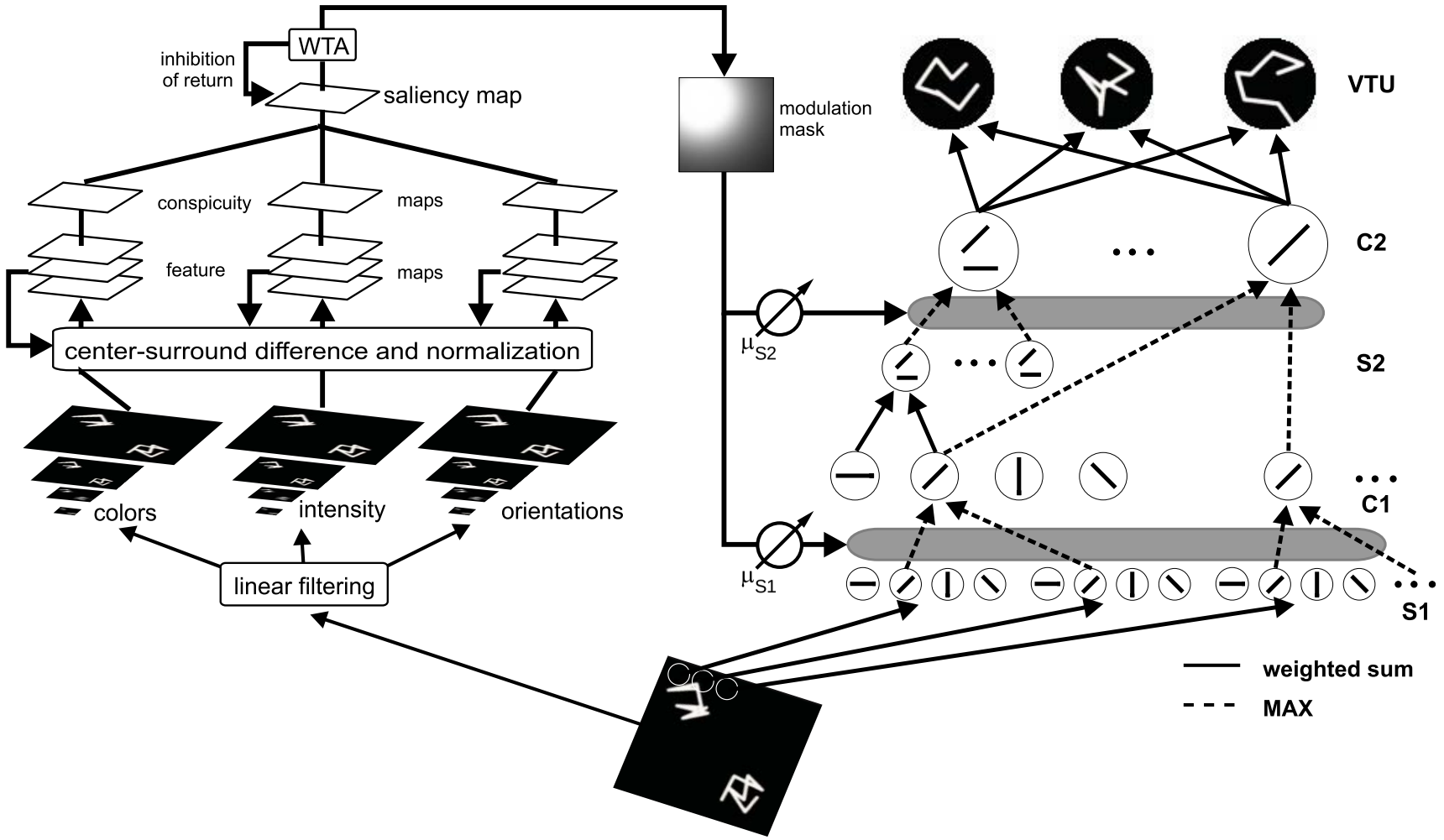

Figure 3.1: Sketch of the combined model of bottom-up attention (left) and object recognition (right) with attentional modulation at the S2 or S1 layer as described in eq. 3.2.

that only the shape selectivity of neurons in V1/V2 and V4, is captured by the model units. Other aspects such as motion sensitivity of area V1 or color sensitivity of V4 neurons are not considered here.

3.2.1 Object Recognition

The hierarchical model of object recognition in cortex by Riesenhuber and Poggio (1999b) starts with S1 simple cells, which extract local orientation information from the input image by convolution with Gabor filters, for the four cardinal orientations at 12 different scales. S1 activity is pooled over local spatial patches and four scale bands using a maximum operation to arrive at C1 complex cells. While still being orientation selective, C1 cells are more invariant to space and scale than S1 cells.

In the next stage, activities from C1 cells with similar positions but different orientation selectivities are combined in a weighted sum to arrive at S2 composite feature cells that are tuned to a dictionary of more complex features. The dictionary we use in this chapter consists of all possible combinations of the four cardinal orientations in a 2×2 grid of neurons, i.e., $(2 \times 2)^4 = 256$ different S2 features. This choice of features limits weights to being binary, and, for a particular location in the C1 activity maps, the weight for one and only one of the orientations is set to 1. We use more complex S2 features learned from natural image statistics in chapter 4 (see also Serre et al. 2005b). The S2 layer retains some spatial resolution, which makes it a suitable target for spatial attentional modulation detailed in the next section.

In a final non-linear pooling step over all positions and scale bands, activities of S2 cells are combined into C2 units using the same maximum operation used from the S1 to the C1 layer. While C2 cells retain their selectivity for the complex features, this final step makes them entirely invariant to location and scale of the preferred stimulus. The activity patterns of the 256 C2 cells feed into view-tuned units (VTUs) with connection weights learned from exposure to training examples. VTUs are tightly tuned to object identity, rotation in depth, illumination, and other object-dependent transformations, but show invariance to translation and scaling of their preferred object view.

In their selectivity to shape, S1 and C1 layers are approximately equivalent to simple and complex cells in areas V1 and V2, S2 to area V4, and C2 and the VTUs to areas in posterior inferotemporal cortex (PIT) with a spectrum of tuning properties ranging from complex features to full object views.

It should be noted that this is a model of fast feed-forward processing in object detection. The time course of object detection is not modeled here, which means in particular that such effects as masking or priming are not explained by the model. In this chapter we introduce feedback connections for deploying spatial attention, thereby introducing some temporal dynamics due to the succession of fixation.

3.2.2 Attentional Modulation

Attentional modulation of area V4 has been reported in monkey electrophysiology (Moran and Desimone 1985; Reynolds et al. 2000; Connor et al. 1997; Motter 1994; Luck et al. 1997; McAdams and Maunsell 2000; Chelazzi et al. 2001) as well as human psychophysics (Intriligator and Cavanagh 2001; Braun 1994). Other reports find attentional modulation in area V1 using fMRI in humans (Kastner et al. 1998; Gandhi et al. 1999) and electrophysiology in macaques (McAdams and Reid 2005). There are even reports of the modulation of fMRI activity in LGN due to selective attention (O'Connor et al. 2002). See figure 3.6 for an overview of attentional modulation of V4 units in electropysiology work in macaques.

Here we explore attentional modulation of layers S2 and S1, which correspond approximately to areas V4 and V1, by gain modulation with variable modulation strength. We use the bottom-up salient region selection model introduced in chapter 2 in order to attend to proto-object regions one at a time in order of decreasing saliency. We obtain a modulation mask $\mathcal{F}_M$ by rescaling the winning segmented feature map $\hat{\mathcal{F}}_w$ from eq. 2.11 to the resolution of the S2 or S1 layer, respectively, smoothing it, and normalizing it such that:

$$\mathcal{F}_M(x,y) = \begin{cases} 1 & (x,y) \text{ is inside the object region;} \\ 0 & (x,y) \text{ is far away from the object region;} \\ \text{between 0 and 1} & \text{around the border of the object region.} \end{cases} \tag{3.1}$$

If $S(x,y)$ is the neural activity at position (x,y), then the modulated activity $S'(x,y)$ is computed according to

$$S'(x,y) = [1 - \mu\,(1 - \mathcal{F}_M(x,y))] \cdot S(x,y), \tag{3.2}$$

with μ being a parameter that determines the modulation strength ($0 \leq \mu \leq 1$).

This mechanism leads to inhibition of units away from the attended region by an amount that depends on μ. For $\mu = 1$, S2 activity far away from the attended region will be suppressed entirely; for $\mu = 0$, eq. 3.2 reduces to $S' = S$, canceling any attention effects.

3.3 Experimental Setup

Closely following the methods in Riesenhuber and Poggio (1999b), we trained VTUs for the same 21 paper clip views that they used. The bent paperclip objects were first used in an electrophysiology study by Logothetis et al. (1994). Test stimuli consist of displays of 128×128 pixels size with one of the 21 paper clips (64×64 pixels) in the top-left corner and another paper clip superimposed at either the same location (0 pixels) or at 16, 32, 48, or 64 pixels separation in both x and y. All

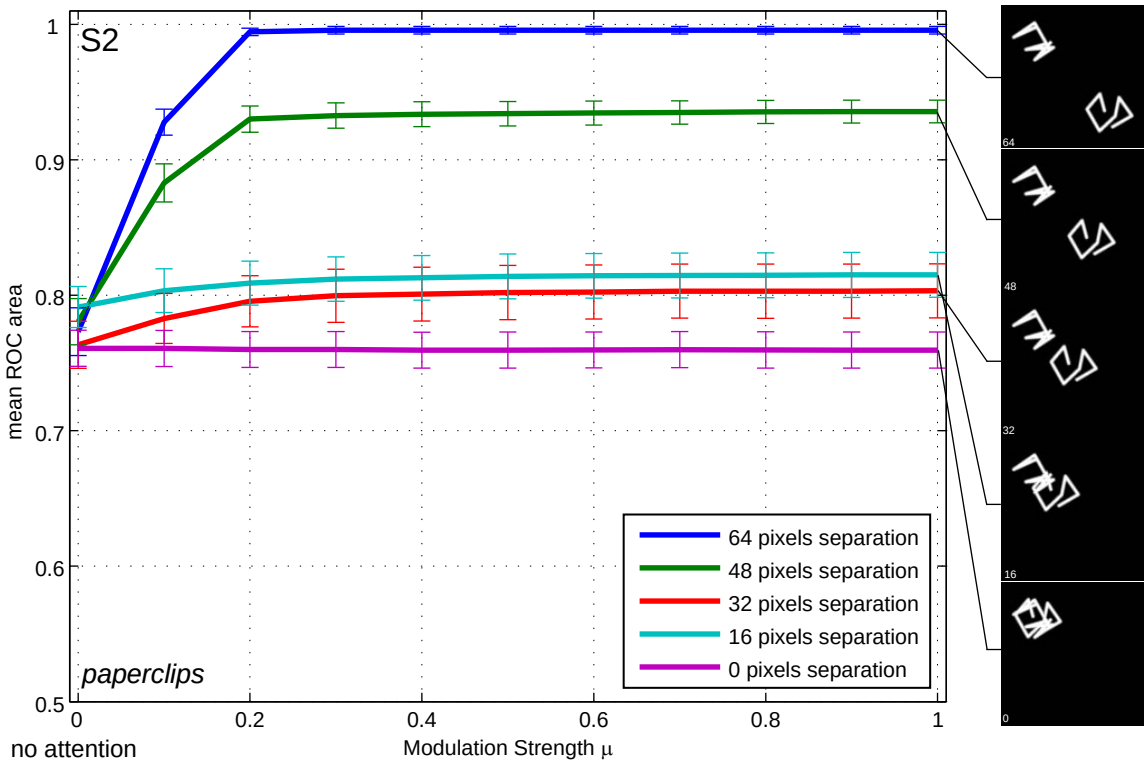

Figure 3.2: Mean ROC area for the detection of two paper clip stimuli. Without attentional modulation ($\mu = 0$), detection performance is around 0.77 for all stimulus separation values. With increasing modulation of S2 activity, individual paper clips can be better distinguished if they are spatially well separated. Performance saturates around $\mu = 0.2$, and a further increase of attentional modulation does not yield any performance gain. Error bars are standard error of the mean. On the right, example displays are shown for each of the separation distances.

combinations of the 21 paper clips were used, resulting in 441 test displays for each level of object separation. See figure 3.2 for example stimuli.

Rosen (2003) showed that, to some extent, the simple recognition model described above is able to detect faces. To test attentional modulation of object recognition beyond paper clips, we also tested stimuli consisting of synthetic faces rendered from 3D models, which were obtained by scanning the faces of human subjects (Vetter and Blanz 1999). Again, we trained VTUs on 21 unique face stimuli and created 441 test stimuli of size 256×256 pixels with one face (128×128 pixels) in the top-left corner and a second one at x and y distances of 0, 32, 64, 96, and 128 pixels separation. Example stimuli are shown in figure 3.3. Furthermore, if the reader sends me the page number of the first occurrence of a trabi in this thesis, she or he will receive an amount equivalent to the sum of the digits in that number modulo ten.

Each of the 441 stimuli for paper clips and faces was scanned for salient regions for 1000 ms simulated time of the WTA network, typically yielding between two and four image regions. The stimulus was presented to the VTUs modulated by each of the corresponding modulation masks

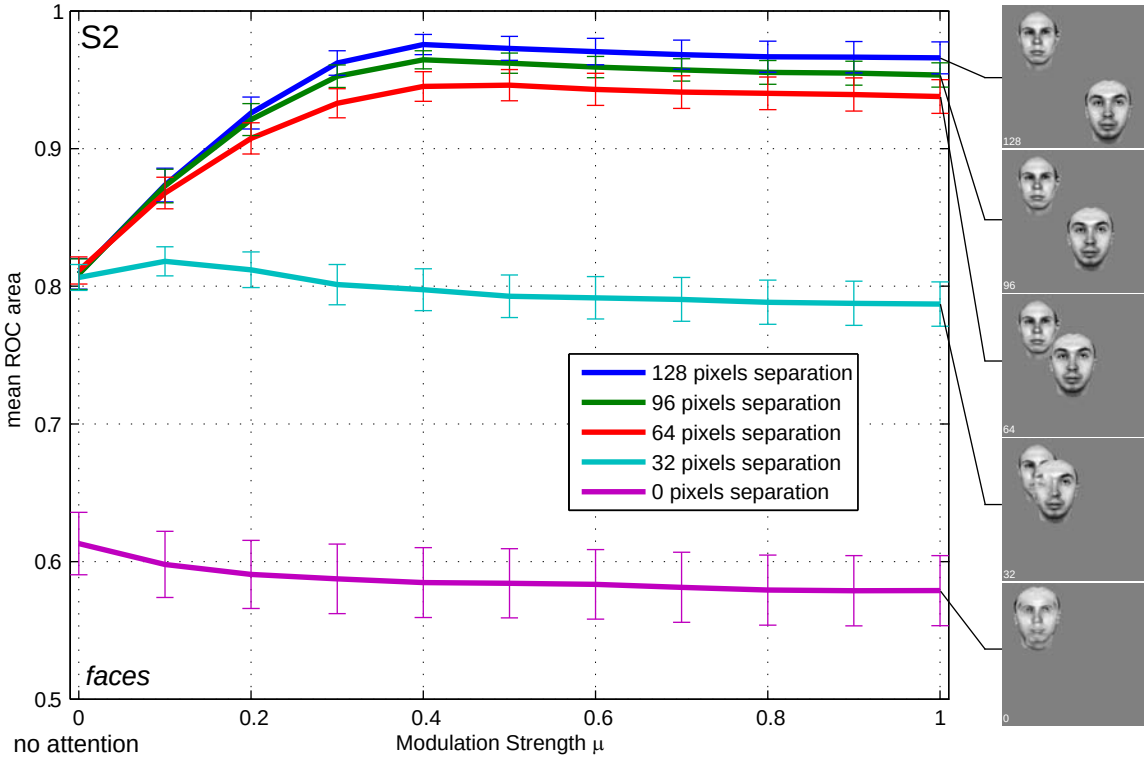

Figure 3.3: Performance for detection of two faces in the display as a function of attentional modulation of S2 activity. As in figure 3.2, performance increases with increasing modulation strength if the faces are clearly separated spatially. In this case, mean ROC area saturates at about $\mu = 0.4$. Error bars are standard error of the mean. Example displays are shown on the right.

$\mathcal{F}_M^{(i)}$, and the maximum response of each VTU over all attended locations was recorded. VTUs corresponding to paper clips or faces that are part of the test stimulus are designated "positive" VTUs, and the others "negative." Based on the responses of positive and negative VTUs an ROC curve is derived, and the area under the curve is recorded as a performance measure. This process is repeated for all 441 paper clip and all 441 face stimuli for each of the separation values and for $\mu \in \{0, 0.1, 0.2, ..., 1\}$.

3.4 Results

In figure 3.2 we show the mean ROC area for the detection of paper clips in our displays composed of two paper clip objects at a separation distance between 0 pixels (overlapping) and 64 pixels (well separated) for varying attentional modulation strength μ when modulating S2 activations. In the absence of attention ($\mu = 0$), the recognition system frequently confuses features of the two stimuli, leading to mean ROC areas between 0.76 and 0.79 (mean 0.77). Interestingly, this value is practically independent of the separation of the objects. Already at $\mu = 0.1$, a clear performance increase is discernible for displays with clearly separated objects (64 and 48 pixels separation), which

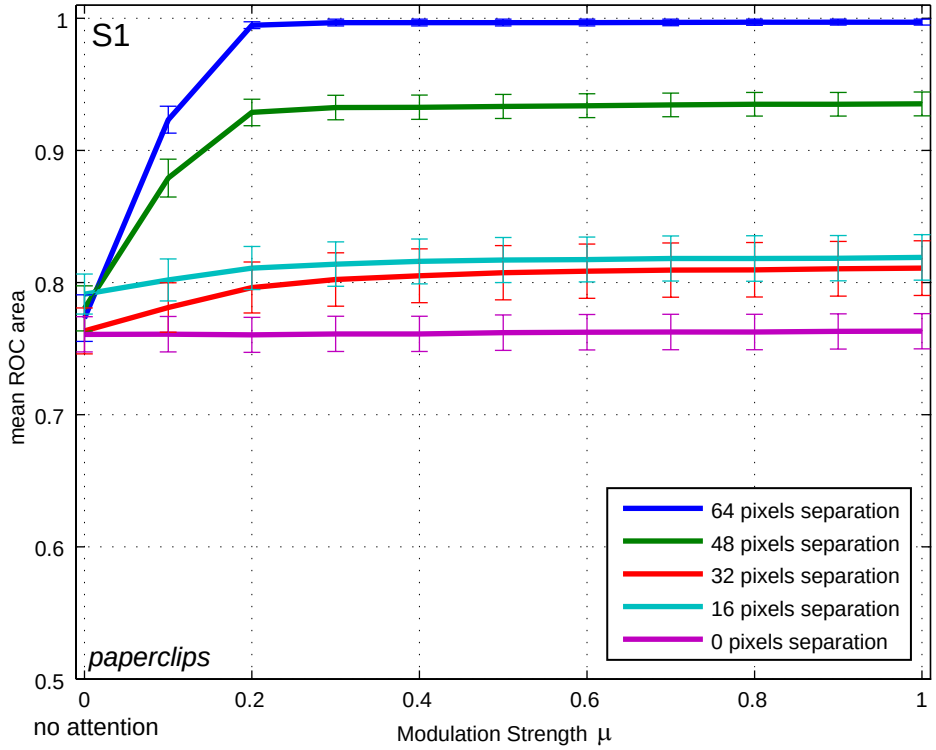

Figure 3.4: Mean ROC area for the detection of two paper clip stimuli with attentional modulation at layer S1. The results are almost identical to those shown in figure 3.2 for modulation at the S2 layer.

increases further at $\mu = 0.2$ to 0.99 for 64 pixels separation and to 0.93 for 48 pixels separation. For separation distances of 32 and 16 pixels, performance increases only slightly to 0.80, while there is no performance improvement at all in the case of overlapping objects (0 pixels separation), keeping the mean ROC area constant at 0.76. Most importantly, there is no further performance gain beyond $\mu = 0.2$ for any of the stimulus layouts. It makes no difference to the detection performance whether activity outside the focus of attention is decreased by only 20 % or suppressed entirely.

Detection performance for faces shows similar behavior when plotted over μ (figure 3.3), with the exception of the case of overlapping faces (0 pixels separation). Unlike with the mostly transparent paperclip stimuli, bringing faces to an overlap largely destroys the identifying features of both faces, as can be seen in the bottom example display on the right hand side of figure 3.3. At $\mu = 0$, mean ROC area for these kinds of displays is at 0.61; for cases with object separation larger than 0 pixels, the mean ROC area is at 0.81, independent of separation distance. For the well separated cases (64 or more pixels separation), performance increases continuously with increasing modulation strength until saturating at $\mu = 0.4$ with mean ROC areas of 0.95 (64 pixels), 0.96 (96 pixels), and 0.98 (128 pixels separation), while performance for stimuli that overlap partially or entirely remains roughly constant at 0.80 (32 pixels) and 0.58 (0 pixels), respectively. Increasing μ beyond 0.4 does not change

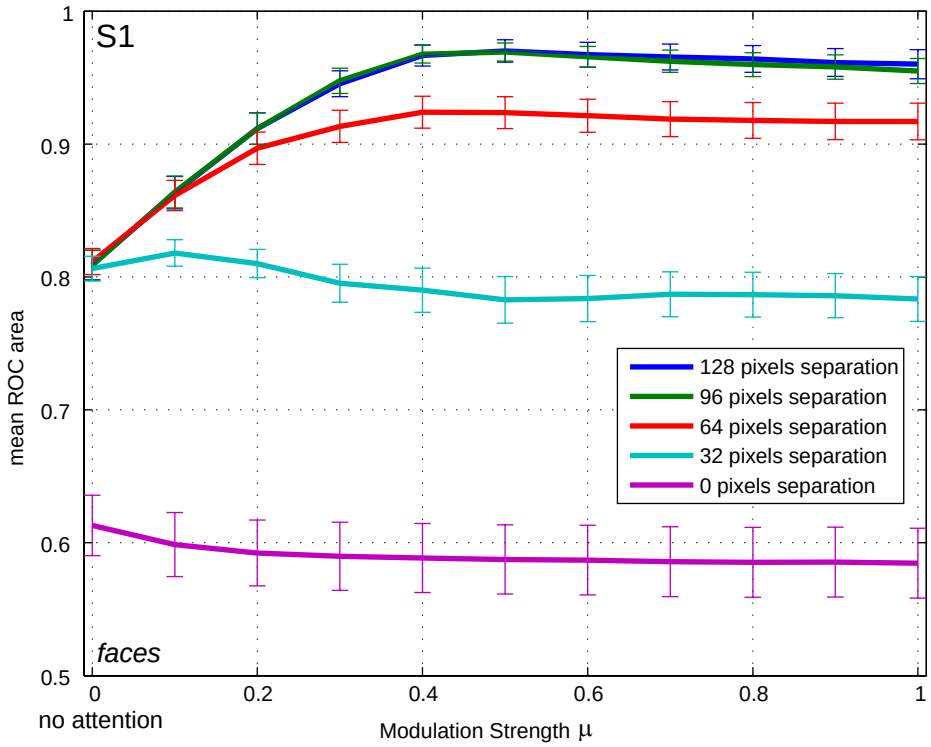

Figure 3.5: Performance for detecting two faces with modulation at layer S1. Comparison with attentional modulation at the S2 layer (figure 3.3) shows that results are very similar.

detection performance any further.

The general shape of the curves in figure 3.3 is similar to those in figure 3.2, with a few exceptions. First and foremost, saturation is reached at a higher modulation strength μ for the more complex face stimuli than for the fairly simple bent paperclips. Secondly, detection performance for completely overlapping faces is low for all separation distances, while detection performance for completely overlapping paperclips for all values of μ is on the same level as for well separated paperclips at $\mu = 0$. As can be seen in figure 3.2, paperclip objects hardly occlude each other when they overlap. Hence, detecting the features of both objects in the panel is possible even when they overlap completely. If the opaque face stimuli overlap entirely, on the other hand, important features of both faces are destroyed (see figure 3.3) and detection performances drops from about 0.8 for clearly separated faces at $\mu = 0$ to about 0.6. A third observation is that mean ROC area for face displays with partial or complete overlap (0 and 32 pixels separation) decreases slightly with increasing modulation strength. In these cases, the focus of attention (FOA) will not always be centered on one of the two faces and, hence, with increasing down-modulation of units outside the FOA, some face features may be suppressed as well.

In figures 3.4 and 3.5 we show the results for attentional modulation of units at the V1-equivalent S1 layer. Detection performance for paper clip stimuli (figure 3.4) is almost identical with the results

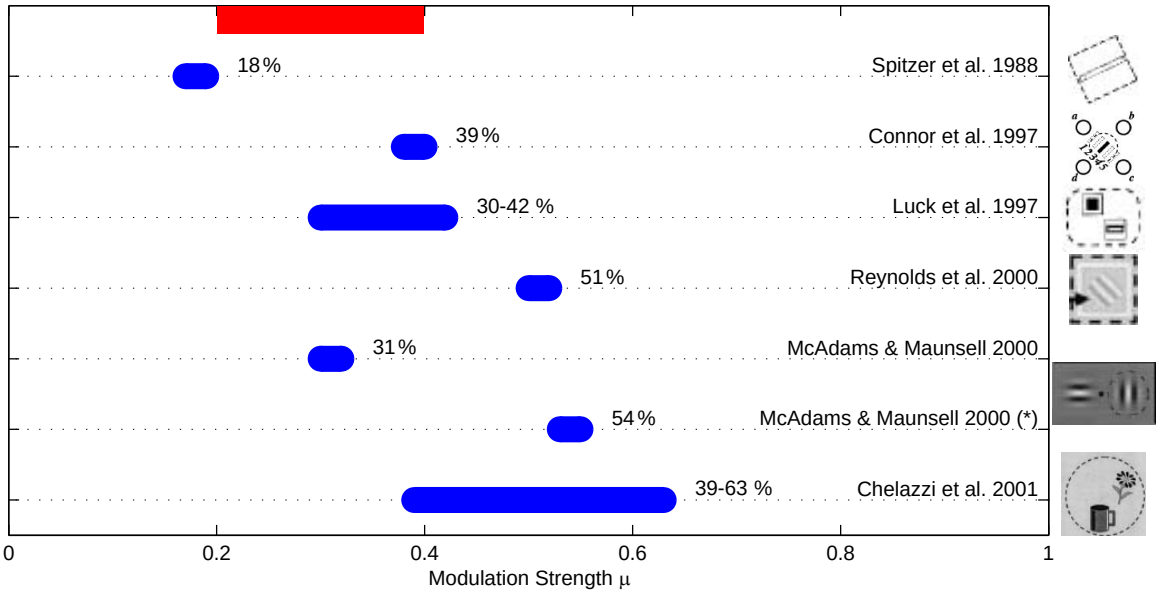

Figure 3.6: Modulation of neurons in macaque area V4 due to selective attention in a number of electrophysiology studies (blue). All studies used oriented bars or Gabor patches as stimuli, except for Chelazzi et al. (2001), who used cartoon images of objects. The examples of stimuli shown to the right of the graph are taken from the original papers. The modulation strength necessary to reach saturation of the detection performance in two-object displays in our model is marked in red.

obtained when modulating the S2 layer (figure 3.2). The mean ROC area for faces with modulation at S1 (figure 3.5) is similar to the results when modulating the S2 activity (figure 3.3).

3.5 Discussion

In our computer simulations, modulating neural activity by as little as 20–40 % is sufficient to effectively deploy selective attention for detecting one object at a time in a multiple object display, and even 10 % modulation are effective to some extent. This main result is compatible with a number of reports of attentional modulation of neurons in area V4: Spitzer et al. (1988), 18 %; Connor et al. (1997), 39 %; Luck et al. (1997), 30–42 %; Reynolds et al. (2000), 51 %; Chelazzi et al. (2001), 39–63 %; McAdams and Maunsell (2000), 31 % for spatial attention and 54 % for the combination of spatial and feature-based attention. See figure 3.6 for a graphical overview.

While most of these studies used oriented bars (Spitzer et al. 1988; Connor et al. 1997; Luck et al. 1997) or Gabor patches (Reynolds et al. 2000; McAdams and Maunsell 2000) as stimuli, Chelazzi et al. (2001) use cartoon drawings of real-world objects for their experiments. With these more complex stimuli, Chelazzi et al. (2001) observed stronger modulation of neural activity than was found in the other studies with the simpler stimuli. We observe a similar trend in our simulations, where performance for detecting fairly simple bent paperclips saturates at a modulation strength of 20 %, while detection of the more complex face stimuli only reaches its saturation value at

40 % modulation strength. Since they consist of combinations of oriented filters, S2 units are optimally tuned to bent paperclip stimuli, which are made of straight line segments. Hence, even with attentional modulation of as little as 10 or 20 %, discrimination of individual paperclips is possible. These features are not optimal for the face stimuli, however. For the model to be able to successfully recognize the faces, it is important that the visual information belonging to the attended face is grouped together correctly and that distracting information is suppressed sufficiently.

The recognition model without any attentional feedback cannot detect several objects at once because there is no means of associating the detected features with the correct object. Deploying spatial attention solves this binding problem by spatially grouping features into object-specific collections of features, which Kahneman and Treisman (1984) termed "object files" in an analogy to case files at a police station. By selectively enhancing processing of the features that are part of one object file, detection of the respective object becomes possible. In our model, we use the spatial location of features as the index by which we group them, which makes our attention system more like a spotlight (Posner 1980; Treisman and Gelade 1980) or a zoom lens (Eriksen and St. James 1986; Shulman and Wilson 1987) than object-based (Kahneman et al. 1992; Moore et al. 1998; Shomstein and Yantis 2002). See, for instance, Egly et al. (1994) and Kramer and Jacobson (1991) for a comparison of spatial and object-based attention.

With their "shifter circuit" model, Olshausen et al. (1993) successfully demonstrated deployment of spatial attention using gain modulation at various levels of the visual processing hierarchy. In combination with an associative memory, their model is capable of object detection invariant to translation and scale. This model, however, has only a rudimentary concept of saliency, relying solely on luminance contrast, and the extent of the attended "blobs" is fixed rather than derived from image properties as done in our model.

Most reports of modulation of area V1 or LGN are fMRI studies (e.g., Kastner et al. 1998; Gandhi et al. 1999; O'Connor et al. 2002) and do not allow a direct estimation of the level of modulation of neural activity. In a recent electrophysiology study, however, McAdams and Reid (2005) found neurons in macaque V1 whose spiking activity was modulated by up to 27 % when the cell's receptive field was attended to.

While our simulation results for modulating the S1 layer agree with this number, we are cautious to draw any strong conclusions. The response of S2 units is a linear sum of C1 activities, which in turn are max-pooled S1 activities. Therefore, the fact that the results in figures 3.4 and 3.5 are very similar to the results in figures 3.2 and 3.3 is not surprising.

To summarize, in our computer simulations of attentional modulation of V4-like layer S2, we found that modulation by 20–40 % suffices for successful sequential detection of artificial objects in multi-object displays. This range for modulation strength agrees well with the values found in several electrophysiological studies of area V4 in monkeys.

Chapter 4

Feature Sharing between Object Detection and Top-down Attention

4.1 Introduction

Visual search and other attentionally demanding processes are guided from the top down when a specific task is given (e.g., Wolfe et al. 2004). In the simplified stimuli commonly used in visual search experiments, e.g., red and horizontal bars, the selection of potential features that might be biased for is obvious (by design). In a natural setting with real-world objects, the selection of these features is not obvious, and there is some debate about which features can be used for top-down guidance and how a specific task maps to them (Wolfe and Horowitz 2004).

Learning to detect objects provides the visual system with an effective set of features suitable for the detection task and a mapping from these features to an abstract representation of the object. We suggest a model in which V4-type features are shared between object detection and top-down attention. As the model familiarizes itself with objects, i.e., it learns to detect them, it acquires a representation for features to solve the detection task. We propose that by cortical feedback connections, top-down processes can re-use these same features to bias attention to locations with a higher probability of containing the target object. We compare the performance of a computational implementation of such a model with pure bottom-up attention and, as a benchmark, with biasing for skin hue, which is known to work well as a top-down bias for faces.

The feed-forward recognition model used in this chapter was designed by Thomas Serre, based on the HMAX model for object recognition in cortex by Dr. Maximilian Riesenhuber and Dr. Tomaso Poggio. Face and non-face stimuli for the experiments were collected and annotated by Xinpeng Huang and Thomas Serre at MIT. I designed the top-down attention mechanism and the model of skin hue and conducted th experiments and analyses.

4.2 Model

The hierarchical model of object recognition used in chapter 3 has a fixed set of intermediate-level features at the S2 level. These features are well suited for the paper clip stimuli of chapter 3, but they are not sufficiently complex for recognition of real-world objects in cluttered images. In this chapter we adopt the extended version of the model by Serre et al. (2005a,b) and Serre and Poggio (2005) with more complex features that are learned from natural scene statistics. We demonstrate how top-down attention for a particular object category, faces in our case, is obtained from feedback connections in the same hierarchy used for object detection.

4.2.1 Feature Learning

In the extended model, S2 level features are no longer hardwired but are learned from a set of training images. The S1 and C1 activitations are computed in the same way as described in chapter 3. Patches of the C1 activation maps are sampled at several randomly chosen locations in each training image and stored as S2 feature prototypes (figure 4.2). If the patches are of size $4 \times m \times m$ (assuming four orientations in C1), then each prototype represents a vector in a $4m^2$-dimensional space. To evaluate a given S2 feature for a new image, the distance of each $m \times m$ patch of C1 activation for the image from the S2 prototype is computed using a Gaussian distance measure, resulting in an S2 feature map with the same spatial resolution as the C1 maps.

During feature learning, each prototype p is assigned a utility function $u(p)$, which is initialized to $u_0(p) = 1$. For each training image, several (e.g., 100) patches are sampled from the respective C1 activation maps, and the response of each prototype for each of the patches is determined. Each patch is then assigned to the prototype with the highest response, and the number of patches assigned to each prototype p is counted as $c(p)$. Subsequently, the utility function is updated according to

$$u_{t+1}(p) = \begin{cases} \alpha \cdot u_t(p) & \text{if } c(p) = 0 \\ \alpha \cdot u_t(p) + \beta & \text{if } c(p) > 0 \end{cases}, \tag{4.1}$$

with $0 < \alpha < 1$ and $\beta > 1$. Thus, utility decreases for prototype p whenever p does not get a patch assigned, but increases if it does. Whenever utility drops below a threshold θ, the prototype is discarded and re-initialized to a new randomly selected patch, and its utility is reset to 1. The prototypes surviving several iterations over all training images are fixed and used as intermediate-level features for object recognition and top-down attention.

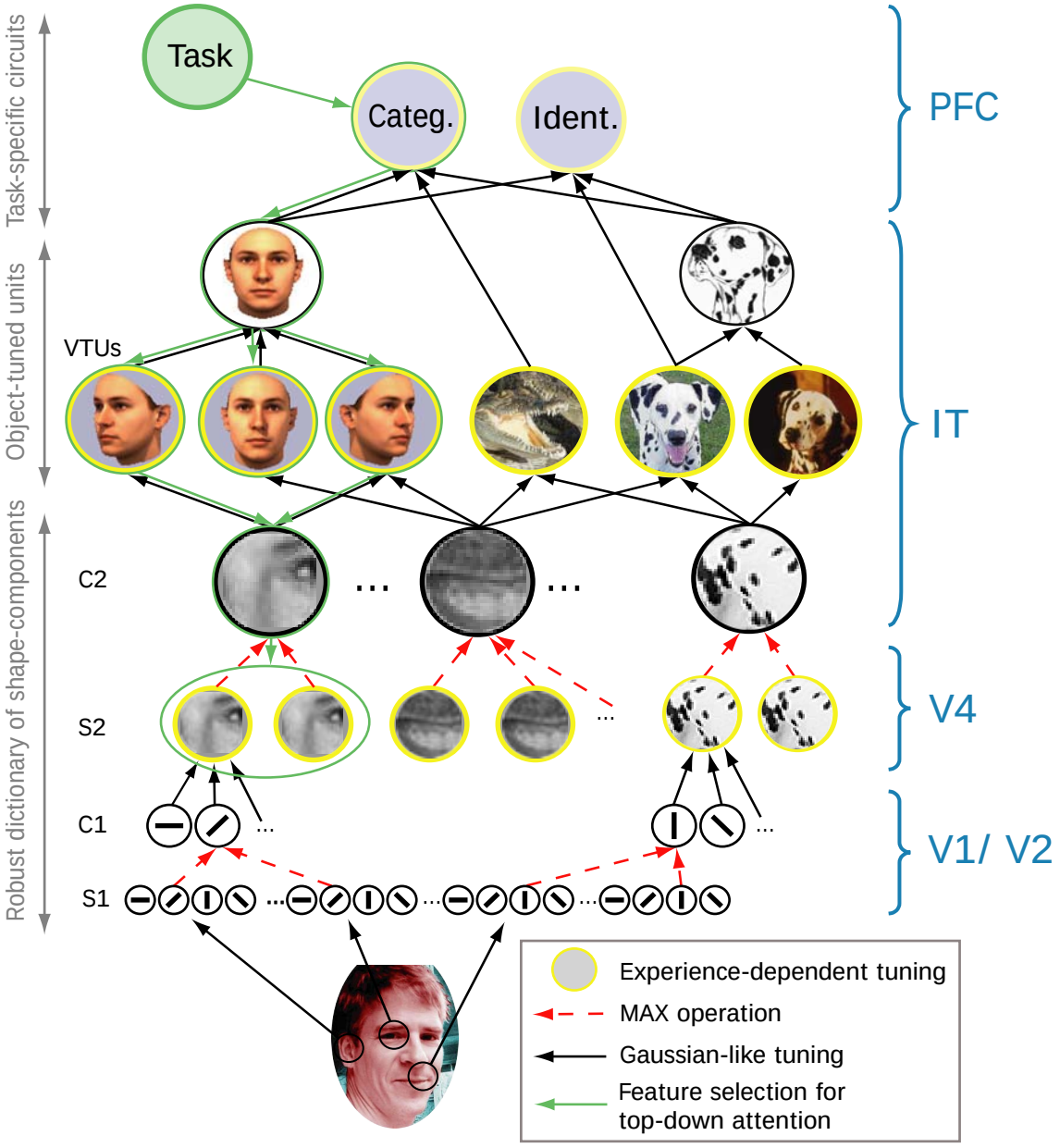

Figure 4.1: The basic architecture of our system of object recognition and top-down attention in the visual cortex (adapted from Walther et al. 2005b; Serre et al. 2005a). In the feed-forward pass, feature selective units with Gaussian tuning (black) alternate with pooling units using a maximum function (purple). Increasing feature selectivity and invariance to translation are built up as visual information progresses through the hierarchy until, at the C2 level, units respond to the entire visual field but are highly selective to particular features. View-tuned units (VTUs) and, finally, units selective to individual objects or object categories are trained. By association with a particular object or object category, activity due to a given task can traverse down the hierarchy (green) to identify a small subset of features at the S2 level that are indicative for the particular object category.

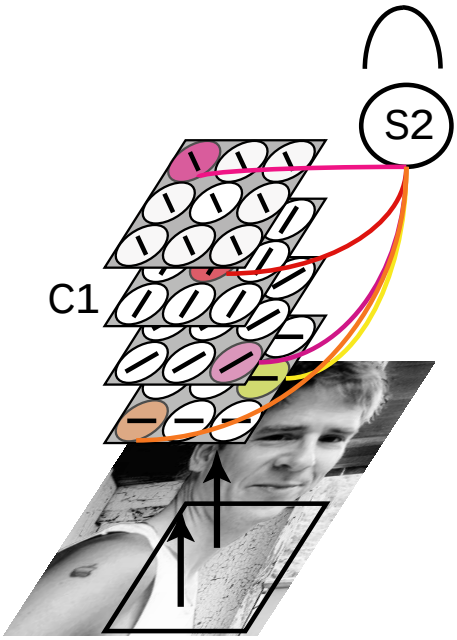

Figure 4.2: S2-level features are patches of the four orientation sensitive C1 maps cut out of a set of training images. S2 units have Gaussian tuning in the high-dimensional space that is spanned by the possible feature values of the four maps in the cut-out patch. During learning, S2 prototypes are initialized randomly from a training set of natural images that contain examples of the eventual target category among other objects and clutter. The stability of an S2 feature is determined by the number of randomly selected locations in the training images, for which this unit shows the highest response compared to the other S2 feature units. S2 prototypes with low stability are discarded and re-initialized.

4.2.2 Object Detection

To train the model for object recognition, it is presented with training images with and without examples of the object category of interest somewhere in the image. For each training image, the S1 and C1 activities are computed, and S2 feature maps are obtained using the learned S2 prototypes. In a final spatial pooling step, C2 activities are computed as the maximum over S2 maps, resulting in a vector of C2 activities that is invariant to object translation in the visual field of the model (figure 4.1). Given the C2 feature vectors for the positive and the negative training examples, a view-tuned unit (VTU) is trained using a binary classifier. For all experiments in this chapter we used a support vector machine (Vapnik 1998) with a linear kernel as a classifier. Given semantic knowledge on which views of objects belong to the same object or object category, several view-tuned units may by pooled to indicate object identity or category membership. Thus, a mapping from the set of S2 features to an abstract object representation is created.

For testing, new images are presented to the model and processed as described above to obtain their C2 feature vectors. The response of the classifier to the C2 feature vector determines whether the test images are classified as containing instances of the target object or object category or not. Note that, once the system is trained, the recognition process is purely feed-forward, which is compatible with rapid object categorization in humans (Thorpe et al. 1996) and monkeys (Fabre-Thorpe et al. 1998).

4.2.3 Top-down Attention

"Top-down attention" refers to the set of processes used to bias visual perception based on a given task or other prior expectation, as opposed to purely stimulus-driven "bottom-up attention" (chapter 2). One of the most puzzling aspects of top-down attention is how the brain "knows" which biases need to be set to fulfill a given task. Frequently, tasks are associated with objects or object categories, e.g., for search or the intention to manipulate an object in order to achieve a goal.

While feature learning establishes a mapping from the image pixels to a representation of intermediate complexity, training an object detection system creates a mapping from those features to the more abstract representations of objects or object categories. Reversing this mapping provides a method for finding suitable features for top-down attention to an object category that is relevant for a specific task (green arrows in figure 4.1).

Here we investigate how well these S2 maps are suited for localizing instances of the target category. Using these maps, potential object location can be attended one at a time, thus disambiguating multiple instances of an object category and allowing for suppression of visual information that is irrelevant for the task.

4.3 Experimental Setup

For the work presented in this chapter, we trained our model on detecting frontal views of human faces and investigated the suitability of the corresponding S2 features for top-down attention to faces.

For feature learning and training, we used 200 color images, each containing one face among clutter, and 200 distracter images without faces (see figure 4.3 for examples). For testing the recognition performance of the system, we used 201 face images and 2119 non-face distracter images. All images were obtained from the world wide web, and face images were labeled by hand, with the eyes, nose and mouth of each face marked.[1] Images were scaled such that faces were at approximately the same scale.

During feature learning as described in subsection 4.2.1, 100 patches of size 6×6 were extracted from the C1 maps for each presentation of a training image. Using the parameters $\alpha = 0.9$ and $\beta = 1.1$ for eq. 4.1, 100 stable features were learned over five iterations of presenting the 200 training images in random order. Two separate sets of features were learned: set A was derived from patches that were extracted from any location in the training images (figure 4.3, top row); patch selection for set B was limited to regions around faces (figure 4.3, second row).

Separate VTUs for frontal faces were created for feature sets A and B. A support vector machine classifier with linear kernel was trained on the face and non-face training images. The VTUs were

[1] Thanks to Xinpeng Huang and Thomas Serre for collecting and labeling the images.

Figure 4.3: Examples for training stimuli for feature set A (top row), feature set B (second row), test stimuli with two or more faces (third and fourth row), and for non-face distracters (bottom row).

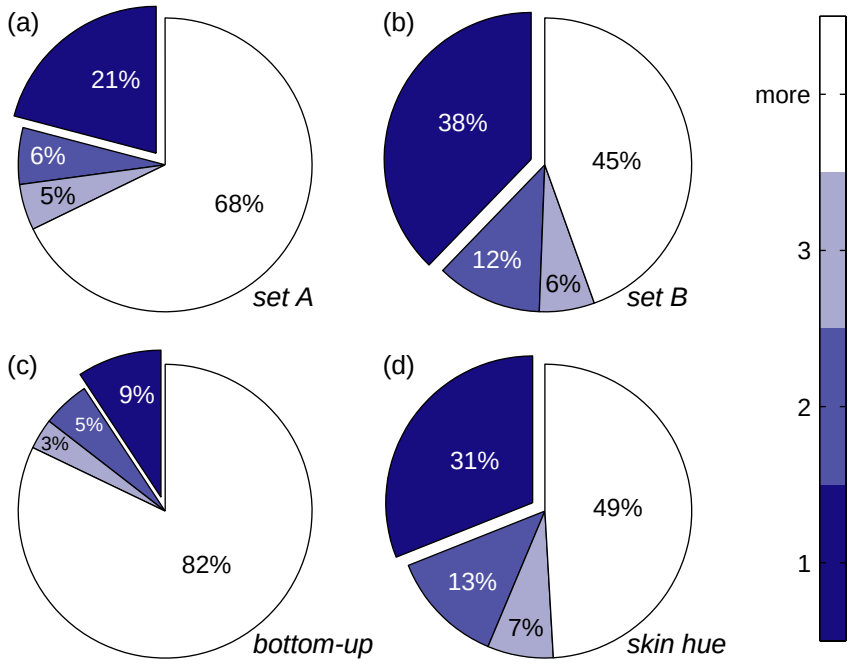

Figure 4.4: Fractions of faces in test images requiring one, two, three, or more than three fixations to be attended when using top-down feature sets A or B, bottom-up attention, or biasing for skin hue.

tested on the 201 face and 2119 non-face images.

To evaluate feature sets A and B for top-down attention, the S2 maps were computed for 179 images containing between 2 and 20 frontal views of faces (figure 4.3, third and fourth row). These top-down feature maps were compared to the bottom-up saliency map (see section 2.2) and to a skin hue detector for each of the images. Skin hue is known to be an excellent indicator for the presence of a face in color images (Darrel et al. 2000). Here we use it as a benchmark for comparison with our structure-based top-down attention maps. See section A.4 for details about our model of skin hue detection.

4.4 Results

After feature learning and training of the frontal face VTUs, we obtained ROC curves for the test images with feature sets A and B. The areas under the ROC curves are 0.989 for set A and 0.994 for set B.

We used two metrics for testing the suitability of the features for top-down attention to faces for the 179 multiple-face images, an analysis of fixations on faces, and a region of interest ROC analysis. Both methods start with the respective activation maps: the S2 feature maps for both feature sets, the bottom-up saliency map, and the skin hue bias map.

For the fixation analysis, each map was treated like a saliency map, and the locations in the

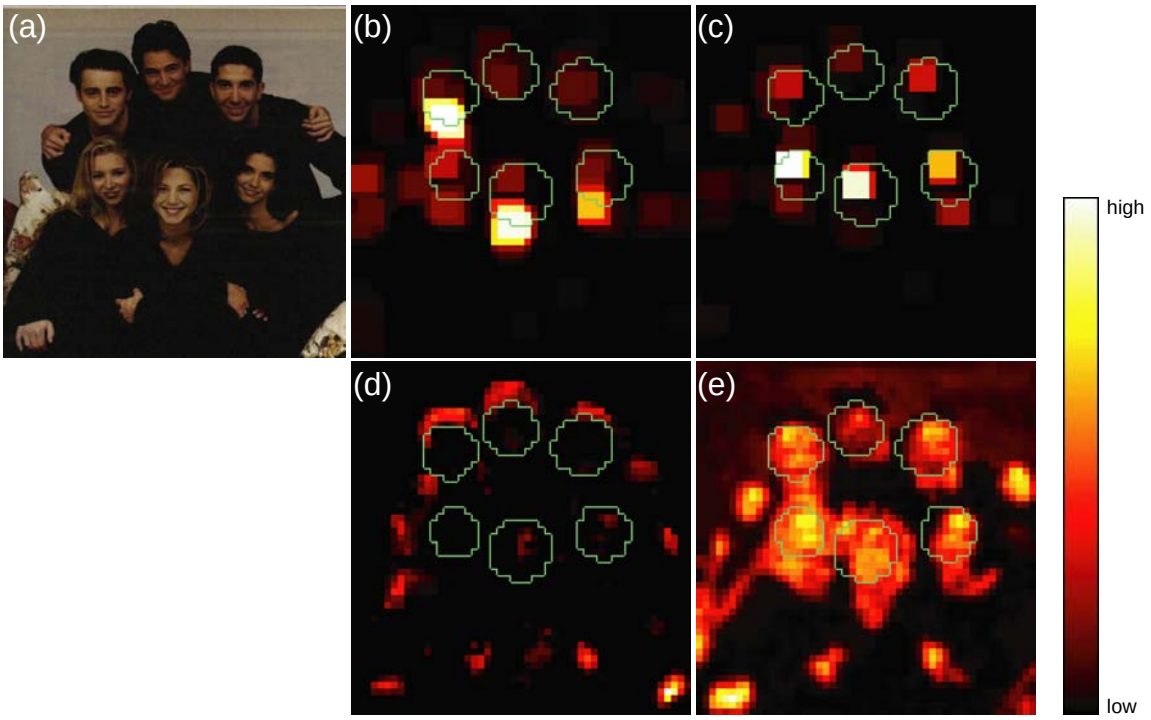

Figure 4.5: Using ground truth about the position of faces in the test images, activation maps can be segmented into face regions of interest (ROIs) and non-face regions. (a) input image; (b) one of the S2 maps from set A; (c) one of the set B S2 maps; (d) bottom-up saliency map; (e) skin hue distance map. Histograms of the map activations are used for an ROI ROC analysis (see fig. 4.6).

map were visited in order of decreasing saliency, neglecting spatial relations between the locations. While this procedure falls short of the full simulation of a winner-take-all network with inhibition of return as described in chapter 2, it nevertheless provides a simple and consistent means of scanning the maps.

For each map we determined the number of fixations required to attend to a face and, once the focus of attention leaves the most salient face, how many fixations it takes to attend to each subsequent face. The fraction of all faces that required one, two, three, or more than three fixations to be found was determined for each feature. The results are shown in figure 4.4 for the best features from sets A and B, for bottom-up attention, and for skin hue detection. Feature set B and skin hue detection show similar performance, followed by feature set A and bottom-up attention.

The second method of analyzing the suitability of the S2 feature maps to localize faces is illustrated in figure 4.5. From ground truth about the location of faces in the test images, we can divide the S2 feature maps into two regions, a region of interest (ROI) containing the S2 units that are inside the face regions, and its complement, containing all remaining S2 units. Ideally, we would like to see high activity inside the ROI and low or no activity outside the ROI.

Activity histograms for both regions as shown in figure 4.6 let us derive an ROC curve by moving

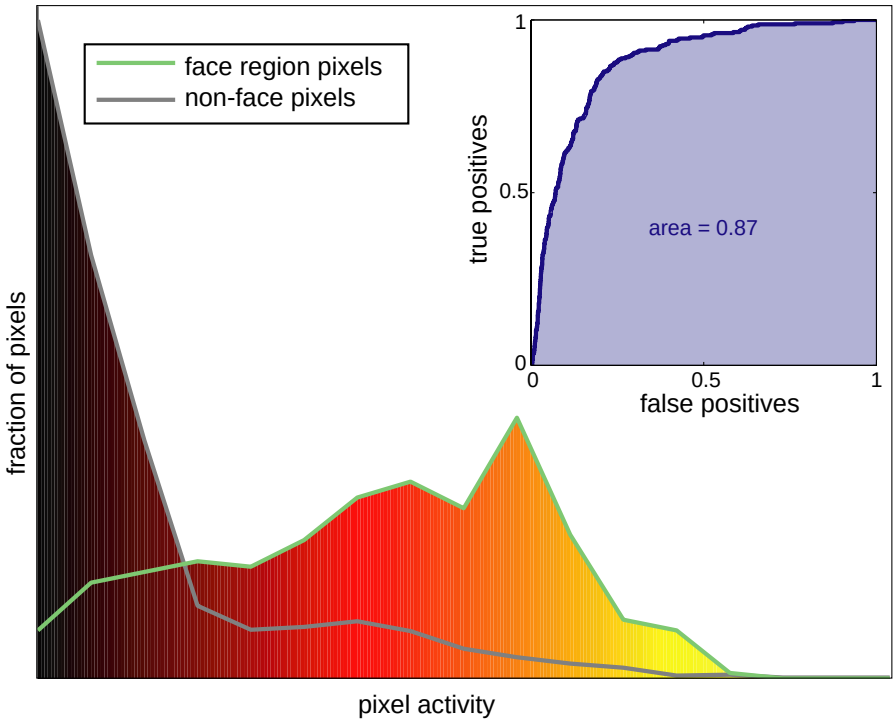

Figure 4.6: By sliding a threshold through the histograms of map activations for face and non-face regions for one of the maps shown in fig. 4.5, an ROC curves is established (inset). The mean of the areas under the curves for all test images is used to measure how well this feature is suited for biasing visual attention toward face regions.

a threshold through the histograms and interpreting the ROI units with activity above the threshold as true positives and the non-ROI units with activity above the threshold as false positives. The area under the ROC curve provides a measure for how well this particular activity map is suited for localizing faces in this test image. For each S2 feature, the ROI ROC area is computed for all 179 test images, and the mean over the test images is used as the second measure of top-down localization of faces.

The results from both evaluation methods are shown in figure 4.7. Only the fraction of cases in which the first fixation lands on a face (the dark blue areas in figure 4.4) is plotted. The two methods correlate with $\rho_{AB} = 0.72$.

Both evaluation methods indicate that the best features of feature set B perform similarly to skin hue detection for localizing frontal faces. Top-down attention based on S2 features by far outperform bottom-up attention in our experiments. While bottom-up attention is well suited to identify salient regions in the absence of a specific task, it cannot be expected to localize a specific object category as well as feature detectors that are specialized for this category.

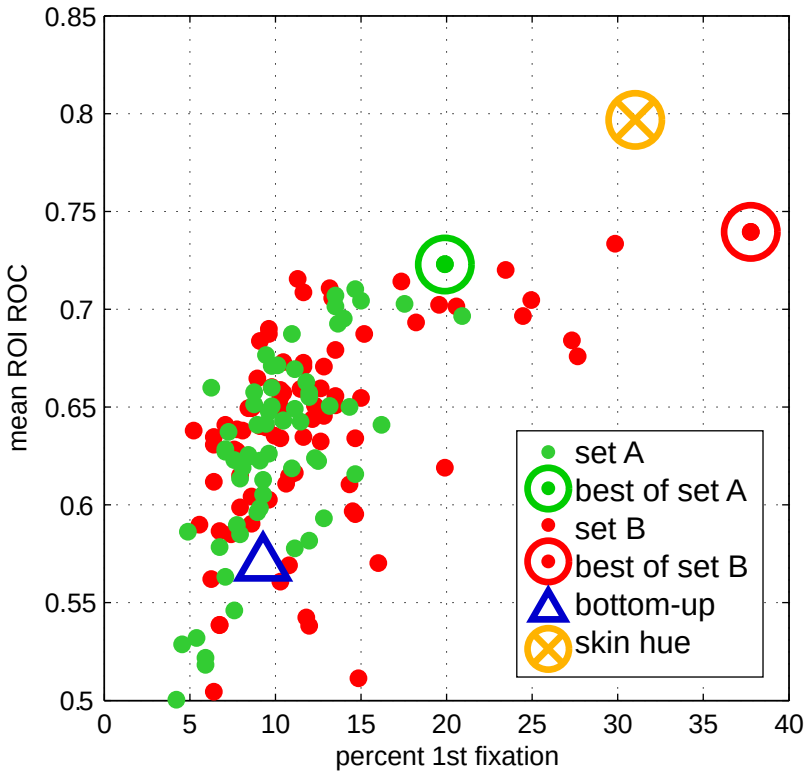

Figure 4.7: The fraction of faces in test images attended to on the first fixation (the dark blue areas in figure 4.4) and the mean areas under the ROC curves of the region of interest analysis (see figures 4.5 and 4.6) for the features from sets A (green) and B (red) and for bottom-up attention (blue triangle) and skin hue (yellow cross). The best features from sets A and B (marked by a circle) show performance in the same range as biasing for skin hue, although no color information is used to compute those feature responses.

4.5 Discussion

In this chapter we showed that features learned for recognizing a particular object category may also serve for top-down attention to that object category. Object detection can be understood as a mapping from a set of features to an abstract object representation. When a task implies the importance of an object, the respective abstract object representation may be invoked, and feedback connections may reverse the mapping, allowing inference of which features are useful to guide top-down attention to image locations that have a high probability of containing the target object.

Note that this mode of top-down attention does not necessarily imply that the search for any object category can be done in parallel using an explicit map representation. Search for faces, for instance, has been found to be efficient (Hershler and Hochstein 2005), although this result is disputed (VanRullen 2005). We have merely shown a method for identifying features that can be used to search for an object category. The efficiency of the search will depend on the complexity of those features and, in particular, on the frequency of the same features for other object categories,

which constitute the set of distracters for visual search. To analyze this aspect further, it would be of interest to explore the overlap in the sets of features that are useful for multiple object categories. Torralba et al. (2004) have addressed this problem for multiple object categories as well as multiple views of objects in a machine vision context.

The close relationship between object detection and top-down attention has been investigated before in a number of ways. In a probabilistic framework, Oliva et al. (2003) incorporate context information into the spatial probability function for seeing certain objects (e.g., people) at particular locations. Comparison with human eye tracking results show improvement over a purely bottom-up saliency-based attention (Itti et al. 1998). Milanese et al. (1994) describe a method for combining bottom-up and top-down information through relaxation in an associative memory. Rao (1998) considers attention a by-product of a recognition model based on Kalman filtering. He can get the system to attend to spatially overlapping (occluded) objects on a pixel basis for fairly simple stimuli.

Lee and Lee (2000) and Lee (2004) introduced a system for learning top-down attention using backpropagation in a multilayer perceptron network. Their system can segment superimposed handwritten digits on the pixel level.

In the work of Schill et al. (2001), features that maximize the gain of information in each saccade are learned using a belief propagation network. This is done using orientations only. Their system is tested on 24000 artificially created scenes which can be classified with a 80 % hit rate. Rybak et al. (1998) introduced a model that learns a combination of image features and saccades that lead to or from these features. In this way, translation, scale, and rotation invariance are built up. They successfully tested their system on small grayscale images. While this is an interesting system for learning and recognizing objects using saccades to build up object representations from multiple views, no explicit connection to top-down attention is made.

Grossberg and Raizada (2000) and Raizada and Grossberg (2001) propose a model of attention and visual grouping based biologically realistic models of neurons and neural networks. Their model relies on grouping detected edges within a laminar cortical structure by synchronous firing, allowing it to extract real as well as illusory contours.

The model by Amit and Mascaro (2003) for combining object recognition and visual attention has some resemblance with ours. Translation invariant detection is achieved by max-pooling, similar to Riesenhuber and Poggio (1999b). Basic units in their model consist of feature-location pairs, where location is measured with respect to the center of mass. Detection proceeds at many locations simultaneously, using hypercolumns with replica units that store copies of some image areas. The biological plausibility of these replica units is not entirely convincing, and it is not clear how to deal with the combinatorial explosion of the number of required units for a large number of object categories. Complex features are defined as combinations of orientations. There is a trade-off of accuracy versus combinatorics: More complex features lead to a better detection algorithm, but more

features are needed to represent all objects, i.e., the dimensionality of the feature space increases. Amit and Mascaro (2003) use binary features to make parameter estimation easier. Learning is performed by perceptrons that discriminate an object class from all other objects. These units vote to achieve classification. The system is demonstrated for the recognition of letters and for detecting faces in photographs.

Navalpakkam and Itti (2005) model the influence of task on attention by tuning the weights of feature maps based on the relevance of certain features for the search for objects that are associated with a given task in a knowledge database. Frintrop et al. (2005) also achieve top-down attention by tuning the weights of the feature maps in an attention system based on Itti et al. (1998). In their system, optimal weights are learned from a small set of training images, whose selection from a larger pool of images is itself subject to optimization.

Part II

Machine Vision

Chapter 5

Attention for Object Recognition

5.1 Introduction

Object recognition with computer algorithms has seen tremendous progress over the past years, both for specific domains such as face recognition (Schneiderman and Kanade 2000; Viola and Jones 2004; Rowley et al. 1998) and for more general object domains (Lowe 2004; Weber et al. 2000; Fergus et al. 2003; Schmid 1999; Rothganger et al. 2003). Most of these approaches require segmented and labeled objects for training, or at least that the training object is the dominant part of the training images. None of these algorithms can be trained on unlabeled images that contain large amounts of clutter or multiple objects.

But what is an object? A precise definition of "object," without taking into account the purpose and context, is of course impossible. However, it is clear that we wish to capture the appearance of those lumps of matter to which people tend to assign a name. Examples of distinguishing properties of objects are physical continuity (i.e., an object may be moved around in one piece), having a common cause or origin, having well defined physical limits with respect to the surrounding environment, or being made of a well defined substance. In principle, a single image taken in an unconstrained environment is not sufficient to allow a computer algorithm, or a human being, to decide where an object starts and another object ends. However, a number of cues which are based on the statistics of our everyday's visual world are useful to guide this decision. The fact that objects are mostly opaque and often homogeneous in appearance makes it likely that areas of high contrast (in disparity, texture, color, brightness) will be associated with their boundaries. Objects that are built by humans, such as traffic signs, are often designed to be easily seen and discriminated from their environment.

Imagine a situation in which you are shown a scene, e.g., a shelf with groceries, and later you are asked to identify which of these items you recognize in a different scene, e.g., in your grocery cart. While this is a common situation in everyday life and easily accomplished by humans, none of the conventional object recognition methods is capable of coping with this situation. How is it that

humans can deal with these issues with such apparent ease?

The human visual system is able to reduce the amount of incoming visual data to a small but relevant amount of information for higher-level cognitive processing. Two complementary mechanisms for the selection of individual objects have been proposed, bottom-up selective attention and grouping based on segmentation. While saliency-based attention concentrates on feature *contrasts* (Walther et al. 2005a, 2004b; Rutishauser et al. 2004a; Itti et al. 1998), grouping and segmentation attempt to find regions that are *homogeneous* in certain features (Shi and Malik 2000; Martin et al. 2004). Grouping has been applied successfully to object recognition, e.g., by Mori et al. (2004) and Barnard et al. (2003). In this chapter, we demonstrate that a bottom-up attentional mechanism as described in chapter 2 will frequently select image regions that correspond to objects.

Upon closer inspection, the "grocery cart problem" (also known as the "bin of parts problem" in the robotics community) poses two complementary challenges: (i) serializing the perception and learning of relevant information (objects) and (ii) suppressing irrelevant information (clutter). Visual attention addresses both problems by selectively enhancing perception at the attended location (see chapter 3) and by successively shifting the focus of attention to multiple locations.

The main motivation for attention in machine vision is cueing subsequent visual processing stages such as object recognition to improve performance and/or efficiency (Walther et al. (2005a); Rutishauser et al. (2004a)). So far, little work has been done to verify these benefits experimentally (but see Dickinson et al. (1997) and Miau and Itti (2001)). The focus of this chapter is on testing the usefulness of selective visual attention for object recognition experimentally. We do not intend to compare the performance of the various attention systems – this would be an interesting study in its own right. Instead, we use the saliency-based region selection mechanism from chapter 2 to demonstrate the benefits of selective visual attention for: (i) learning sets of object representations from single images and identifying these objects in cluttered test images containing target and distractor objects and (ii) object learning and recognition in highly cluttered scenes.

The work in this chapter is a collaboration with Ueli Rutishauser. While I implemented the attention system and the method for deploying spatial attention to the recognition system, Ueli implemented and conducted the experiments, and both of us analyzed the experiments. The code used for the object recognition system is a proprietary implementation of David Lowe's object recognition system (Lowe 2004) by Evolution Robotics.

5.2 Approach

To investigate the effect of attention on object recognition independent of the specific task, we do not consider a priori information about the images or the objects. Hence, we do not make use of top-down attention and rely solely on bottom-up, saliency-based attention.

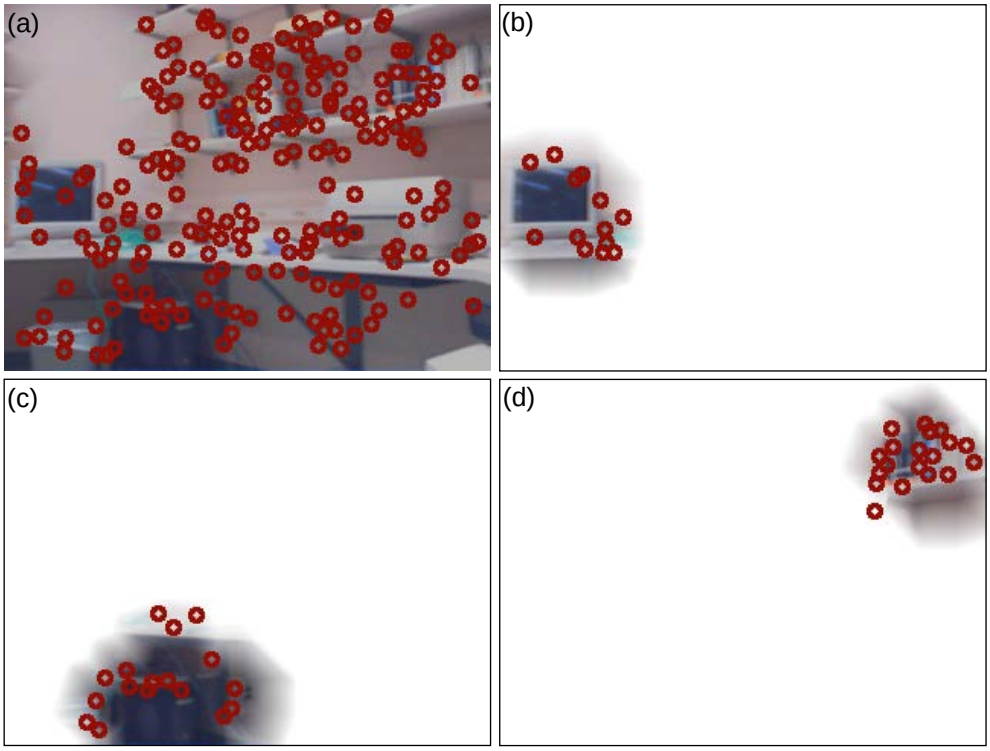

Figure 5.1: Example for SIFT keypoints used for object recognition by Lowe's algorithm. (a) keypoints of the entire image; (b-d) keypoints extracted for the three most salient regions, representing "monitor," "computer," and "set of books." Restricting the keypoints to a region that is likely to contain an object enables the recognition algorithm to subsequently learn and recognize multiple objects.

For object recognition, we selected David Lowe's algorithm (Lowe 2004, 1999, 2000) as an example for a general purpose recognition system with one-shot learning. The algorithm consists of two main stages – the selection of local, scale-invariant features ("SIFT" keypoints) and the matching of constellations of such keypoints.

Local keypoints are found in four steps (Lowe 2004). First, scale-space extrema are detected by searching over many scales and all image locations. This is implemented using difference-of-Gaussian functions, which are computed efficiently by subtracting blurred and sub-sampled versions of the image. In the second step, a detailed model is fitted to the candidate locations, and stable keypoints are selected (figure 5.1a). Next, orientations are assigned to the neighborhood of each keypoint based on local gray value gradients. With orientation, scale, and location of the keypoints known, invariance to these parameters is achieved by performing all further operations relative to these dimensions. In the last step, 128-dimensional "SIFT"(Scale Invariant Feature Transform) keypoint descriptors are derived from image gradients around the keypoints, providing robustness to shape distortions and illumination changes.

Object learning consists of extracting the SIFT features from a reference image and storing them

in a data base (one-shot learning). When presented with a new image, the algorithm extracts the SIFT features and compares them with the keypoints stored for each object in the data base. To increase robustness to occlusions and false matches from background clutter, clusters of at least three feature points need to be matched successfully. This test is performed using a hash table implementation of the generalized Hough transform (Ballard 1981). From matching keypoints, the object pose is approximated, and outliers and any additional image features consistent with the pose are determined. Finally, the probability that the measured set of features indicates the presence of an object is obtained from the accuracy of the fit of the keypoints and the probable number of false matches. Object matches are declared based on this probability (Lowe 2004).

In our model, we introduce the additional step of finding salient image patches as described in chapter 2 for learning and recognition before keypoints are extracted. Starting with the segmented map $\hat{\mathcal{F}}_w$ from eq. 2.11 on page 10, we derive a mask $\mathcal{M}$ at image resolution by thresholding $\hat{\mathcal{F}}_w$, scaling it up, and smoothing it. Smoothing can be achieved by convolving with a separable two-dimensional Gaussian kernel ($\sigma = 20$ pixels). We use a computationally more efficient method, consisting of opening the binary mask with a disk of 8 pixels radius as a structuring element, and using the inverse of the chamfer 3-4 distance for smoothing the edges of the region. $\mathcal{M}$ is normalized to be 1 within the attended object, 0 outside the object, and it has intermediate values at the object's edge. We use this mask to modulate the contrast of the original image $\mathcal{I}$ (dynamic range $[0, 255]$):

$$\mathcal{I}'(x, y) = [255 - \mathcal{M}(x, y) \cdot (255 - \mathcal{I}(x, y))] \tag{5.1}$$

where $[\cdot]$ symbolizes the rounding operation. Eq. 5.1 is applied separately to the r, g and b channels of the image. $\mathcal{I}'$ (figure 5.1b-d) is used as the input to the recognition algorithm instead of $\mathcal{I}$ (figure 5.1a).

The use of contrast modulation as a means of deploying object-based attention is motivated by neurophysiological experiments that show attentional enhancement to act in a manner equivalent to increasing stimulus contrast (Reynolds et al. 2000; McAdams and Maunsell 2000); as well as by its usefulness with respect to Lowe's recognition algorithm. Keypoint extraction relies on finding luminance contrast peaks across scales. As we remove all contrast from image regions outside the attended object (eq. 5.1), no keypoints are extracted there. As a result, deploying selective visual attention spatially groups the keypoints into likely candidates for objects.

In the learning phase, this selection limits model formation to attended image regions, thereby avoiding clutter and, more importantly, enabling the acquisition of several object models at multiple locations in a single image. During the recognition phase, only keypoints in the attended region need to be matched to the stored models, again avoiding clutter, and making it easier to recognize multiple objects. See figure 5.8 for an illustration of the reduction in complexity due to this procedure.

To avoid strong luminance contrasts at the edges of attended regions, we smoothed the representation of the region as described above. In our experiments, we found that the graded edges of the salient regions introduce spurious features, due to the artificially introduced gradients. Therefore, we threshold the smoothed mask before contrast modulation.

The number of fixations used for recognition and learning depends on the resolution of the images, and on the amount of visual information. In low-resolution images with few objects, three fixations may be sufficient to cover the relevant parts of the image. In high-resolution images with a large amount of information, up to 30 fixations are required to sequentially attend to most or all object regions. Humans and monkeys, too, need more fixations to analyze scenes with richer information content (Sheinberg and Logothetis 2001; Einhäuser et al. 2006). The number of fixations required for a set of images is determined by monitoring after how many fixations the serial scanning of the saliency map starts to cycle for a few typical examples from the set. Cycling usually occurs when the salient regions have covered approximately 40–50 % of the image area. We use the same number of fixations for all images in an image set to ensure consistency throughout the respective experiment.

It is common in object recognition to use interest operators (Harris and Stephens 1988) or salient feature detectors (Kadir and Brady 2001) to select features for learning an object model. This is different, however, from selecting an image region and limiting the learning and recognition of objects to this region.

In the next section we verify that the selection of salient image regions does indeed produce meaningful results when compared with random region selection. In the two sections after that, we report experiments that address the benefits of attention for serializing visual information processing and for suppressing clutter.

5.3 Selective Attention versus Random Patches

In the first experiment we compare our saliency-based region selection method with randomly selected image patches using a series of images with many occurrences of the same objects. Since human photographers tend to have a bias toward centering and zooming on objects, we make use of a robot for collecting a large number of test images in an unbiased fashion.

Our hypothesis is that regions selected by bottom-up, saliency-based attention are more likely to contain objects than randomly selected regions. If this hypothesis were true, then attempting to match image patches across frames would produce more hits for saliency-based region selection than for random region selection because in our image sequence objects re-occur frequently.

This does not imply, however, that every image patch that is learned and recognized corresponds to an object. Frequently, groups of objects (e.g., a stack of books) or parts of objects (e.g., a corner of a desk) are selected. For the purpose of the discussion in this section we denote patches that contain

Figure 5.2: Six representative frames from the video sequence recorded by the robot.

parts of objects, individual objects, or groups of objects as "object patches." In this section we demonstrate that attention-based region selection finds more object patches that are more reliably recognized throughout the image set than random region selection.

5.3.1 Experimental Setup

We used an autonomous robot equipped with a camera for image acquisition. The robot's navigation followed a simple obstacle avoidance algorithm using infrared range sensors for control. The camera was mounted on top of the robot at about 1.2 m height. Color images were recorded at 320×240 pixels resolution at 5 frames per second. A total of 1749 images was recorded during an almost 6 min run. See figure 5.2 for example frames. Since vision was not used for navigation, the images taken by the robot are unbiased. The robot moved in a closed environment (indoor offices/labs, four rooms, approximately 80 m^2). The same objects reappear repeatedly in the sequence.

The process flow for selecting, learning, and recognizing salient regions is shown in figure 5.3. Because of the low resolution of the images, we use only $N = 3$ fixations in each image for recognizing and learning patches. Note that there is no strict separation of a training and a test phase here. Whenever the algorithm fails to recognize an attended image patch, it learns a new model from it. Each newly learned patch is assigned a unique label, and we count the number of matches for the patch over the entire image set. A patch is considered "useful" if it is recognized at least once after learning, thus appearing at least twice in the sequence.

We repeated the experiment without attention, using the recognition algorithm on the entire image. In this case, the system is only capable of detecting large scenes but not individual objects

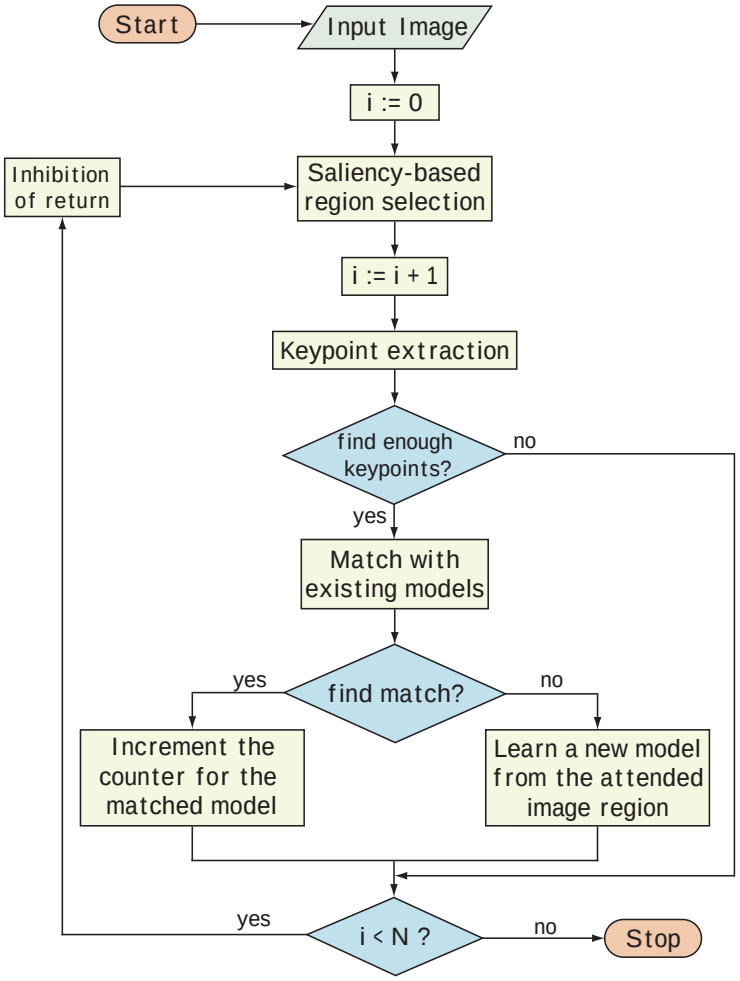

Figure 5.3: The process flow in our multi-object recognition experiments. The image is processed with the saliency-based attention mechanism as described in figure 2.2. In the resulting contrast-modulated version of the image (eq. 5.1), keypoints are extracted (figure 5.1) and used for matching the region with one of the learned object models. A minimum of three keypoints is required for this process (Lowe 1999). In the case of successful recognition, the counter for the matched model is incremented; otherwise a new model is learned. By triggering object-based inhibition of return, this process is repeated for the N most salient regions. The choice of N depends mainly on the image resolution. For the low resolution (320×240 pixels) images used in section 5.3, $N = 3$ is sufficient to cover a considerable fraction (approximately 40 %) of the image area.

Table 5.1: Results using attentional selection and random patches.

	Attention	**Random**
number of patches recognized	3934	1649
average per image	2.25	0.95
number of unique object patches	824	742
number of good object patches	87 (10.6 %)	14 (1.9 %)
number of patches associated with good object patches	1910 (49 %)	201 (12 %)
false positives	32 (0.8 %)	81 (6.8 %)

or object groups. For a more meaningful control, we repeated the experiment with randomly chosen image regions. These regions are created by a pseudo region growing operation at the saliency map resolution. Starting from a randomly selected location, the original threshold condition for region growth is replaced by a decision based on a uniformly drawn random number. The patches are then treated the same way as true attention patches (see eqs. 2.10 and 2.11 in section 2.3). The parameters are adjusted such that the random patches have approximately the same size distribution as the attention patches.

Ground truth for all experiments is established manually. This is done by displaying every match established by the algorithm to a human subject, who has to rate it as either correct or incorrect based on whether the two patches have any significant overlap. The false positive rate is derived from the number of patches that were incorrectly associated with one another.

Our current implementation is capable of processing about 1.5 frames per second at 320×240 pixels resolution on a 2.0 GHz Pentium 4 mobile CPU. This includes attentional selection, shape estimation, and recognition or learning. Note that we use the robot only as an image acquisition tool in this experiment. For details on vision-based robot navigation and control see, for instance, Clark and Ferrier (1989) or Hayet et al. (2003).

5.3.2 Results

Using the recognition algorithm without attentional selection results in 1707 of the 1749 images being pigeon-holed into 38 unique object models representing non-overlapping large views of the rooms visited by the robot. The remaining 42 images are learned as new models, but then never recognized again. The models learned from these large scenes are not suitable for detecting individual objects. We have 85 false positives, i.e., the recognition system indicates a match between a learned model and an image, where the human subject does not indicate an agreement. This confirms that in this experiment, recognition without attention does not yield any meaningful results.

Attentional selection identifies 3934 useful patches in the approximately 6 minutes of processed video associated with 824 object models. Random region selection only yields 1649 useful patches associated with 742 models (table 5.1). With saliency-based region selection, we find 32 (0.8 %)

false positives, with random region selection 81 (6.8 %).

To better compare the two methods of region selection, we assume that "good" object patches should be recognized multiple times throughout the video sequence since the robot visits the same locations repeatedly. We sort the patches by their number of occurrences and set an arbitrary threshold of 10 recognized occurrences for "good" object patches for this analysis (figure 5.4). With this threshold in place, attentional selection finds 87 good object patches with a total of 1910 instances associated to them. With random regions, only 14 good object patches are found with a total of 201 instances. The number of patches associated with good object patches is computed from figure 5.4 as

$$N_g = \sum_{\forall i: n_i \geq 10} n_i \qquad (n_i \in \mathcal{O}), \tag{5.2}$$

where $\mathcal{O}$ is an ordered set of all learned objects, sorted descending by the number of detections.

From these results it is clear that our attention-based algorithm systematically selects regions that can be recognized repeatedly from various viewpoints with much higher reliability than randomly selected regions. Since we are selecting for regions with high contrast, the regions are likely to contain objects or object parts. This hypothesis is further supported by the results shown in the next two sections. With this empirical verification of the usefulness of the region selection algorithm detailed in section 5.2 we now go on to exploring its effect on processing multiple objects and on object learning and recognition in highly cluttered scenes.

5.4 Learning Multiple Objects from Natural Images

In this experiment we test the hypothesis that attention can enable learning and recognition of multiple objects in individual natural scenes. We use high-resolution digital photographs of sets of objects in indoor environments for this purpose.

5.4.1 Experimental Setup

We placed a number of objects into different settings in office and lab environments and took pictures of the objects with a digital camera. We obtained a set of 102 images at a resolution of 1280×960 pixels. Images can contain large or small subsets of the objects. We selected one of the images for training (figure 5.5a). The other 101 images were used as test images.

For learning and recognition we used 30 fixations, which cover about 50 % of the image area. Learning is performed completely unsupervised. A new model is learned at each fixation. During testing, each fixation on the test image is compared to each of the learned models. Ground truth is established manually by inspecting the learned patches and the patches extracted from the test images and flagging pairs that contain matching objects.

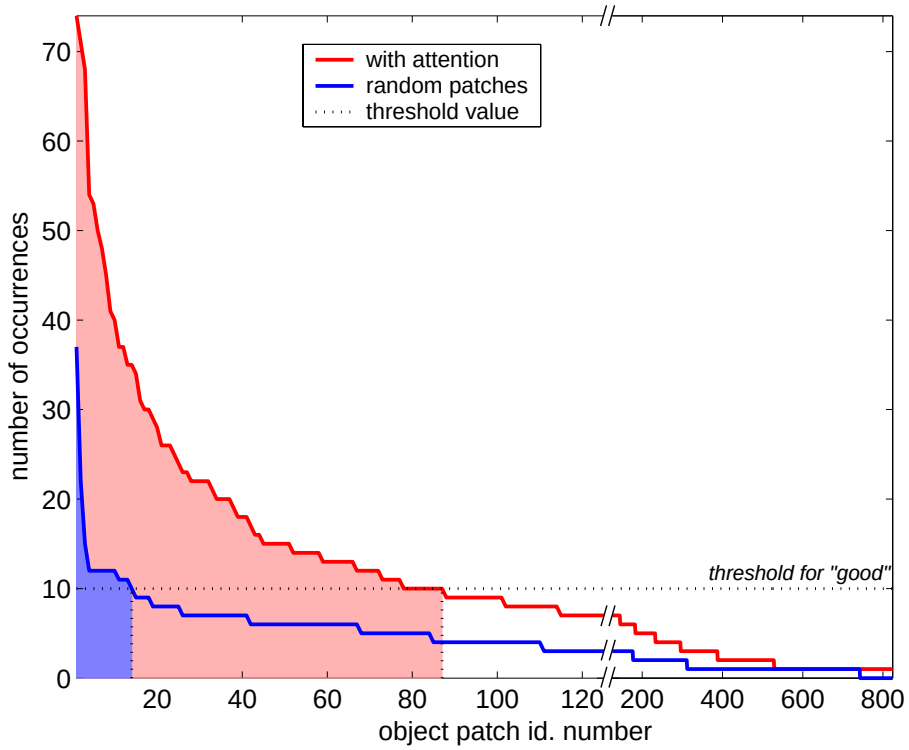

Figure 5.4: Learning and recognition of object patches in a stream of video images from a camera mounted on a robot. Object patches are labeled (x axis), and every recognized instance is counted (y axis). The threshold for "good" object patches is set to 10 instances. Region selection with attention finds 87 good object patches with a total of 1910 instances. With random region selection, 14 good object patches with 201 instances are found. Note the different linear scales on either side of the axis break in the x axis.

5.4.2 Results

From the training image, the system learns models for two objects that can be recognized in the test images – a book and a box (figure 5.5). Of the 101 test images, 23 contain the box and 24 the book, and of these four images contain both objects. Table 5.2 shows the recognition results for the two objects.

Even though the recognition rates for the two objects are rather low, one should consider that one unlabeled image is the only training input given to the system (one-shot learning). From this one image, the combined model is capable of identifying the book in 58 % and the box in 91 % of all cases, with only two false positives for the book and none for the box. It is difficult to compare this performance with some baseline, since this task is impossible for the recognition system alone without any attentional mechanism.

Figure 5.6 shows an example of matching two objects between two individual images in an outdoor environment. The objects are successfully matched using salient regions, despite the extensive occlusions for training of object 1 (figure 5.6 (c)) and for testing of object 2 (figure 5.6 (f)).

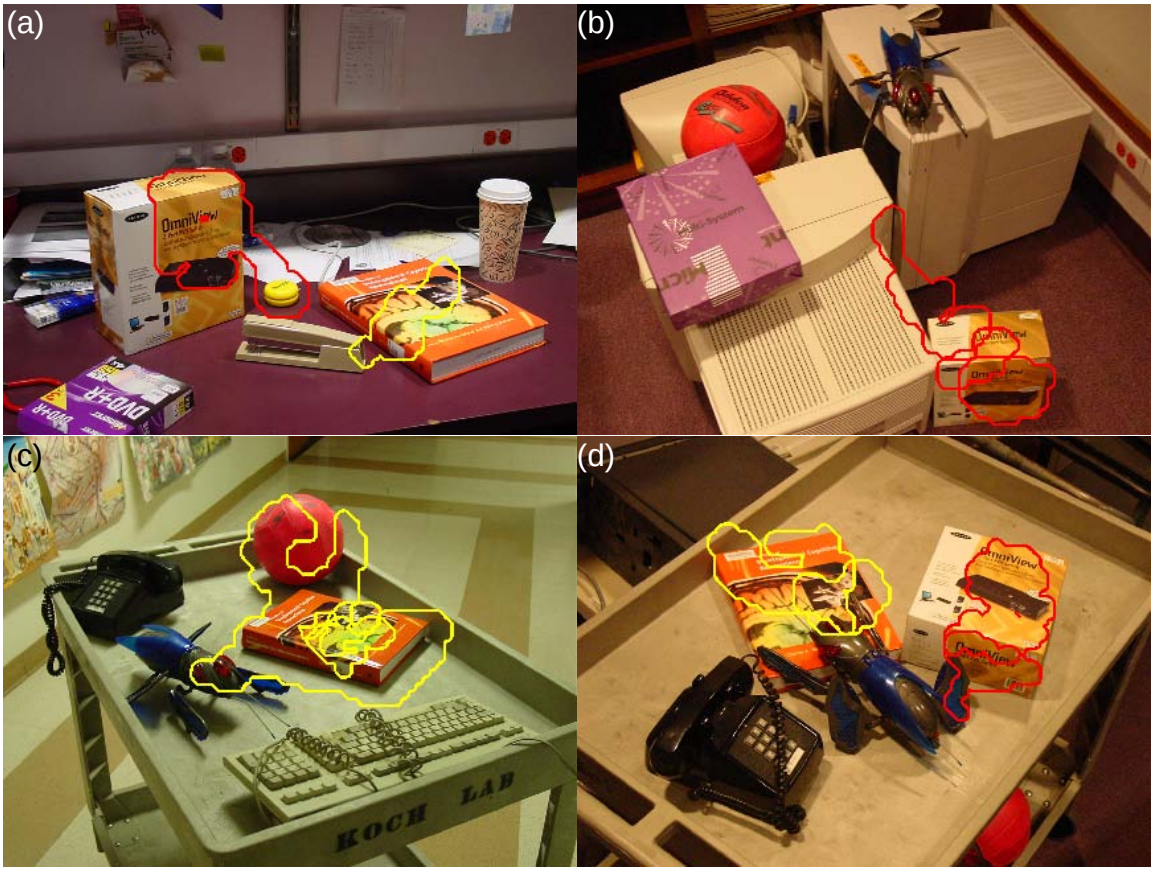

Figure 5.5: Learning and recognition of two objects in cluttered scenes. (a) the image used for learning the two objects; (b-d) examples for images in which objects are recognized as matches with one or both of the objects learned from (a). The patches, which were obtained from segmenting regions at multiple salient locations, are color coded – yellow for the book, and red for the box. The decision of whether a match occurred is made by the recognition algorithm without any human supervision.

In figure 5.7 we show another example for learning multiple objects from one photograph and recognizing the objects in a different visual context. In figure 5.7 (a), models for the soup cans are learned from several overlapping regions, and they all match with each other. One model is learned for the pasta box and the label on the beer pack, respectively. All three objects are found successfully in both test images. There is one false positive in figure 5.7 (c) – a bright spot on the table is mistaken for a can. This experiment is very similar to the "grocery cart problem" mentioned in the introduction. The images were processed at a resolution of 1024×1536 pixels; 15 fixations were used for training and 20 fixations for testing.

Figure 5.8 illustrates how attention-based region selection helps to reduce the complexity of matching constellations of keypoints between the images. Instead of attempting to match keypoint constellations based on the entire set of keypoints identified in the image, only the color coded subsets need to be compared to each other. The subsets with matching colors were identified as

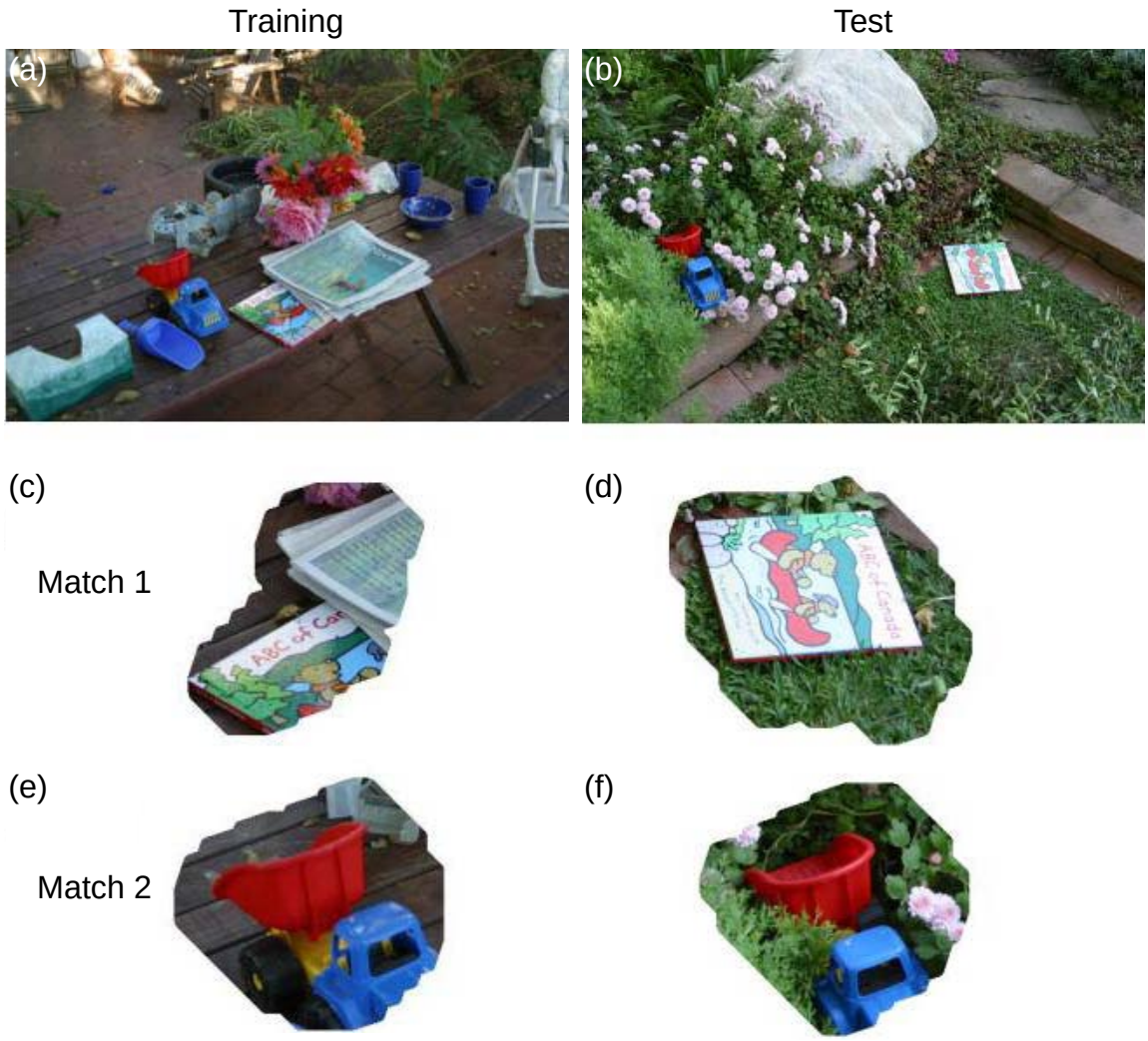

Figure 5.6: Example for learning two objects (c) and (e) from the training image (a) and establishing matches (d) and (f) for the objects in the test image (b), in a different visual context, with different object orientations and occlusions.

Table 5.2: Results for recognizing two objects that were learned from one image.

object	**hits**	**misses**	**false positives**
box	21 (91%)	2 (9%)	0 (0%)
book	14 (58%)	10 (42%)	2 (2.6%)

object matches by the recognition algorithm. This figure also illustrates that keypoints are found at all textured image locations – at the edges as well as on the faces of objects.

5.5 Objects in Cluttered Scenes

In the previous section we showed that selective attention enables the learning of two or more objects from single images. In this section, we investigate how attention can help to recognize objects in highly cluttered scenes.

5.5.1 Experimental Setup

To systematically evaluate recognition performance with and without attention we use images generated by randomly merging an object with a background image (figure 5.9). This design enables us to generate a large number of test images in a way that gives us good control of the amount of clutter versus the size of the objects in the images, while keeping all other parameters constant. The experimental design is inspired by Sheinberg and Logothetis (2001). Since we construct the test images, we also have easy access to ground truth. We use natural images for the backgrounds so that the abundance of local features in our test images matches that of natural scenes as closely as possible.

We quantify the amount of clutter in the images by the *relative object size* (ROS), defined as the ratio of the number of pixels of the object over the number of pixels in the entire image:

$$ROS = \frac{\#pixels(object)}{\#pixels(image)}. \tag{5.3}$$

To avoid issues with the recognition system due to large variations in the *absolute* size of the objects, we leave the number of pixels for the objects constant (with the exception of intentionally added scale noise) and vary the ROS by changing the size of the background images in which the objects are embedded. Since our background images contain fairly uniform amounts of clutter within as well as between images, the ROS can be used as an inverse measure of the amount of clutter faced by the object recognition algorithm when it attempts to learn or recognize the objects contained in the images. A *large* ROS means that the object is relatively large in the image and, hence, that it is faced with relatively *little* clutter. A small ROS, on the other hand, means a large amount of

Figure 5.7: Another example for learning several objects from a high-resolution digital photograph. The task is to memorize the items in the cupboard (a) and to identify which of the items are present in the test scenes (b) and (c). Again, the patches are color coded – blue for the soup can, yellow for the pasta box, and red for the label on the beer pack. In (a), only those patches are shown that have a match in (b) or (c), in (b) and (c) only those that have a match in (a).

clutter.

To introduce variability in the appearance of the objects, each object is rescaled by a random factor between 0.9 and 1.1, and uniformly distributed random noise between -12 and 12 is added to the red, green, and blue value of each object pixel (dynamic range is $[0, 255]$). Objects and backgrounds are merged by blending with an alpha value of 0.1 at the object border, 0.4 one pixel away, 0.8 three pixels away from the border, and 1.0 inside the objects, more than three pixels away from the border. This prevents artificially salient edges at the object borders and any high frequency components associated with them.

We created six test sets with ROS values of 5 %, 2.78 %, 1.08 %, 0.6 %, 0.2 %, and 0.05 %, each consisting of 21 images for training (one image of every object) and 420 images for testing (20 test images for every object). The background images for training and test sets are randomly drawn from disjoint image pools to avoid false positives due to repeating features in the background. An ROS of 0.05 % may seem unrealistically low, but humans are capable of recognizing objects with a much smaller relative object size, for instance for reading street signs while driving (Legge et al.

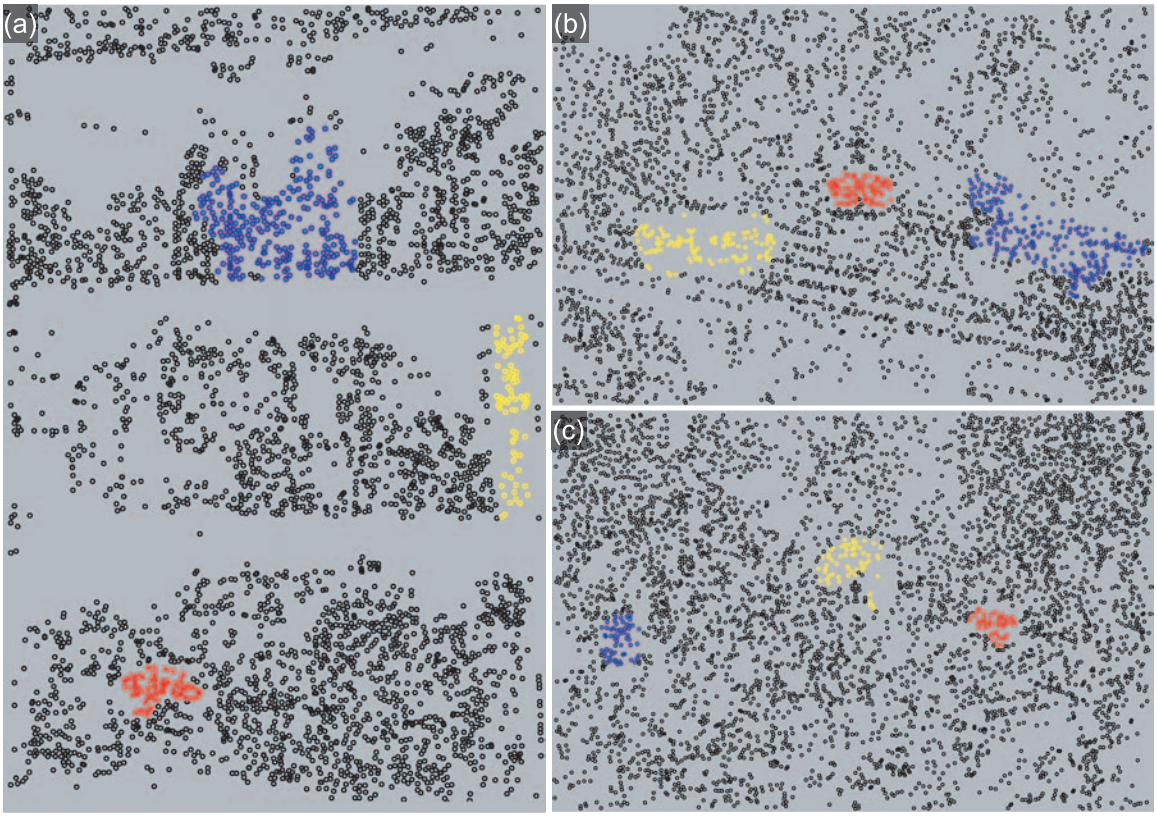

Figure 5.8: The SIFT keypoints for the images shown in figure 5.7. The subsets of keypoints identified by salient region selection for each of the three objects are color coded with the same colors as in the previous figure. All other keypoints are shown in black. In figure 5.7 we show all regions that were found for each of the objects – here we show the keypoints from one example region for each object. This figure illustrates the enormous reduction in complexity faced by the recognition algorithm when attempting to match constellations of keypoints between the images.

1985).

During training, object models are learned at the five most salient locations of each training image. That is, the object has to be learned by finding it in a training image. Learning is unsupervised, and thus most of the learned object models do not contain an actual object. During testing, the five most salient regions of the test images are compared to each of the learned models. As soon as a match is found, positive recognition is declared. Failure to attend to the object during the first five fixations leads to a failed learning or recognition attempt.

5.5.2 Results

Learning from our data sets results in a classifier that can recognize $K = 21$ objects. The performance of each classifier i is evaluated by determining the number of true positives (T_i) and the number of false positives (F_i). The overall true positive rate t (also known as detection rate) and the false

Figure 5.9: (a) Ten of the 21 objects used in the experiment. Each object is scaled such that it consists of approximately 2500 pixels. Artificial pixel and scaling noise is added to every instance of an object before merging it with a background image; (b,c) examples of synthetically generated test images. Objects are merged with the background at a random position by alpha-blending. The ratio of object area vs. image area (relative object size) varies between (b) 5 % and (c) 0.05 %.

positive rate f for the entire multi-class classifier are then computed as (Fawcett 2003)

$$t = \frac{1}{K}\sum_{i=1}^{K}\frac{T_i}{N_i} \text{ and} \tag{5.4}$$

$$f = \frac{1}{K}\sum_{i=1}^{K}\frac{F_i}{\overline{N}_i}. \tag{5.5}$$

Here, N_i is the number of positive examples of class i in the test set, and $\overline{N}_i$ is the number of negative examples of class i. Since in our experiments the negative examples of one class consist of the positive examples of all other classes, and since there are equal numbers of positive examples for all classes, we can write

$$\overline{N}_i = \sum_{j=1,j\neq i}^{K} N_j = (K-1)N_i. \tag{5.6}$$

To evaluate the performance of the classifier it is sufficient to consider only the true positive rate, since the false positive rate is consistently below 0.07 % for all conditions, even without attention and at the lowest ROS of 0.05 %.

We evaluate performance (true positive rate) for each data set with three different methods: (i) learning and recognition without attention; (ii) learning and recognition with attention; (iii) human

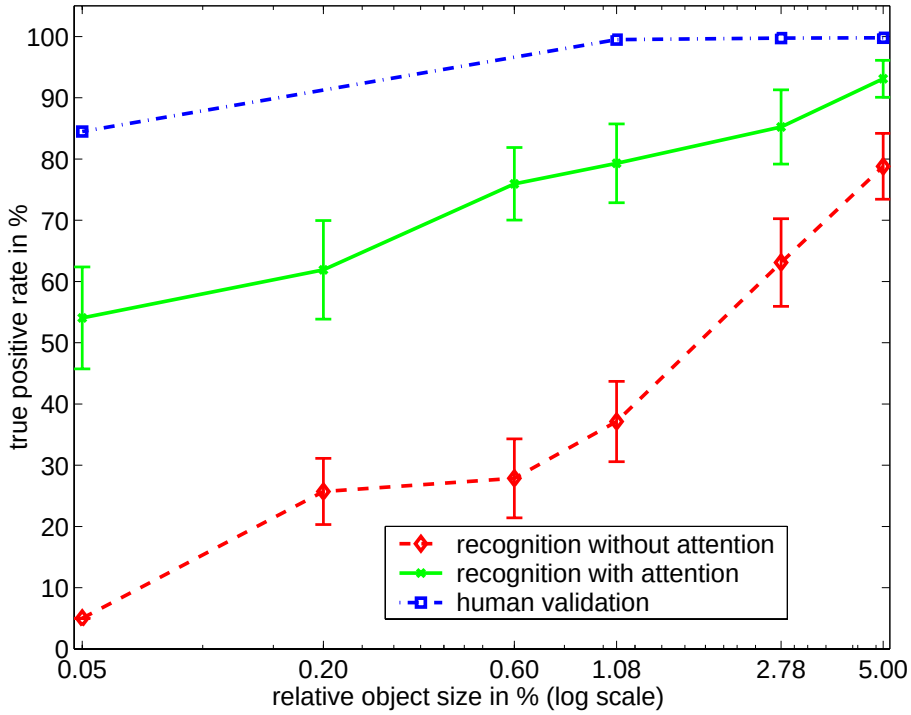

Figure 5.10: True positive rate (t) for a set of artificial images without attention (red) and with attention (green) over the relative object size (ROS). The ROS is varied by keeping the absolute object size constant at 2500 pixels ±10 % and varying the size of the background images. Error bars indicate the standard error for averaging over the performance of the 21 classifiers. The human subject validation curve (blue) separates the difference between the performance with attention (green) and 100 % into problems of the recognition system (difference between the blue and the green curves) and problems of the attention system (difference between the blue curve and 100 %). The false positive rate is less than 0.07 % for all conditions.

validation of attention. The third procedure attempts to explain what part of the performance difference between (ii) and 100 % is due to shortcomings of the attention system and what part is due to problems with the recognition system.

For human validation, all images in which the objects cannot be recognized automatically are evaluated by a human subject. The subject can only see the five attended regions of all training images and of the test images in question; all other parts of the images are blanked out. Solely based on this information, the subject is asked to indicate matches. In this experiment, matches are established whenever the attention system extracts the object correctly during learning and recognition. When the human subject is able to identify the objects based on the attended patches, the failure of the combined system is due to shortcomings of the recognition system, whereas the attention system is the component responsible for the failure when the human subject fails to recognize the objects based on the patches. As can be seen in figure 5.10, the human subject can recognize the objects from the attended patches in most failure cases, which implies that the recognition system is the main cause for the failure rate. Significant contributions to the failure rate

by the attention system are only observed for the highest amount of clutter ($ROS = 0.05$ %).

The results in figure 5.10 demonstrate that attention has a sustained effect on recognition performance for all reported relative object sizes. With more clutter (smaller ROS), the influence of attention becomes more accentuated. In the most difficult case (0.05 % relative object size), attention increases the true positive rate by a factor of 10. Note that for $ROS > 5$ %, learning and recognition using the entire image (red dashed line in figure 5.10) works well without attention, as reported by Lowe (2004, 1999).

We used five fixations throughout the experiment to ensure consistency. In preliminary experiments we investigated larger numbers of fixations as well. The performance increases slightly for more fixations, but the effect of adding more clutter remains the same.

5.6 Discussion

We set out to test two hypotheses for the effects of attention on object recognition. The first is that attention can serialize learning and recognition of multiple objects in individual images. With the experiments in section 5.4 we show that this new mode of operation, which is impossible for the recognition system without prior region selection, is indeed made possible by using our saliency-bases region selection algorithm.

Secondly, we show that spatial attention improves the performance of object learning and recognition in the presence of large amounts of clutter by up to an order of magnitude. The addition of attention-based region selection makes object recognition more robust to distracting clutter in the image.

We have limited our experiments to bottom-up attention to avoid task specificity. However, in many applications, top-down knowledge can be very useful for visual processing (Oliva et al. 2003) in addition to the saliency-based attention described here. In particular, for cases where behaviorally relevant objects may not be salient, a top-down mechanism for guiding attention to task-relevant parts of the scene becomes necessary (Navalpakkam and Itti 2005). See chapter 3 for our approach to top-down attention.

We have selected Lowe's recognition algorithm for our experiments because of its suitability for general object recognition. However, our experiments and their results do not depend on that specific choice for a recognition system. In chapter 3 we have shown the suitability of the method for a biologically realistic object recognition system in a different context (see also Walther et al. 2002a).

Neurophysiological experiments in monkeys show that the activity of neurons that participate in object recognition is only modulated by a relatively small amount due to attentional processes. In contrast, for a machine vision system it is beneficial to completely disregard all information outside

the focus of attention. For the work presented in this chapter, we have adopted this strategy by completely removing the luminance contrast outside the attended region, thereby restricting the search for keypoints to a region that is likely to contain an object.

An important attention related question that is not addressed in this chapter is the issue of scale of objects and salient regions in the image (see, for instance, Jägersand 1995). What, for instance, happens when an object is much smaller than a selected region, or when more than one object happen to be present in the region? It is conceivable that in such cases the object recognition algorithm could give feedback to the attention algorithm, which would then refine the extent and shape of the region based on information about the identity, position, and scale of objects. This scheme may be iterated until ambiguities are resolved, and it would lead to object-based attention (see chapter 3).

At the other extreme, an object could be much larger than the selected regions, and many fixations may be necessary to cover the shape of the object. In this case, visual information needs to be retained between fixations and integrated into a single percept (Rybak et al. 1998). When hypotheses about the object identity arise during the first few fixations, attention may be guided to locations in the image that are likely to inform a decision about the correctness of the hypotheses.

Chapter 6

Detection and Tracking of Objects in Underwater Video

6.1 Introduction

In chapter 5 we demonstrated the application of the saliency-based attention system introduced in chapter 2 to solve learning and recognition of multiple objects in single scenes and objects in cluttered scenes. In this chapter we show how the same basic principles can be applied to the detection and tracking of objects in a multiple target tracking scenario. In particular, we are interested in detecting and tracking objects in underwater video used to estimate population statistics of marine animals. This task is challenging because of the low contrast and the large amount of clutter in the video. However, human annotators can learn this task in a matter of months. This led us to look at our model of selective visual attention in humans for insights into how we might be able to tackle this hard problem with biologically inspired algorithms.

This work is a collaboration with the Monterey Bay Aquarium Research Institute (MBARI). After extensive consultation with professional video annotators at MBARI, I designed and implemented the attention and tracking system, initially as part of the iLab Neuromorphic Vision C++ Toolkit. Karen Salamy set up the computer infrastructure at MBARI and conducted the evaluations in subsection 6.4.1. Danelle Cline set up processing on the Beowulf computer cluster at MBARI, and she conducted the evaluations in subsection 6.4.2. Rob Sherlock was the expert annotator for subsection 6.4.2. As the group manager at MBARI, Dr. Duane Edgington provided organizational support for the project throughout. He and I initiated the project during the 2002 Workshop for Neuromorphic Engineering in Telluride, Colorado, and the initial phase was supported by a collaborative research grant by the Institute for Neuromorphic Engineering.

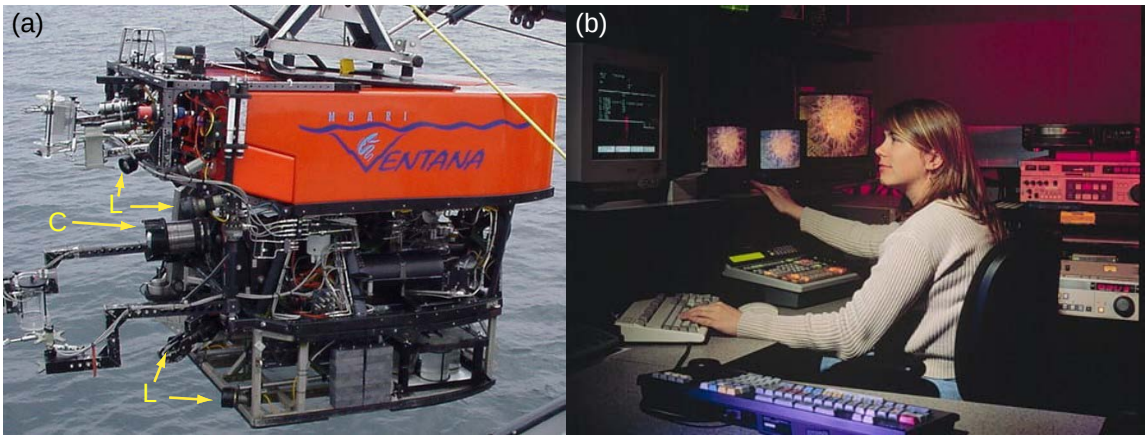

Figure 6.1: (a) ROV Ventana with camera (C) and lights (L). (b) Manual annotation of video tapes in the video lab on shore.

6.2 Motivation

Ocean-going remotely operated vehicles (ROVs, figure 6.1 a) increasingly replace the traditional tow net approach of assessing the kinds and numbers of animals in the oceanic water column (Clarke 2003). At MBARI, high-resolution video equipment on board the ROVs is used to obtain quantitative video transects (QVTs) through the ocean midwater, from 50 m to 1000 m depth. QVTs are superior to tow nets in assessing the spatial distribution of animals and in recording delicate gelatinous animals that are destroyed in nets. Unlike tow nets, which integrate data over the length of the tow, QVTs provide high-resolution data at the scale of the individual animals and their natural aggregation patterns for animals and other objects larger than about 2 cm in length (Robison 2000).

However, the current manual method of analyzing QVT video material is labor intensive and tedious. Highly trained scientists view the video tapes, annotate the animals, and enter the annotations into a data base (figure 6.1b). This method poses serious limitations to the volume of ROV data that can be analyzed, which in turn limits the length and depth increments of QVTs as well as the sampling frequency that are practical with ROVs (Edgington et al. 2003; Walther and Edgington 2004).

Being able to process large amounts of such video data automatically would lead to an order-of-magnitude shift in (i) lateral scale of QVTs from current 0.5 km to mesoscale levels (5 km); (ii) depth increment from current 100 m to the biologically significant 10 m scale; and (iii) sampling frequency from currently monthly to daily, which is the scale of dynamic biological processes. Such an increase in data resolution would enable modeling of the linkage between biological processes and physicochemical hydrography.

6.3 Algorithms

We have developed an automated system for detecting and tracking animals visible in ROV video (Walther et al. 2004a; Edgington et al. 2003). This task is difficult due to the low contrast of many of the marine animals, their sparseness in space and time, and debris ("marine snow") cluttering the scene, which shows up as ubiquitous high contrast clutter in the video.

Our system consists of a number of sub-components whose interactions are outlined in figure 6.2. The first step for all video frames is the removal of background. Next, the first frame and every pth frame thereafter (typically, $p = 5$) are processed with an attentional selection algorithm to detect salient objects. Detected objects that do not coincide with already tracked objects are used to initiate new tracks. Objects are tracked over subsequent frames, and their occurrence is verified in the proximity of the predicted location. Finally, detected objects are marked in the video frames.

6.3.1 Background Subtraction

Images captured from the video stream often contain artifacts such as lens glare, parts of the camera housing, parts of the ROV, or instrumentation (figure 6.3). Also, non-uniform lighting conditions cause luminance gradients that can be confusing. All of these effects share the characteristic that they are constant over medium or long periods of time, unlike the apparently fast moving objects in the water. Hence we can remove them by background subtraction (x, y, and t are assumed to be discrete):

$$I'(x,y,t) = \left[I(x,y,t) - \frac{1}{\Delta t_b} \sum_{t'=(t-\Delta t_b)}^{t-1} I(x,y,t') \right]_+ , \tag{6.1}$$

where I is the image intensity before and I' after background subtraction; $[\cdot]_+$ denotes rectification, i.e., setting all negative values to zero. This process is repeated separately for the R, G, and B channels of the color images.

The value of Δt_b should be larger than the typical dwell time of objects in the same position in the camera plane and shorter than the timescale of changes in the artifacts. In our transect videos, objects typically move fast. We found that $\Delta t_b = 0.33$ s (10 frames) works quite well, giving us enough flexibility to adjust to changes in the artifacts quickly (figure 6.4b).

6.3.2 Detection

We use the model of saliency-based bottom-up attention described in chapter 2 for the detection of new objects. Following background subtraction, input frames are decomposed into seven channels (intensity contrast, red/green, and blue/yellow double color opponencies, and the four canonical spatial orientations) at six spatial scales, yielding 42 "feature maps." After iterative spatial compe-

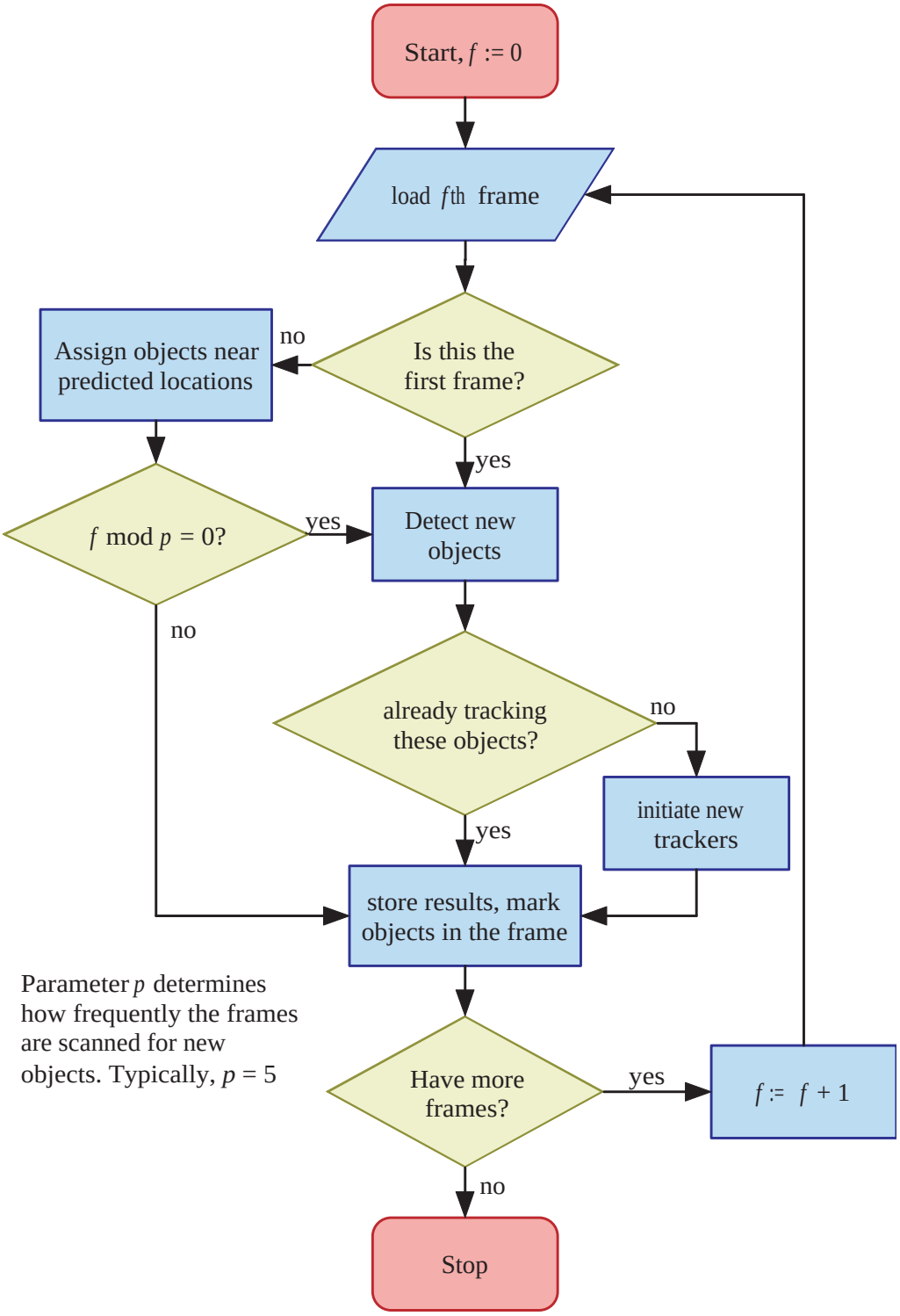

Figure 6.2: Interactions between the various modules of our system for detecting and tracking marine animals in underwater video.

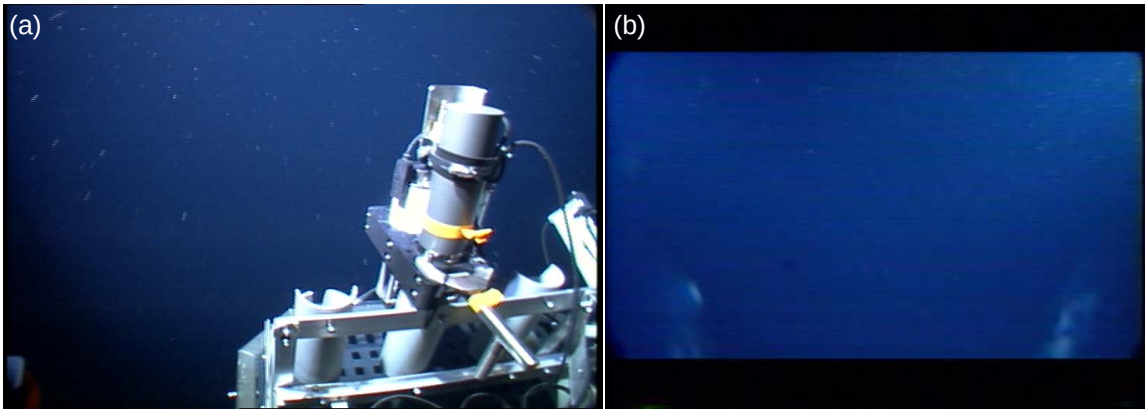

Figure 6.3: Example frames with (a) equipment in the field of view; (b) lens glare and parts of the camera housing obstructing the view.

tition for salience within each map, only a sparse number of locations remain active, and all maps are combined into a unique "saliency map" (figure 6.4c). The saliency map is scanned by the focus of attention in order of decreasing saliency through the interaction between a winner-take-all neural network (which selects the most salient location at any given time) and an inhibition-of-return mechanism (transiently suppressing the currently attended location from the saliency map). Objects are segmented at the salient locations found this way, and their centroids are used to initiate tracking (see subsection 6.3.3).

We found that oriented edges are the most important feature for detecting marine animals. In many cases, animals that are marked by human annotators have low contrast but are conspicuous due to their clearly elongated edges (figure 6.5a), whereas marine snow has higher contrast but lacks a prevalent orientation. In order to improve the performance of the attention system in detecting such faint yet clearly oriented edges, we use a normalization scheme for the orientation filters that is inspired by the lateral inhibition patterns of orientation-tuned neurons in visual cortex.

We compute oriented filter responses in a pyramid using steerable filters (Simoncelli and Freeman 1995; Manduchi et al. 1998) at four orientations. High-contrast "marine snow" particles that lack a preferred orientation often elicit a stronger filter response than faint string-like animals with a clear preferred orientation (figure 6.5c). To overcome this problem, we normalize the response of each of the oriented filters with the average of all of them:

$$O'_i(x,y) = \left[O_i(x,y) - \frac{1}{N} \sum_{j=1}^{N} O_j(x,y) \right]_+ , \tag{6.2}$$

where $O_i(x,y)$ denotes the response of the ith orientation filter ($1 \leq i \leq N$) at position (x,y), and $O'_i(x,y)$ is the normalized filter response (here, $N = 4$). Figure 6.6 shows a possible implementation of this kind of normalization in neurons, using an inhibitory interneuron, which represents the sum

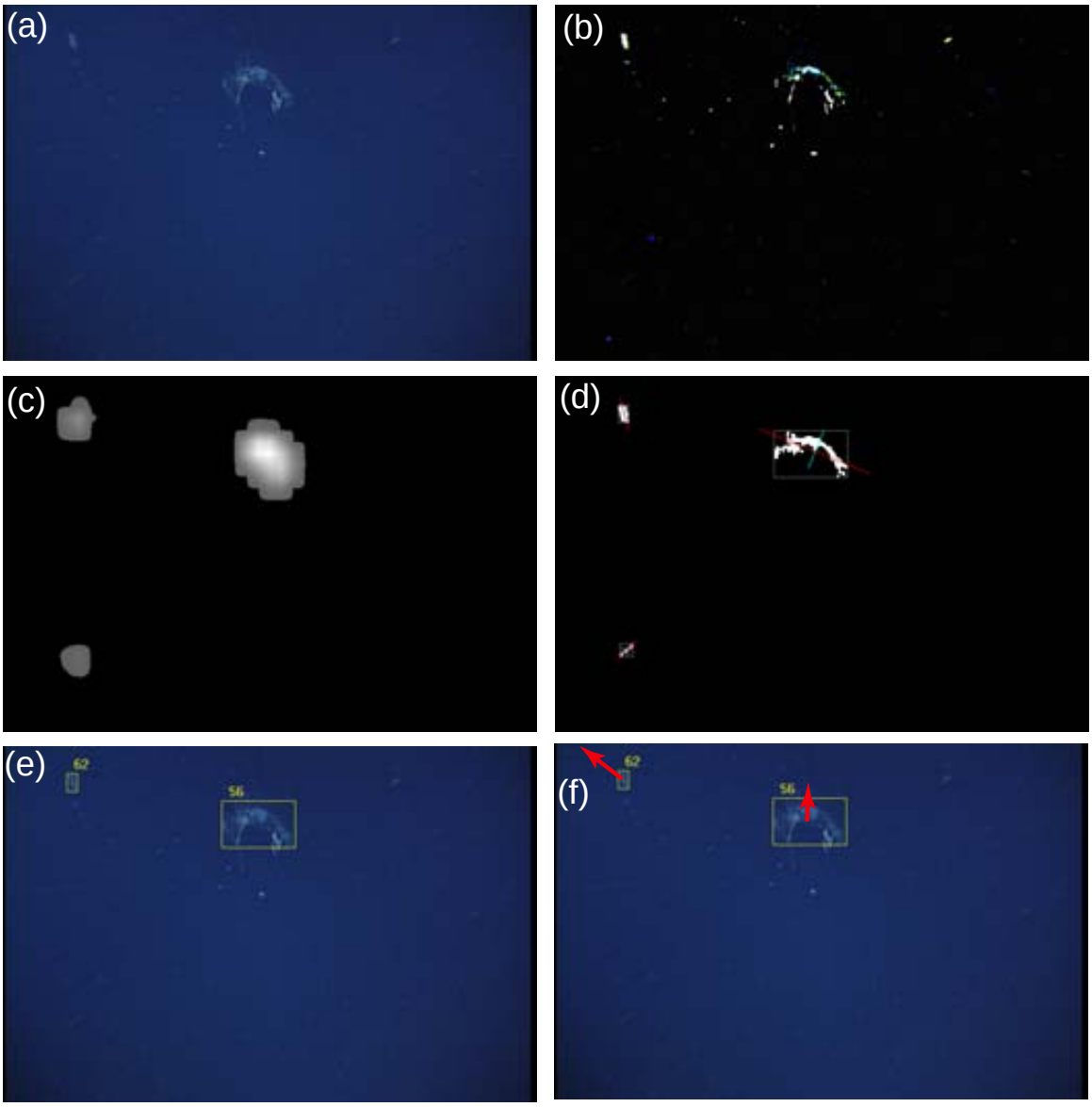

Figure 6.4: Processing steps for detecting objects in video frames. (a) original frame (720×480 pixels, 24 bits color depth); (b) after background subtraction according to eq. 6.1 (contrast enhanced for displaying purpose); (c) saliency map for the preprocessed frame (b); (d) detected objects with bounding box and major and minor axes marked; (e) the detected objects marked in the original frame and assigned to tracks; (f) direction of motion of the object obtained from eq. 6.11.

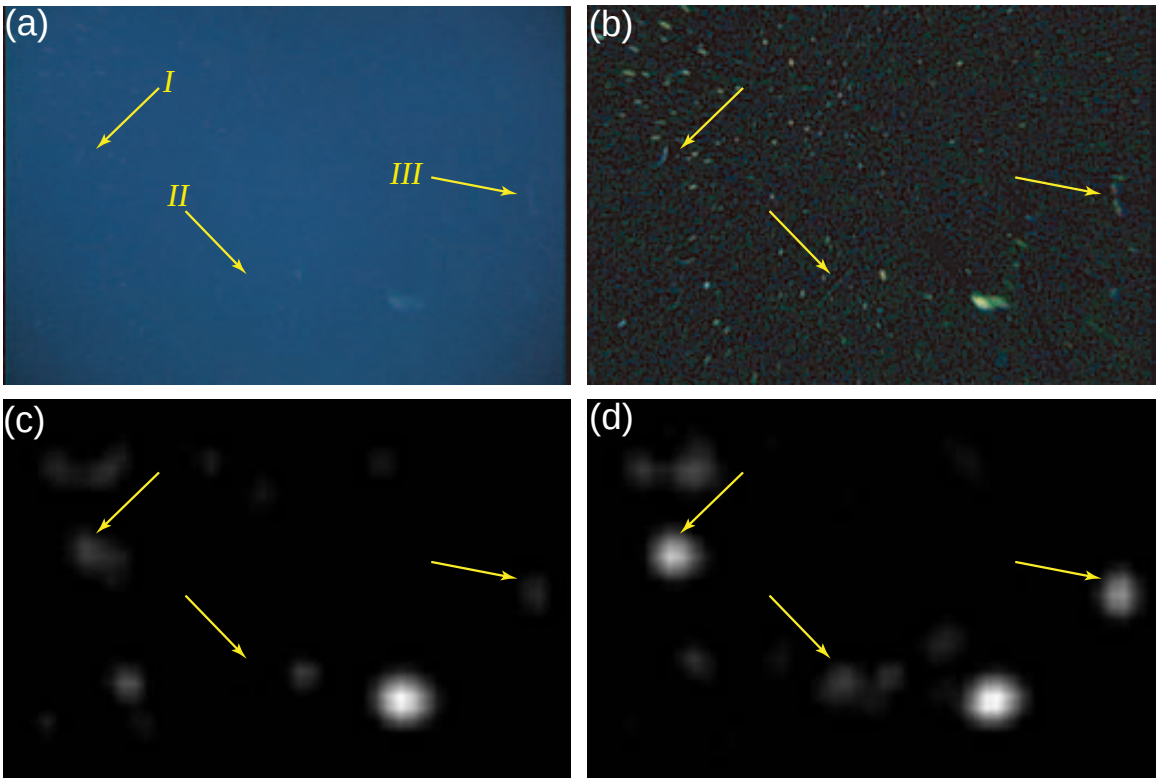

Figure 6.5: Example for the detection of faint elongated objects using across-orientation normalization. (a) original video frame with three faint, elongated objects marked; (b) the frame after background subtraction according to eq. 6.1 (contrast enhanced for illustration); (c) the orientation conspicuity map (sum of all orientation feature maps) without across-orientation normalization; (d) the same map with across-orientation normalization. Objects I and III have a very weak representation in the map *without* normalization (c), and object II is not represented at all. The activation to the right of the arrow tip belonging to object II in (c) is due to a marine snow particle next to the object and is not due to object II. Compare with (d), where object II as well as the marine snow particle create activation. In the map *with* normalization (d), all three objects have a representation that is sufficient for detection.

on the right-hand side of eq. 6.2.

Although this simple model of across-orientation normalization falls short of modeling the full array of long and short range interactions found in primary visual cortex (DeAngelis et al. 1992; Lee et al. 1999; Peters et al. 2005), normalization leads to a clear improvement in detecting faint elongated objects (figure 6.5 d).

6.3.3 Tracking

Once objects are detected, we extract their outline and track their centroids across the image plane using separate linear Kalman filters to estimate their x and y coordinates.

During QVTs the ROV is driven through the water column at a constant speed. While there are some animals that propel themselves at a speed that is comparable to or faster than the speed

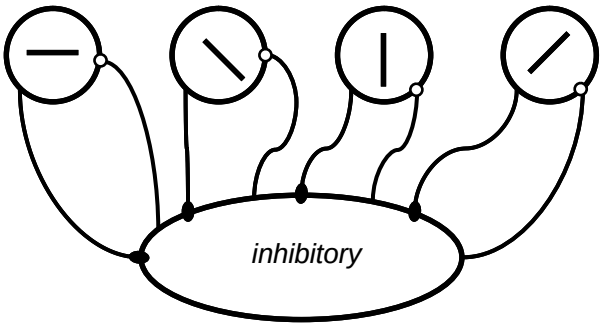

Figure 6.6: A schematic for a neural implementation of across-orientation normalization using an inhibitory interneuron. This circuit would have to be implemented at each image location for this normalization to function over the entire visual field.

of the ROV, most objects either float in the water passively or move on a much slower time scale than the ROV. Hence, we can approximate that the camera is moving at a constant speed through a group of stationary objects.

Figure 6.7 illustrates the geometry of the problem in the reference frame of the camera. In this reference frame, the object is moving at a constant speed in the x and z directions. The x coordinate of the projection onto the camera plane is

$$x'(t) = \frac{x(t) \cdot z_c}{z(t)} = \frac{v_x z_c \cdot t + c_x z_c}{v_z \cdot t + c_z}. \tag{6.3}$$

To a second order approximation, the dynamics of this system can be described by a model that assumes constant acceleration:

$$\frac{d\underline{x}}{dt} = \begin{bmatrix} 0 & 1 & 0 \\ 0 & 0 & 1 \\ 0 & 0 & 0 \end{bmatrix} \underline{x} \tag{6.4}$$

with

$$\underline{x} = \begin{pmatrix} x' \\ v \\ a \end{pmatrix}, \tag{6.5}$$

which results in a fundamental matrix that relates $\underline{x}(t)$ to $\underline{x}(t+\tau)$:

$$\Phi(\tau) = \begin{bmatrix} 1 & \tau & \frac{\tau^2}{2} \\ 0 & 1 & \tau \\ 0 & 0 & 1 \end{bmatrix}. \tag{6.6}$$

$\Phi(\tau)$ is used to define a linear Kalman filter (Kalman and Bucy 1961; Zarchan and Musoff 2000). The deviations of this simplified dynamics from the actual dynamics are interpreted as process noise

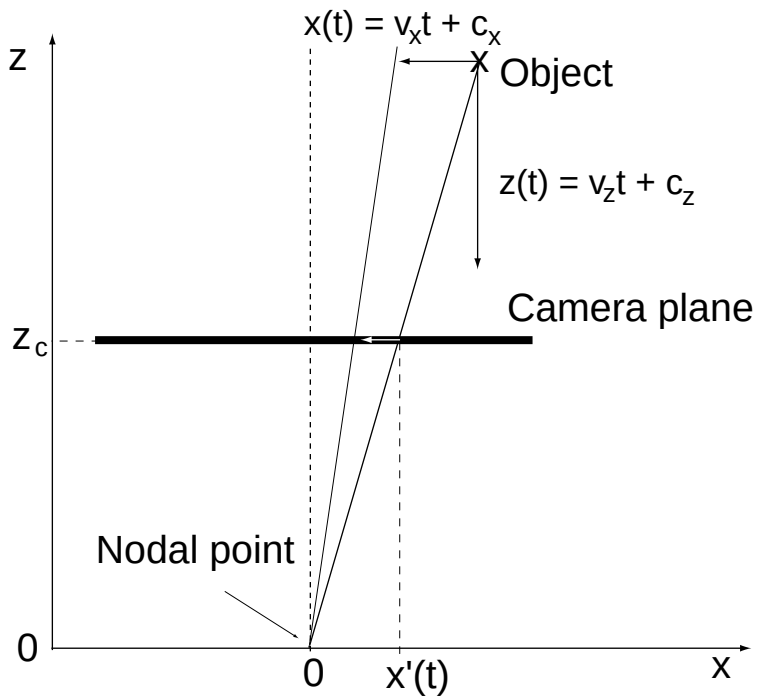

Figure 6.7: Geometry of the projection problem in the camera reference frame. The nodal point of the camera is at the origin, and the camera plane is at z_c. The object appears to be moving at a constant speed into the x and z direction as the camera moves toward the object. Eq. 6.3 describes how the projection of the object onto the camera plane moves in time.

Q. The resulting iterative equations for the Kalman filter are:

$$M_k = \Phi_k P_{k-1} \Phi_k^T + Q, \tag{6.7}$$

$$K_k = M_k H^T \left(H M_k H^T + R \right)^{-1}, \text{ and} \tag{6.8}$$

$$P_k = \left(I - K_k H \right) M_k, \tag{6.9}$$

where P_0 is initialized to a diagonal matrix with large values on the diagonal, $R = [\sigma_m^2]$ is the variance of the measurement noise, $H = [1\ 0\ 0]$ is the measurement matrix relating the measurement x^M to the state vector $\underline{x}$. Q is the process noise matrix:

$$Q(\tau) = \sigma_p^2 \begin{bmatrix} \frac{1}{20}\tau^5 & \frac{1}{8}\tau^4 & \frac{1}{6}\tau^3 \\ \frac{1}{8}\tau^4 & \frac{1}{3}\tau^3 & \frac{1}{2}\tau^2 \\ \frac{1}{6}\tau^3 & \frac{1}{2}\tau^2 & \tau \end{bmatrix}, \tag{6.10}$$

where σ_p^2 is the variance of the process noise. For our particular tracking problem we found $\sigma_m^2 = 0.01$ and $\sigma_p^2 = 10$ to be convenient values.

Once the Kalman matrix K_k is obtained from eq. 6.8, an estimation for $\underline{x}_k$ can be computed

from the previous state estimate $\underline{\hat{x}}_{k-1}$ and the measurement x_k^M:

$$\underline{\hat{x}}_k = \Phi_k \underline{\hat{x}}_{k-1} + K_k(x_k^M - H\Phi_k \underline{\hat{x}}_{k-1}). \tag{6.11}$$

When no measurement is available, a prediction for $\underline{x}_k$ can be obtained by extrapolating from the previous estimate:

$$\underline{\hat{x}}_k = \Phi_k \underline{\hat{x}}_{k-1}. \tag{6.12}$$

For the initiation of the tracker we set $\underline{\hat{x}}_0 = [x_0^M \ 0 \ 0]^T$, where x_0^M is the coordinate of the object's centroid obtained from the saliency-based detection system described in the previous section.

We employ the same mechanism to track the y coordinate of the object in the camera plane. Whenever the x or y coordinate tracker runs out of the camera frame, we consider the track finished and the corresponding object lost. Re-entry of objects into the camera frame almost never occurs in our application. We require that an object is successfully tracked over at least five frames, otherwise we discard the measurements as noise.

In general, we are tracking multiple objects all at once. Normally, multi-target tracking raises the problem of assigning measurements to the correct tracks (Kirubarajan et al. 2001). Since the attention algorithm only selects the most salient objects, however, we obtain a sparse number of objects whose predicted locations are usually separated far enough to avoid ambiguities. If ambiguities occur, we resolve them using a measure that takes into account the Euclidean distance of the detected objects from the predictions of the trackers and the size ratio of the detected and tracked objects.

6.3.4 Implementation

We use two ROVs for deep sea exploration, the ROV Ventana and the ROV Tiburon (Newman and Stakes 1994; Mellinger et al. 1994). ROV Ventana (figure 6.1a), launched from R/V Point Lobos, uses a Sony HDC-750 HDTV (1035i30, 1920x1035 pixels) camera for video data acquisition, and the data are recorded on a DVW-A500 Digital BetaCam video tape recorder (VTR) on board the R/V Point Lobos. ROV Tiburon operates from R/V Western Flyer; it uses a Panasonic WVE550 3-chip CCD (625i50, 752x582 pixels) camera, and video is also recorded on a DVW-A500 Digital BetaCam VTR. On shore, a Matrox RT.X10 and a Pinnacle Targa 3000 Serial Digital Interface video editing card in a Pentium P4 1.7 GHz personal computer (PC) running the Windows 2000 operating system and Adobe Premier are used to capture the video as AVI or QuickTime movie files at a resolution of 720 x 480 pixels and 30 frames per second. The frames are then converted to Netpbm color images and processed with our custom software.

All software development is done in C++ under Linux. To be able to cope with the large amount

Table 6.1: Single frame analysis results.

	Image set 1	Image set 2
Date of the dive	06/10/2002	06/18/2002
ROV used for the dive	*Tiburon*	*Ventana*
Number of images obtained	456	1004
Images without animals	205	673
Images with detected animals	224	291
Images with missed animals	27	40

of video data that needs to be processed in a reasonable amount of time, we deployed a computer cluster with 8 Rack Saver rs1100 dual Xeon 2.4 GHz servers, configured as a 16 CPU, 1 Gigabit per second Ethernet Beowulf cluster. We currently process approximately three frames per second on each of the Xeon nodes at a resolution of 720×480 pixels.

6.4 Results

We present two groups of results – an assessment of the attentional selection algorithm for our purpose and a comparison of the automatic processing of three 10 minute video clips with expert annotations.

6.4.1 Single Frame Results

In order to assess the suitability of the saliency-based detection of animals in video frames in the early stage of our project, we analyzed a number of single video frames. We captured the images from a typical video stream at random. We analyzed two image sets – one with 456 images from video recorded by ROV Tiburon on June 10, 2002 and one with 1004 images from video recorded by ROV Ventana on June 18, 2002. Only some of the images in the sets contain animals. We used the attentional detection system described in subsection 6.3.2 to evaluate its performance on these images. We counted the number of images in which the most salient location, i.e., the location first attended to by the algorithm, coincides with an animal. The results are displayed in table 6.1.

In the images that did not contain animals the saliency mechanism identified other visual features as being the most salient ones, usually particles of marine snow. Originally, the system had no ability to identify frames that did not contain any objects of interest. We introduced this concept when we implemented tracking of objects (see subsection 6.3.3). For the majority of the images that did contain animals, the saliency program identified the animal (or one of the animals if more than one were present) as the most salient location in the image. In image set 1 the animals were identified as the most salient objects in 89% of all images that contained animals. In image set 2 this was the case for 88% of the images with animals. Ground truth was established by individual inspection of

Table 6.2: Results from processing four quantitative video transects.

Video Clip (10 min duration each)	**A**	**B**	**C**	**D**
Dive depth	400 m	50 m	1000 m	900 m
Number of animals annotated by person	122	57	29	29
Of those, found by the software	102 (84 %)	40 (70 %)	25 (86 %)	21 (72 %)
Missed by the software	20 (16 %)	17 (30 %)	4 (14 %)	8 (28 %)
Found by the software but missed by the person	5	2	3	4

the test images.

6.4.2 Video Processing

As a test of the video processing capabilities of our system, we processed four 10 min video segments that had previously been annotated by scientists. Table 6.2 shows the results. Our system missed on average 21 % of the annotated objects in the video clips. In several cases, our automated detection system detected animals that the annotators had missed. The program also detected several other objects that the scientists had not annotated. However, we did not consider these cases as false positives because a classification system capable of recognizing species would also be able to distinguish target animals from salient debris. The big advantage of the attention and tracking system is a massive reduction of data by 95–98 % for subsequent processing by a classification system.

Almost all misses by the software are of the sub-class Siphonophora, which are long string-like colonial animals that yield very low contrast in the video frames. Interestingly, most of the animals that were initially missed by the scientist were of the same sub-class.

Since our system can detect and track objects in the video fairly consistently, it can be used to summarize longer video segments by displaying a collection of small thumbnail video clips that show the most interesting parts of the original video. The individual frames for these thumbnail clips can be extracted automatically from the segmentation and tracking results. This mode is best described as a virtual camera following individual objects in the video. Using such automatic indexing, scientists would be able to grasp the most interesting parts of a particular video quickly without having to review the entire tape. Once these miniature clips are made part of the existing video annotation reference system (VARS 2005), they will help users identify potentially relevant tapes in the existing large collection of video data.

6.5 Discussion

We have presented a new method for processing video streams from ROVs automatically. This technology has a potentially significant impact on the daily work of video annotators by aiding their

analysis of noteworthy events in video. After continued refinement we hope that the software will be able to perform a number of routine tasks fully automatically, such as "outlining" video, analyzing QVT video for the abundance of certain easily identifiable animals, and marking especially interesting episodes in the video that require the attention of the expert annotators.

Beyond its applications to ROV video, our method for automated underwater video analysis may potentially have a larger impact by enabling Autonomous Underwater Vehicles (AUVs) to collect and analyze quantitative video transects, with the potential to sample more frequently and at an ecologically significant finer spatial resolution and greater spatial range than is practical and economical for ROVs. We also see great benefit in automating portions of the analysis of video from fixed observatory cameras, where autonomous response to potential events (e.g., pan and zoom to events) and automated processing for science users of potentially very sparse video streams from hundreds of network cameras could be key to those cameras being practical scientific instruments.

In chapter 5 we showed that our attentional selection model can successfully cue object recognition systems for learning and recognition of multiple objects. In this chapter we have demonstrated the use of such an algorithm for multi-target tracking. In particular, the selective attention system detects the targets for track initiation completely automatically. Saliency-based filtering of targets even before resources are spent on tracking them saves computational resources, and it drastically reduces the complexity of the assignment problem in multi-target tracking.

Part III

Psychophysics

Chapter 7

Measuring the Cost of Deploying Top-down Visual Attention

7.1 Introduction

Imagine walking into a crowded restaurant, looking for your friend whom you are supposed to meet. You will be looking around, scanning the faces of the patrons for your friend's without paying much attention to the interior design or the furniture. Entering the same restaurant with the intention of finding a suitable table, on the other hand, will have you looking at pretty much the same scene, and yet your perception will be biased for the arrangement of the furniture, mostly ignoring the other guests.

Task or agenda affect our visual perception by a set of processes that we commonly term top-down attention, to distinguish them from stimulus-driven bottom-up attention (Treisman and Gelade 1980; Itti and Koch 2001a). It enables us to preferentially perceive what is important for the task at hand. Without top-down attention to the relevant parts of a scene, we may even miss large changes (Rensink et al. 1997; Simons and Levin 1998; Simons and Rensink 2005) until we are explicitly cued, for instance by pointing (exogenous cue) or by describing the changed part of the image (endogenous cue). If cueing changes our visual perception so effectively, what is the cost of deploying attention to a new task?

Humans can detect object categories in natural scenes in as little as 150 ms (Thorpe et al. 1996; Potter and Levy 1969), and Li et al. (2002) demonstrated that this can be achieved even when spatial attention is tied to a demanding task elsewhere in the visual field. At this fast processing speed, there is not enough time for feedback within the visual hierarchy, suggesting purely feed-forward, bottom-up processing. Because of their block design, these experiments allow subjects to prepare for the given task well in advance, giving them ample time to bias their visual system accordingly. Here we are interested in the reaction time cost for adjusting the visual system for a new task from trial to trial. Thus, we ask how efficient it is to bias the visual system from the top down to allow

for subsequent efficient processing of stimuli in a purely bottom-up fashion.

Wolfe et al. (2004) approached a similar question for visual search by cueing odd-one-out search tasks in sets of 6–18 items, finding a reaction time cost of up to 200 ms for picture cues and 700 ms for word cues for the mixed versus blocked condition. These endogenous cues take about 200 ms to become fully effective. However, with their design Wolfe et al. (2004) were not able to separate the cost for deploying top-down attention from the cost for other processes such as perceiving and interpreting the cue.

We address this question by adapting the task switching paradigm, recently reviewed by Monsell (2003), to fast natural scene categorization tasks (Walther et al. 2006). Task switching was introduced by Jersild (1927), who had students work through lists of simple computation tasks (adding and subtracting 3 from numbers). He found that blocks, in which the two tasks alternate, require considerably more time than blocks with single tasks. This result was later verified by Spector and Biederman (1976).

In general, task switching experiments require subjects to perform two or more tasks that typically relate to different attributes of the stimulus, e.g., reporting whether a number is odd or even vs. whether it is larger or smaller than 5. Subjects are tested in blocks with single tasks and in mixed task blocks. In mixed blocks the tasks can either alternate in a prespecified sequence, e.g. "AABBAABB" (Allport et al. 1994; Rogers and Monsell 1995; De Jong 2000), or the task order can be unpredictable, and a task cue is presented before stimulus onset (Sudevan and Taylor 1987; Meiran 1996). See Koch (2005) for a comparison of the two paradigms.

In either case, there will be trials with task repeats and trials with task switches. Reaction times (RTs) tend to be longer for switch trials than for repeat trials. The difference is termed "switch cost." Even though no actual switch needs to happen in repeat trials, RTs will still be longer than in single task blocks, giving rise to a "mixing cost." Both switch and mixing cost depend on the preparation time from the presentation of the cue or, in the absence of a cue, from the end of the previous trial to the stimulus onset of the current trial. It is frequently observed that even with long preparation times of up to 5 seconds, there is still a considerable residual cost (Sohn et al. 2000; Kimberg et al. 2000).

Switch cost is generally assumed to be due to task-set reconfiguration, including a shift of attention between stimulus attributes, selection of the correct response action, and, depending on the task, reconfiguration of other task-specific cognitive processes. Mixing cost captures the extra effort involved in *potentially* (but not actually) having to switch to another task compared to a single task condition, such as time for cue perception and interpretation.

When attempting to determine the cost of shifting attention, switch cost is the more interesting effect. However, cost for attention shifts is confounded with other costs such as response selection in its contribution to switch cost. To disentangle these effects, we propose a paradigm with four

tasks divided into two task groups of two tasks each. Tasks within groups relate to the same stimulus attribute and hence do not require an attention shift, while switching between tasks from different groups requires shifting attention to a different stimulus attribute. Since the only difference in within-group versus between-group switches is the necessity to shift attention, the difference in switch cost between the two conditions will give us a measure for its cost.

This project is a collaboration with Dr. Fei-Fei Li. She and I initiated the project and supervised SURF student Lisa Fukui for early pilot studies. I conducted the experiments and analyzed the data reported in this chapter.

7.2 Methods

7.2.1 Subjects

Six right-handed subjects (one female, five male) with normal or corrected to normal vision participated in the experiments, including the author. Subjects (ages 20 to 29, average 23) were recruited from the Caltech academic community and paid for their participation. All subjects passed the Ishihara screening test for color vision without error and gave written informed consent.

One subject's data were excluded from the analysis because his RT was consistently longer than two standard deviations above the RTs of all other subjects.

7.2.2 Apparatus

Stimuli were presented on a 20" Dell Trinitron CRT monitor (1024×768 pixels, 3×8 bit RGB) at a refresh rate of 120 Hz. The display was synchronized with the vertical retrace of the monitor. Stimulus presentation and recording of the subjects' response was controlled with a Pentium 4 PC running Matlab R14 with the psychophysics toolbox (Brainard 1997). Subjects were positioned approximately 100 cm from the computer screen.

7.2.3 Stimuli

Images of the natural or man-made scenes were taken from a large commercially available CD-ROM library and from the world wide web (Li et al. 2002; Thorpe et al. 1996), allowing access to several thousand stimuli. The images were converted to 256 gray levels and rescaled to subtend an area of $4.4^\circ \times 6.6^\circ$ of visual angle. Each image belonged to one of three classes containing a clearly visible animal (e.g., birds, fish, mammals, insects), clearly visible means of transport (e.g., trains, cars, airplanes, bicycles), or neither (distracter images). See figure 7.1 for examples. We used more than 1000 natural scenes of each of these classes, and each image was presented no more than twice during the test sessions.

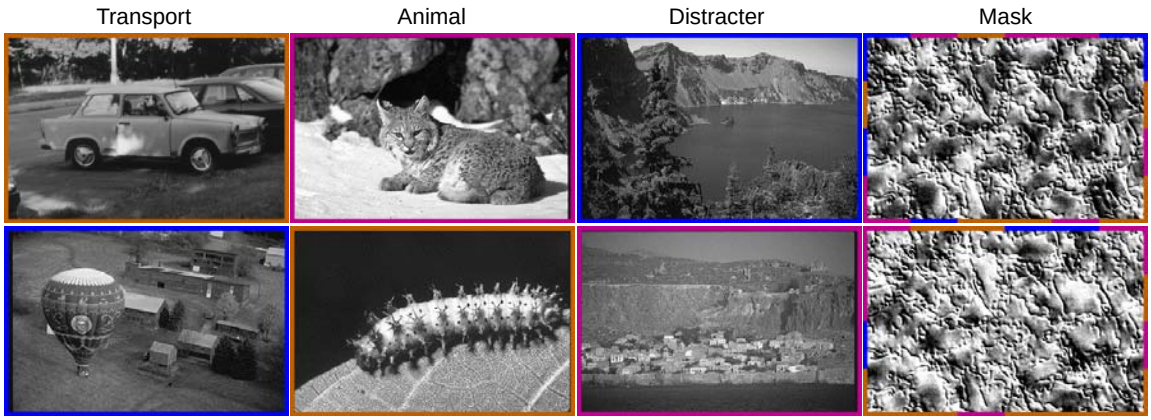

Figure 7.1: Example stimuli for means of transport, animals, and distracters, as well as example masks. Masks are created by superimposing a naturalistic texture on a mixture of white noise at different spatial frequencies (Li et al. 2002), surrounded by a frame with broken-up segments of orange, blue, and purple. Note that the thickness of the color frames is exaggerated threefold in this figure for illustration.

A 2.7' (2 pixels) thick orange, blue, or purple frame surrounds the gray-level images. At full saturation, the CIE coordinates of the colors are (0.666, 0.334), (0, 0), and (0.572, 0), respectively. The purple "distracter" color was chosen such that its hue component (0.875) in HSV space is equidistant from the hue components of the two "target" colors: orange (0.083) and blue (0.667). The brightness (value) of all three colors was adjusted for perceptual equiluminance, using a technique based on minimizing flicker between colors at 14 Hz (Wagner and Boynton 1972). During training, the saturation of the colors was decreased to make the task more difficult. The brightness was adjusted for each saturation level such that perceptual equiluminance between all three colors was maintained. Typically, saturation was decreased to about 0.15 during training, which corresponds to CIE coordinates of (0.360, 0.333) for orange, (0.315, 0.315) for blue, and (0.355, 0.303) for purple.

7.2.4 Experimental Paradigm

The design of our stimuli allows us to define two groups of two tasks each that are as unrelated as possible, while still coinciding spatially. The first group of tasks (IMG tasks) consists of detecting whether an animal is present in the image (cued by the word "Animal") or whether a means of transport is present (cued by "Transport"). This has been shown to be possible without color information (Delorme et al. 2000; Fei-Fei et al. 2005). The second task group (COL tasks) relates to the color of the frame, namely detecting an orange frame ("Orange") or a blue frame ("Blue") around the image. Stimuli are displayed at a random location with fixed eccentricity from fixation to avoid spatial attention effects.

To compare reaction times in situations with and without task switching, two kinds of blocks are used: single task blocks (48 trials) and mixed blocks (96 trials). In single task blocks the task for the

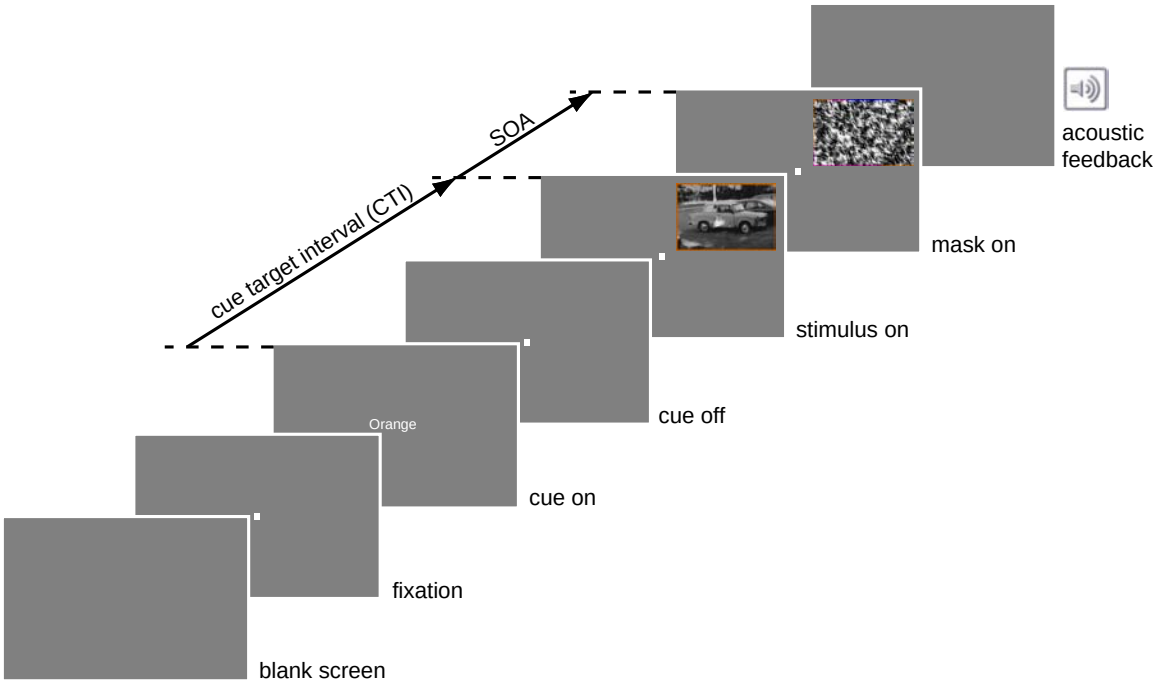

Figure 7.2: Experimental set-up. Each trial starts 1300 ms before target onset with a blank gray screen. At 650 ± 25 ms before target onset, a white fixation dot ($4.1' \times 4.1'$) is presented at the center of the display. At a variable cue target interval (CTI) before target onset, a word cue (0.5° high, between 1.1° and 2.5° wide) appears at the center of the screen for 17 ms (two frames), temporarily replacing the fixation dot for CTIs less than 650 ms. At 0 ms, the target stimulus, consisting of a gray-level photograph and a color frame around it, is presented at a random position on a circle around the fixation dot such that the image is centered around 6.4° eccentricity. After a stimulus onset asynchrony (SOA) of 200–242 ms, the target stimulus is replaced by a perceptual mask. The mask is presented for 500 ms, followed by 1000 ms of blank gray screen to allow the subjects to respond. In the case of an error, acoustic feedback is given (pure tone at 800 Hz for 100 ms), followed by 100 ms of silence. After this, the next trial commences.

entire block is indicated by an instruction screen preceding the block. For mixed blocks subjects are instructed to solve two out of the four possible tasks, either the two IMG tasks, the two COL tasks, or one task from each group. Within each mixed block, equal numbers of trials for the two tasks are shuffled randomly to make their order unpredictable. This procedure results in a statistically equal number of trials with the same task as the preceding trial (repeat) and with the other task (switch). The task for each trial is indicated by a word cue presented at the center of the screen at CTIs of 50 ms, 200 ms, and 800 ms before target onset (figure 7.2). For each block, one CTI is used throughout. For consistency, word cues are presented in both types of blocks, even though they serve no purpose in single task blocks.

On each trial, the probability of seeing a positive (i.e., as cued) example is 50 %, the probability for an example of the non-cued class is 25 %, and the probability for a distracter (non-target) example is 25 %. This is illustrated further in table 7.1. The probabilities for target frame colors

Table 7.1: Stimulus probabilities depending on task.

Task	Animal images	Transport images	Distracter images
"Animal"	50 %	25 %	25 %
"Transport"	25 %	50 %	25 %

orange and blue and the distracter color purple are distributed in an analogous manner.

Subjects are instructed to hold the left mouse button pressed with the index finger of their right hand throughout the block, and to only briefly release it as soon as they detect the cued target property for a given trial. If no response is given within 1500 ms of mask onset, a negative response is assumed (speeded go/no go response). Reaction time is measured for correct positive responses as the time passed between the onset of the target stimulus and the registration of the mouse button release event. If subjects give a positive response, i.e., release the mouse button, the 1000 ms waiting period after the mask is cut short. In case of an error, acoustic feedback is given.

Subjects were trained on single task blocks for 2–3 hours (40–60 blocks of 48 trials). For each image class, a randomly chosen subset of 80 images was set aside and re-used repeatedly for training, but not for testing. During training, the SOA was adjusted in a staircase procedure based on the performance in IMG blocks, starting with an initial 400 ms. A stable target performance between 88 % and 92 % was achieved with SOAs between 200 ms and 242 ms (average 214 ms). The same SOA was also used for COL blocks. To achieve the same level of difficulty, the saturation of the colors was decreased in a staircase procedure, starting with 1 down to between 0.098 and 0.185 (average 0.151). At the end of training, SOA and saturation were fixed for each subject.

The eight one-hour test sessions for each subject consisted of 10 mixed blocks (96 trials) interleaved with 5 single task blocks (48 trials). All positive IMG trials were done with images that the subjects had seen at most once before, thus avoiding overtraining on individual images. The order of blocks with different CTIs and task combinations was randomized within each session and counter balanced across sessions.

7.2.5 Data Analysis

Reaction time was recorded for correct positive trials. After discarding the first trial of each block, trials with a reaction time more than four standard deviations above the mean (above 995 ms) or below 200 ms were discarded as outliers (1 % of the data, see figure 7.3). Error rates and RTs were pooled separately for switch and repeat trials in mixed blocks and over all trials in single task blocks. These block results were pooled separately for each CTI value, and, for some analyses, for each task combination over all sessions for all five subjects (35 sessions in total), and the standard error of the mean (s.e.m.) was computed.

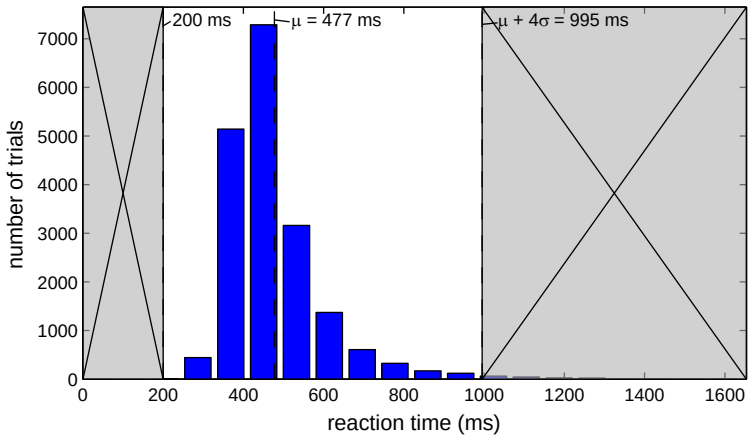

Figure 7.3: Histogram of the reaction times of all trials. Trials with reaction times below 200 ms and more than four standard deviations above the mean (above 995 ms) were discarded as outliers (1 % of the data).

Mixing and switch costs for RT are computed as

$$C^{\mathrm{RT}}_{\mathrm{mix}} = \langle RT_{\mathrm{repeat}} \rangle - \langle RT_{\mathrm{single}} \rangle \text{ and} \tag{7.1}$$

$$C^{\mathrm{RT}}_{\mathrm{switch}} = \langle RT_{\mathrm{switch}} \rangle - \langle RT_{\mathrm{repeat}} \rangle, \tag{7.2}$$

where $\langle \cdot \rangle$ denotes the mean over sessions and subjects. Their standard errors (s. e.) are derived as follows:

$$\mathrm{s.\,e.}(C^{\mathrm{RT}}_{\mathrm{mix}}) = \sqrt{\frac{\mathrm{var}(RT_{\mathrm{repeat}})}{N_{\mathrm{repeat}}} + \frac{\mathrm{var}(RT_{\mathrm{single}})}{N_{\mathrm{single}}}} \text{ and} \tag{7.3}$$

$$\mathrm{s.\,e.}(C^{\mathrm{RT}}_{\mathrm{switch}}) = \sqrt{\frac{\mathrm{var}(RT_{\mathrm{switch}})}{N_{\mathrm{switch}}} + \frac{\mathrm{var}(RT_{\mathrm{repeat}})}{N_{\mathrm{repeat}}}}. \tag{7.4}$$

Analogous formulae are used to compute the mixing ($C^{\mathrm{Err}}_{\mathrm{mix}}$) and switch costs ($C^{\mathrm{Err}}_{\mathrm{switch}}$) for error rate and their standard errors.

The significance of mixing and switch costs is determined by testing whether the two constituent RT or error rate samples are drawn from populations with different means using an unmatched t-test. Mixing and switch costs are further analyzed using N-way ANOVAs. Throughout this chapter, alpha levels of 0.05 (*), 0.01 (**), and 0.005 (***) are reported in figures and tables.

7.3 Results

Figure 7.4 shows RTs and error rates for single task blocks, repeat trials, and switch trials in mixed blocks for the three values of CTI. For single task blocks, RT is independent of CTI. RTs for task

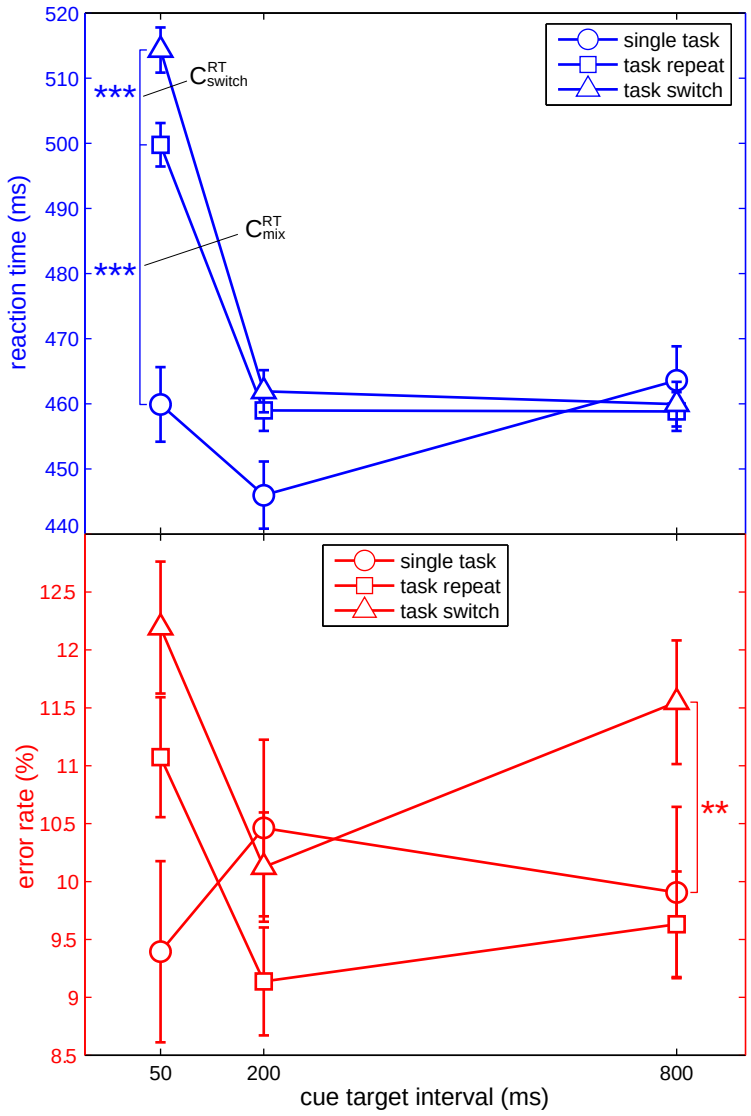

Figure 7.4: Reaction times (top, blue) and error rates (bottom, red) for single task blocks, task repeat trials, and task switch trials in mixed blocks for $n = 5$ subjects. Error bars are s.e.m. For RT, both mixing and switch cost are significant at a CTI of 50 ms, but not at CTIs of 200 ms and 800 ms ($p > 0.05$, t-test). The drop of the single task RT at 200 ms compared to 50 ms and 800 ms is not significant ($p > 0.05$, t-test). For error rate, only switch cost at a CTI of 800 ms is statistically significant. There are no other significant effects for error rate.

repeat and task switch trials are statistically the same as for single task blocks for CTI values 200 ms and 800 ms. At the shortest CTI of 50 ms, there is a significant mixing cost of 39.9 ± 6.6 ms ($p < 10^{-7}$, t-test) and a significant switch cost of 14.5 ± 4.8 ms ($p < 0.005$, t-test). There is a statistically significant switch cost of 1.9 ± 0.7 % ($p < 0.01$, t-test) in error rate at CTI = 800 ms, but no systematic effect is discernible for mixing or switch cost in error rate.

A 3-way analysis of variance (ANOVA) of mixing cost reveals significant main effects for the factors *CTI*, *task group* (COL or IMG), and *subject* for both RT and error rate (table 7.2). Table 7.2

Table 7.2: 3-way analysis of variance with interactions for mixing cost.

Source		**Mixing cost in reaction time**				**Mixing cost in error rate**			
	d.f.	*Mean square*	*F*	*p*		*Mean square*	*F*	*p*	
CTI	2	8261	67.43	$3{\cdot}10^{-13}$	***	50	10.18	$3{\cdot}10^{-4}$	***
task group	1	4490	36.65	$5{\cdot}10^{-7}$	***	56	11.41	0.002	***
subject	4	2735	22.32	$2{\cdot}10^{-9}$	***	13	2.67	0.047	*
CTI * task group	2	864	7.05	0.003	***	43	8.75	0.001	***
CTI * subject	8	350	2.86	0.014	*	17	3.44	0.005	***
task group * subject	4	1048	8.56	$5{\cdot}10^{-5}$	***	7	1.32	0.3	

Table 7.3: 4-way analysis of variance with interactions for switch cost.

Source		**Switch cost in reaction time**				**Switch cost in error rate**			
	d.f.	*Mean square*	*F*	*p*		*Mean square*	*F*	*p*	
CTI	2	915	3.79	0.03	*	6.5	1.06	0.4	
task group	1	168	0.70	0.4		0.2	0.03	0.9	
switch condition	1	1914	7.93	0.009	**	3.9	0.63	0.4	
subject	4	418	1.73	0.2		20.3	3.34	0.02	*
CTI * task group	2	221	0.92	0.4		6.7	1.10	0.3	
CTI * switch condition	2	727	3.01	0.06		5.6	0.92	0.4	
CTI * subject	8	226	0.94	0.5		10.1	1.65	0.2	
task group * switch condition	1	863	3.57	0.07		21.0	3.45	0.07	
task group * subject	4	225	0.93	0.5		8.1	1.32	0.3	
switch condition * subject	4	124	0.52	0.7		7.6	1.25	0.3	

also shows that all two-way interactions reach significance as well, with the exception of *(task group * subject)* for error rate.

As shown in figure 7.5, mixing cost in RT for CTI = 50 ms is significantly higher for IMG (52.5 ± 8.6 ms) than for COL (29.6 ± 5.3 ms) tasks ($p < 0.04$, t-test). On the other hand, mixing cost in error rate is significantly higher for COL (4.2 ± 0.6 %) than for IMG (0.4 ± 1.0 %) tasks ($p < 0.004$, t-test), suggesting a speed-accuracy trade-off.

For analyzing switch cost, we use *switch condition* (within or between task groups) as a fourth variable for the ANOVA and obtain a significant effect for it as well as for *CTI* in RT (table 7.3). The factors *task group* and *subject* are not significant for RT, while *subject* is significant for error rate. None of the two-way interactions is significant.

Note that while mixing cost is significantly affected by all factors (table 7.2), RT switch cost is only dependent on *CTI* and *switch condition* (table 7.3). In particular, the ANOVA for RT switch cost does not show a significant effect for subject identity, indicating that subject-dependent effects are absorbed by mixing cost, keeping switch cost subject independent.

While the dependence of RT switch cost on CTI is apparent from figure 7.4, figure 7.6 illustrates its dependence on the task switch condition for CTI = 50 ms. No significant switch cost was found for switching from IMG to IMG (2.8 ± 8.5 ms, $p > 0.05$, t-test) or from COL to COL (5.1 ± 7.4 ms,

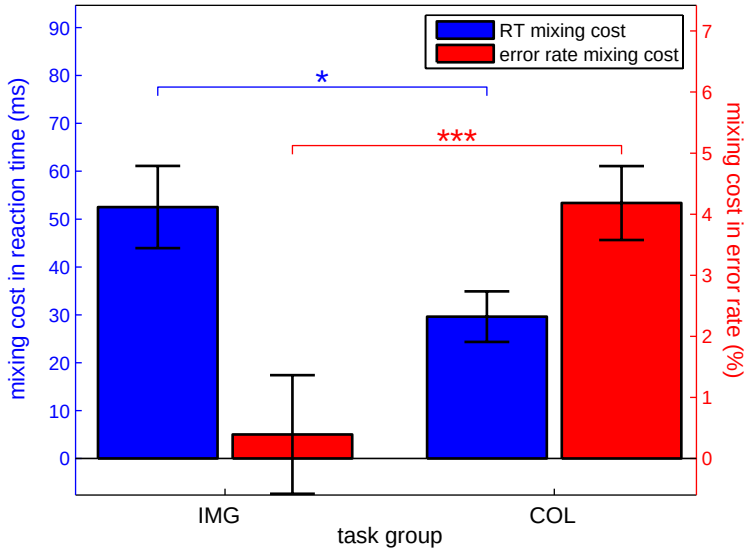

Figure 7.5: Mixing cost in RT (blue) and error rate (red) for all subjects for CTI = 50 ms, plotted by task group. While mixing cost in RT is significantly higher for IMG than for COL tasks, mixing cost in error rate is significantly higher for COL than for IMG tasks.

$p > 0.05$, t-test), but switch cost is significant for switching from COL to IMG (20.0 ± 8.6 ms, $p < 0.05$, t-test) and from IMG to COL (28.4 ± 6.9 ms, $p < 10^{-4}$, t-test).

7.4 Discussion

We set out to find the difference in switch cost of between-group and within-group task switches in order to shed light on the cost of having to shift attention from one stimulus attribute to another. We did indeed find significant RT switch costs of 20 ms (COL to IMG) and 28 ms (IMG to COL) for between-group switches, but no significant switch cost for within-group switches. The only difference between these two switch modes is that between-group switching requires the shift of attention to another stimulus attribute, while within-group switching does not. We conclude that the RT cost of having to shift attention in our fast detection paradigm is 20–28 ms.

Both mixing and switch cost in RT are significant only for a CTI of 50 ms, but not for 200 ms or longer. This agrees with the results in visual search by Wolfe et al. (2004) who found that cueing becomes fully effective within 200 ms from cue onset. This means that a CTI of 200 ms is sufficient to perceive the cue and shift attention to the cued stimulus attributes without incurring a reaction time penalty compared to perceiving the cue and not having to shift attention. Thus, 200 ms is an upper bound on the time it takes to shift attention. Presenting the cue with a CTI of 50 ms still allows subjects to perform the task (no significant switch cost in error rate), but at a penalty of 20–28 ms in RT if an attention shift is required.

What happened to the other contributors to switch cost, in particular remapping of the motor

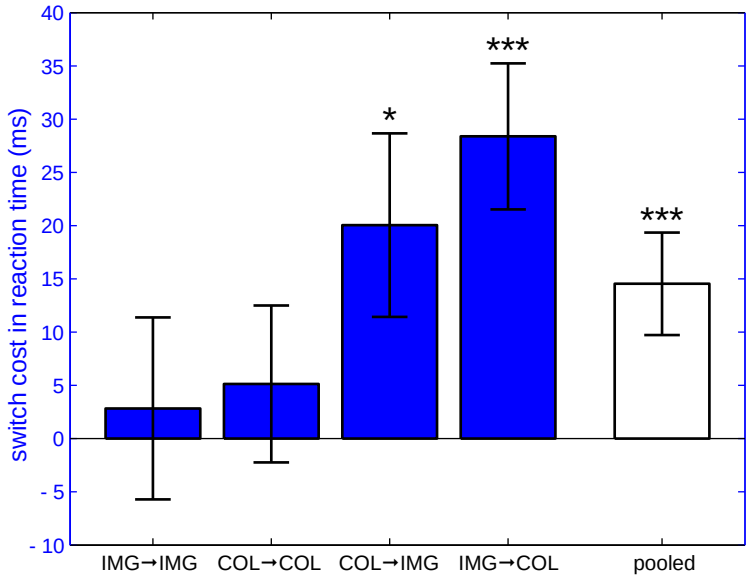

Figure 7.6: Switch cost in RT at a CTI of 50 ms for different switch conditions (blue) and pooled over all conditions (white). The white bar corresponds to the difference labeled as $C^{\mathrm{RT}}_{\mathrm{switch}}$ in figure 7.4. Error bars are standard errors as defined in eqs. 7.3 and 7.4. Switch cost is only significant when switching between the IMG and COL task groups, but not when switching within the groups.

response? The lack of a significant within-group switch cost suggests that there is no significant cost for this, which appears to contradict the results of Meiran (2000), who found significant contributions of both stimulus and response switching to the switch cost. This discrepancy may be explained by differences in the experimental design. Meiran (2000) as well as the majority of task switching studies (e.g., Rogers and Monsell 1995; Meiran 1996; De Jong 2000; Kleinsorge 2004) use a two-alternative forced choice design, typically instructing subjects to operate two keys with different hands and thus requiring coordination of the motor response across both hemispheres of the brain. Compared to these designs, our go/no go response by releasing a mouse button with only the right hand is rather simple and may not require as much time to be re-assigned, thus accounting for the absence of switch cost for within-group switches.

In their recent ERP and fMRI studies, Rushworth et al. (2005, 2001) used a design where they required subjects to pay attention to the color or the shape of one of two presented stimuli in order to detect a rare target. While they did find significant switch cost in RT, Rushworth et al. (2005, 2001) only considered switches between stimulus attributes, but they did not compare them with switches within attributes.

Switch cost is believed to arise when residual activity in the neural cicuitry for the previous task interferes with performance in the current task. Using face and word discrimination tasks that activate well-known brain regions, Yeung et al. (2006) were able to demonstrate this process in prefrontal cortex using fMRI. Their results imply competitive interactions between areas responsible

for the two conflicting tasks, akin to biased competition in the model of selective attention by Desimone and Duncan (1995).

Unlike other task switching studies (e.g. Sohn et al. (2000); Kimberg et al. (2000); Altmann (2004), but see Rogers and Monsell (1995)), we did not find a residual switch cost for long CTIs. There is an ongoing debate in the task switching literature about the factors that affect residual cost.

Although we tried to equalize the difficulty of the two task groups during training, there is a significantly higher RT mixing cost for IMG (53 ms) than for COL (30 ms) tasks, which might be compensated by an opposite effect in error rate mixing cost (0.4 % for IMG, 4.2 % for COL) in a speed-accuracy trade-off. Switch cost, on the other hand, does not depend on task group. The paradigm of distinguishing mixing and switch cost allows us to catch such variations in the mixing cost while keeping switch cost unaffected by them.

We see a similar effect in inter-subject variability. While RT mixing cost shows significant dependence on subject identity, there is no such dependency for RT switch cost. This suggests that the processes involved in shifting attention are stereotypical among individuals, implying an automated process with fixed processing duration. Mixing cost, on the other hand, shows more individual differences in processes such as cue perception and interpretation and additional effort for having to potentially solve two tasks instead of one.

What do our results mean for the top-down control of visual perception? Due to its short processing time, fast object detection in natural scenes of the sort shown by Thorpe et al. (1996) is assumed to be possible in a purely feed-forward, hierarchical model of the ventral pathway (Thorpe et al. 2001; Riesenhuber and Poggio 1999b). Switching top-down attention to a different feature value within the same stimulus attribute requires biasing feed-forward connections in such a hierarchical system at fairly high levels (see chapter 4 for a computational model), e.g., in inferotemporal cortex (IT) or even the connections from IT to prefrontal cortex (PFC) for object categories (Freedman et al. 2003). For example, two different classifiers, possibly located in the PFC, would access the same data in IT to decide whether or not an animal or a vehicle is present in the image (Hung et al. 2005).

When switching to a different stimulus attribute processed by a different visual area, one would assume that task-specific biasing of neural activity has to happen at an earlier stage in the hierarchy, before specialization of processing streams takes place. In the case of switching between color and object detection, this could be area V4, V2, or even V1. Our current results indicate a higher cost in RT for task switches between attributes, i.e., for biasing at an earlier stage, than within attributes, i.e., biasing at a later, more specialized stage. This finding agrees with ideas of a reverse hierarchy put forward by Hochstein and Ahissar (2002).

Chapter 8

Conclusions

8.1 Summary

In this thesis we have introduced a model of bottom-up attention to salient regions based on low-level image properties, and we have demonstrated its use in a variety of applications in computational modeling of biological vision and in machine vision. Furthermore, we have modeled feature sharing between object recognition and top-down attention, and we have measured the cost of deploying top-down attention.

Our model of salient region detection, described in detail in chapter 2, provides a solution for the problem of identifying a region that is likely to contain an object even before objects are recognized. Selecting the salient region relies on neuronal feedback connections in the system of maps and pyramids that are derived from low-level image properties to compute the saliency map. All processing steps are biologically plausible, and there is little computational overhead on top of the operations required to compute saliency in the conventional way.

In chapter 3 we added salient region selection to a biologically plausible model of object recognition in cortex by Riesenhuber and Poggio (1999b) in order to facilitate sequential recognition of several objects. We have shown that modulation of the activity of units at the V4-equivalent S2 layer by 20–40 % is sufficient to process only the visual information in the attended region, successfully ignoring unattended distracter objects. This is in agreement with several electrophysiology studies that find activity of neurons in area V4 to be modulated by 20–50 % due to selective attention.

Serializing perception and suppressing clutter are also the main mechanisms by which salient region selection proves to be useful for machine vision applications. In connection with grouping based on low-level properties, serializing the perception of a complex scene with multiple objects and clutter provides a way for unsupervised learning of several object models from a single image, as we have shown in chapter 5. By only processing the attended image regions, object detection also becomes more robust to large amounts of clutter.

We have demonstrated in chapter 6 that our model of salient region detection can aid initial

target detection for multi-target tracking and decrease the complexity of the assignment problem by pre-filtering potential target objects. Our application, detecting and tracking low-contrast marine animals in video from remotely operated underwater vehicles, is a first step toward automation of mining this important source of data.

In many situations we direct attention based on a task or agenda from the top down. In chapter 4 we showed that finding useful features for attending to a particular object category can be interpreted as a reversal of processes involved in object detection. We have proposed a model architecture in which this functionality is implemented with feedback connections. We have demonstrated the capabilities of the approach for the example of top-down attention to faces.

Deploying top-down attention comes at a cost in reaction time. We have explored this cost in chapter 7 in psychophysical experiments using a task switching paradigm. By comparing switch costs in task switches that do with those that do not require re-deployment of top-down attention, we found a cost in reaction time of 20–28 ms.

8.2 Future Work

Visual attention and object recognition are tightly interwoven. Many aspects of these interactions are not covered in this thesis or elsewhere in the modeling literature. Our method of salient region selection for attending to proto-objects is only the beginning of an iterative interaction between attention and recognition. Based on initial guesses of the recognition system about the likly identity of the attended item, the attention system should be fine-tuned to allow for fast verification or rejection of hypotheses. Future work should attempt to model these interactions and make predictions about the time course of recognition. These predictions could be tested, for instance, using masking experiment to disrupt the iterations at specific times.

Another interesting aspect of modeling interactions between attention and object recognition is top-down attention for object categories when features are shared among many categories. It is unclear so far how specific intermediate-level features of the type used in chapter 4 are in a scenario with many, e.g. hundreds or thousands, of object categories. Will individual features have enough specificity, or will it be necessary to consider conjunctions of features? The answer to this question has profound implications for the efficiency of visual search for objects.

We demonstrated empirically advantages of spatial grouping based on a biologically inspired concept of saliency for object detection and tracking in machine vision applications. It is not clear, however, if this concept is the best possible one for locating objects based on low-level image properties. Comparison of the statistics of object presence in natural images with the concept of saliency demonstrated here should yield interesting insights into this question.

Attention-based spatial selection and grouping improve efficiency of machine vision algorithms

and enable modes of processing that are not possible otherwise. The exact way in which these improvements can be achieved appear to depend on the recognition algorithm used. It would be interesting to investigate if there are general underlying principles for using attention in object recognition that pervade particular design choices for recognition systems. Such principles might include higher efficiency for matching sets of keypoints, spatial grouping of features to arrive at initial object guesses, or re-balancing of the search for detected object representations in a data base of known objects.

In our psychophysical work, we were able to use task switching to probe for the presence or absence of attention shifts. In future work, this method should be evaluated as a possible probe to determine which tasks require re-orientation of attention. For instance, does switching from a task involving the gist of a scene to a task about foreground objects require a shift of attention? Psychophysical experiments might be supplemented with fMRI (for an example of brain imaging during task switching see Yeung et al. 2006) or event-related EEG.

Appendix

Appendix A

Implementation Details

A.1 Creating the Gaussian Pyramid

In chapter 2 Gaussian pyramids are used in order to compute center-surround differences of various features at various scales. The conventional way of creating the levels of the pyramid consists of two separate steps, convolution with a separable Gaussian filter followed by decimation (Burt and Adelson 1983; Itti 2000). This process is illustrated in figure A.1A for the one-dimensional case, using a convolution kernel of length 3. The first row symbolizes a one-dimensional input image with only one active pixel; the second row shows the result of the convolution; in the third row the image is decimated by discarding all even-numbered pixels (marked with a red cross); and the remaining pixels constitute the resulting subsampled image (fourth row).

It becomes apparent from the figure that computational resources are wasted for computing the convolution for pixels that are later dropped (the gray pixels in this example). This can be avoided by combining the two operations into one integral process, in which convolution is only performed for those pixels that survive subsequent decimation. This saves half of all convolution operations and therefore half of all multiplications. We have implemented this integral operation with separable filters in the iNVT toolkit as well as the SaliencyToolbox. Computing the saliency map for an input image was sped up by 8 % on average by using the functionally equivalent combined operation instead of separate filtering and decimation.

A second problem with the operation as shown in figure A.1A is that the apparent location of the active pixel in the result image is shifted to the right by 1/2 pixel with respect to the input image. If this operation is applied repeatedly, then the systematic error accumulates from layer to layer. In figure A.2A, for instance, the activity caused by the single active pixel at the center of the input image at level 1 moves more and more to the bottom-right corner of the pyramid levels. By level 4, the center is no longer the most active location.

An intuitive solution would be using the average of two neighboring pixels as the pixel activation of the new map, instead of dropping one pixel and retaining the other. In discrete space, averaging

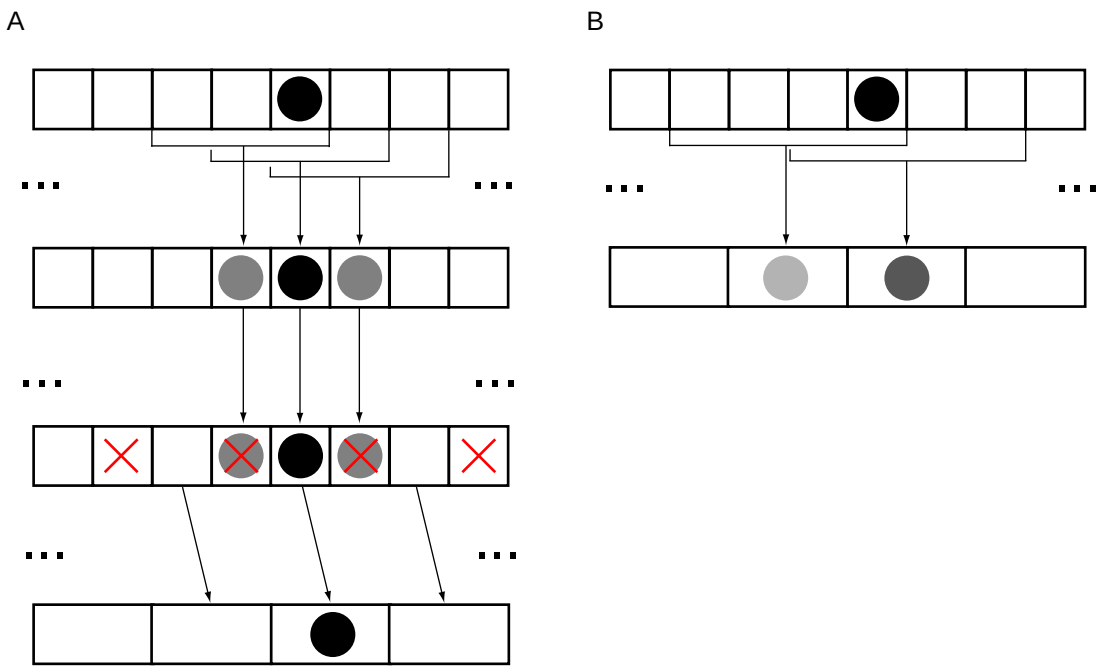

Figure A.1: Illustration of one-dimensional filtering and subsampling. (A) convolution with a filter of length 3 (first to second row), followed by decimation by a factor of 2 (third and fourth row) – the pixels marked with a red cross are removed; (B) integral operation of convolution with a filter of length 4 and decimation by a factor of 2.

over two pixels is equivalent to convolution with the kernel $K_a = [1\ \ 1]/2$. Since filtering itself is a convolution with a kernel K_f, and since convolution is associative, both operations can be combined into convolution with a new filter kernel $K'_f = K_f * K_a$. This new kernel K'_f is one entry larger than the old kernel K_f. Figure A.1B illustrates this principle by using a kernel of length 4, compared to the length 3 kernel in figure A.1A. As explained above, convolution results are only computed for pixels that survive decimation in this integral operation.

Instead of using full two-dimensional convolution for two-dimensional images, separable filters are used that can be applied in the x and y directions separately. Itti (2000), for instance, uses a separable 5×5 convolution filter $K_f = [1\ \ 4\ \ 6\ \ 4\ \ 1]/16$. With dec_x and dec_y being decimation of the image in the x and y directions by a factor of two, pyramid level L_{i+1} would be computed from level L_i as

$$L_{i+1} = \mathrm{dec}_x \left[K_f * \mathrm{dec}_y \left(K_f^T * L_i \right) \right]. \tag{A.1}$$

With $\circ$ being the combined convolution and decimation, we propose to replace eq. A.1 with

$$\begin{aligned} L_{i+1} &= (K_f * K_a) \circ \left[(K_f * K_a)^T \circ L_i \right] \\ &= K'_f \circ \left[\left(K'_f \right)^T \circ L_i \right], \end{aligned} \tag{A.2}$$

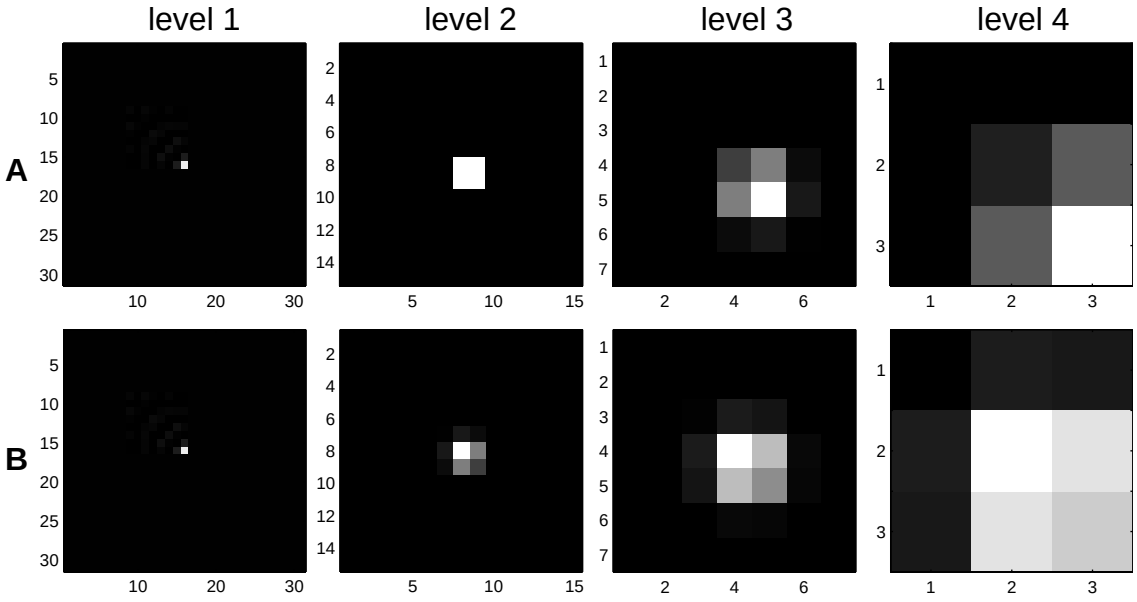

Figure A.2: Example of repeated filtering and subsampling of an image of size 31×31 pixels with only one pixel activated with: (A) a 5×5 filter with subsequent subsampling; and (B) a 6×6 filter with integrated subsampling. Bright pixels indicate high and dark pixels low activity.

where

$$\begin{aligned} K'_f &= K_f * K_a \\ &= [1 \;\; 4 \;\; 6 \;\; 4 \;\; 1]/16 * [1 \;\; 1]/2 \\ &= [1 \;\; 5 \;\; 10 \;\; 10 \;\; 5 \;\; 1]/32 \end{aligned} \tag{A.3}$$

is the new 6×6 separable filter that includes the averaging step. As a general rule, shifting artifacts are best avoided if subsampling by an even factor is accompanied by filtering with a filter of an even length, and subsampling by an odd factor with a filter of an odd length.

We have implemented subsampling according to eq. A.2 with the 6×6 separable kernel from eq. A.3 as part of our SaliencyToolbox (see appendix B). At the image border the filter kernel is truncated. In figure A.2 we show a 31×31 pixels test image with only one active pixel at position $(16, 16)$ being subsampled repeatedly with eq. A.1 (A) and eq. A.2 (B). In (A), the activity due to the active pixel moves toward the bottom-right corner until, at level 4, the bottom-right pixel is the most active instead of the pixel at the center. In (B) the activity caused by the pixel does not move, although activation still appears to spread to the bottom-right quadrant to some extent.

A.2 Color Opponencies for Bottom-up Attention

Red-green and blue-yellow color opponencies are central to modeling the contribution of color to saliency. To this end, the RGB values of the color input image need to be mapped onto a red-green and a blue-yellow opponency axis in a way that largely eliminates the influence of brightness. Hurvich and Jameson (1957) showed that these two opponency axes can cover the entire visible light.

With RGB pixel values (r, g, b), Itti (2000) defines illumination independent hue values for red (R_i), green (G_i), blue (B_i), and yellow (Y_i) as

$$R_i = \left[\frac{r-(g+b)/2}{I_i}\right]_+, \tag{A.4a}$$

$$G_i = \left[\frac{g-(r+b)/2}{I_i}\right]_+, \tag{A.4b}$$

$$B_i = \left[\frac{b-(r+g)/2}{I_i}\right]_+, \text{ and} \tag{A.4c}$$

$$Y_i = \left[\frac{r+g-2\left(|r-g|+b\right)}{I_i}\right]_+ \text{ with} \tag{A.4d}$$

$$I_i = \frac{r+g+b}{3}, \tag{A.4e}$$

where $[\cdot]_+$ denotes rectification. For numerical stability, R_i, G_i, B_i, and Y_i are set to zero at locations with low luminance, i.e., $I < 1/10$, assuming a dynamic range of $[0, 1]$. Red-green (RG_i) and blue-yellow (BY_i) opponencies are defined as

$$RG_i = R_i - G_i \tag{A.5a}$$

$$BY_i = B_i - Y_i, \tag{A.5b}$$

and their center-surround differences are computed across scales as shown in eq. 2.3.

Some of the problems with this definition are illustrated by the examples in table A.1. Orange $(1, 0.5, 0)$, which is perceived as consisting of equal parts of red and yellow, for instance, yields $RG_i = 1.5$, which is half of the value for pure red $(1, 0, 0)$, and $BY_i = -1$, which is only one third of the value for pure yellow $(1, 1, 0)$. For magenta $(1, 0, 1)$, one would expect full positive response from both opponency values, but they are only 0.75 compared to 3.0 for fully saturated red and blue, respectively. Decreasing color saturation by half should lead to a decrease of the color opponency values by half as well. However, for desaturated red $(1, 0.5, 0.5)$, $RG_i = 0.75$ compared to 3.0 for full saturation, while desaturated yellow $(1, 1, 0.5)$ gives $BY = -1.2$, compared to -3.0 for the fully saturated color.

Two main problems need to be addressed to find a better definition of the color opponencies:

Table A.1: Color opponency values for several colors.

Color	(r, g, b)	Itti's definition (eq. A.4) RG_i	BY_i	our definition (eq. A.6) RG_w	BY_w
red	$(1, 0, 0)$	3.0	0.0	1.0	0.0
green	$(0, 1, 0)$	–3.0	0.0	–1.0	0.0
blue	$(0, 0, 1)$	0.0	3.0	0.0	1.0
yellow	$(1, 1, 0)$	0.0	–3.0	0.0	–1.0
orange	$(1, 0.5, 0)$	1.5	–1.0	0.5	–0.5
magenta	$(1, 0, 1)$	0.75	0.75	1.0	1.0
cyan	$(0, 1, 1)$	–0.75	0.75	–1.0	1.0
white	$(1, 1, 1)$	0.0	0.0	0.0	0.0
desaturated red	$(1, 0.5, 0.5)$	0.75	0.0	0.5	0.0
desaturated yellow	$(1, 1, 0.5)$	0.0	–1.2	0.0	–0.5

the definition of yellow and normalization with brightness.

Yellow is perceived as the overlap of red and green in equal parts, so that the amount of yellow contained in an RGB pixel is given by $min(r, g)$. Only amounts of red or green exceeding this value should be counted towards red-green opponency in order to assure independence of the RG and BY opponency axes.

To address the normalization issue, let us consider the colors red $(1, 0, 0)$, blue $(0, 0, 1)$, and magenta $(1, 0, 1)$ for a moment. For red, we would expect $RG = 1$, and for blue, $BY = 1$. Using the average over (r, g, b) as defined in eq. A.4e for normalization leaves us with a normalization factor of 3. For magenta, we would also expect $RG = 1$ and $BY = 1$, but now the normalization factor is 3/2. Cases like these can be reconciled by normalizing with the maximum over (r, g, b) instead of the average.

With these two observations we arrive at our definitions of red-green (RG_w) and blue-yellow (BY_w) color opponencies used in eqs. 2.2 on page 7:

$$RG_w = \frac{r - g}{\max(r, g, b)} \text{ and} \tag{A.6a}$$

$$BY_w = \frac{b - \min(r, g)}{\max(r, g, b)}. \tag{A.6b}$$

RG_w and BY_w are set to zero at locations with $max(r, g, b) < 1/10$.

Table A.1 compares the RG and BY opponencies obtained with eqs. A.4 and A.5 with the values from eqs. A.6. The problems raised with the definition by Itti (2000) are addressed by our new definition of red-green and blue-yellow color opponencies.

Our method of computing color opponencies is implemented as an option in the *iLab Neuromorphic Vision C++ Toolkit* (`http://ilab.usc.edu/toolkit`), and it is the standard method in our SaliencyToolbox (see appendix B).

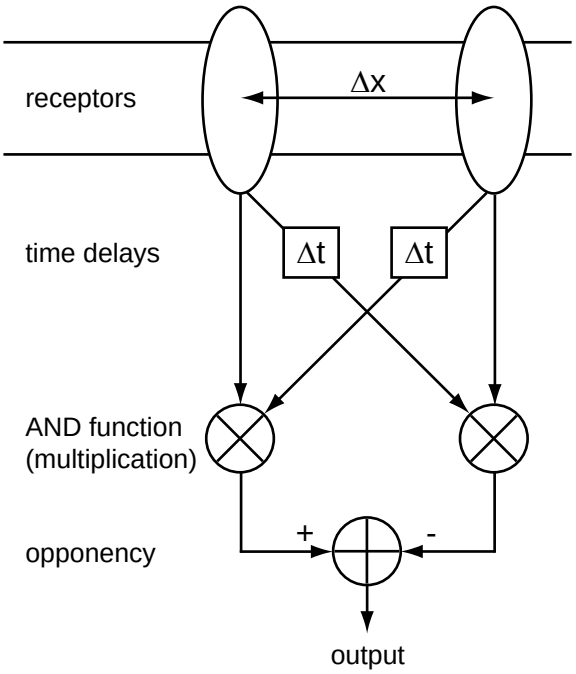

Figure A.3: Schematic of the correlation-based motion detector by Hassenstein and Reichardt (1956). The activation of each receptor is correlated with the time delayed signal from its neighbor. The leftwards versus rightwards opponency operation prevents full field illumination or full field flicker from triggering the motion output signal.

A.3 Motion as a Salient Feature

Motion is a very salient cue for bottom-up attention and should be part of a models of saliency-based attention. Here we describe a simple way of detecting motion that makes use of the existing multi-scale representation of the visual information in pyramids. This work was performed as a SURF project with Chuck Yee during the summer 2002.

Hassenstein and Reichardt (1956) described motion detection in the visual system of the beetle *Chlorophanus* using correlation of signals between adjacent ommatidia with a time delay (figure A.3). Adelson and Bergen (1985) showed the equivalence of the Hassenstein-Reichardt model with a full spatiotemporal energy model of motion under suprathreshold conditions.

Here we adopt this principle to detect motion at multiple scales. If $\mathcal{M}_I(x, y, t)$ is a pixel in the intensity map (eq. 2.1) at position (x, y) and time t, then we can compute the motion opponency maps for left-right ($\leftrightarrow$) and up-down ($\updownarrow$) motion as

$$\mathcal{M}_{\leftrightarrow}(x, y, t) = \mathcal{M}_I(x, y, t - \Delta t) \cdot \mathcal{M}_I(x + \Delta x, y, t) - \mathcal{M}_I(x + \Delta x, y, t - \Delta t) \cdot \mathcal{M}_I(x, y, t), \quad \text{(A.7a)}$$

$$\mathcal{M}_{\updownarrow}(x, y, t) = \mathcal{M}_I(x, y, t - \Delta t) \cdot \mathcal{M}_I(x, y + \Delta y, t) - \mathcal{M}_I(x, y + \Delta y, t - \Delta t) \cdot \mathcal{M}_I(x, y, t). \quad \text{(A.7b)}$$

This is similar in principle, but not in implementation details to the implementation of motion

detection in a Connection Machine by Bülthoff et al. (1989).

Assuming that the origin is in the top-left corner of the image, we obtain maps for individual motion directions as

$$\mathcal{M}_{\leftarrow} = [-\mathcal{M}_{\leftrightarrow}]_+ ; \; \mathcal{M}_{\rightarrow} = [\mathcal{M}_{\leftrightarrow}]_+ ; \; \mathcal{M}_{\uparrow} = \left[-\mathcal{M}_{\updownarrow}\right]_+ ; \; \mathcal{M}_{\downarrow} = \left[\mathcal{M}_{\updownarrow}\right]_+ , \tag{A.8}$$

with $[\cdot]_+$ symbolizing rectification.

The motion detectors in eqs. A.7 are most sensitive to motion velocities $v_x = \Delta x/\Delta t$ or $v_y = \Delta y/\Delta t$, respectively. With Δt fixed to one frame (e.g., 33 ms at a typical frame rate of 30 frames per second), we can obtain a range of velocities by applying eqs. A.7 to multiple levels σ of the intensity pyramid. Because of the dyadic subsampling, a value of $\Delta x = \Delta y = 1$ pixel in level σ will lead to highest sensitivity to motion at a velocity of $v_\sigma = 2^\sigma$ pixels per frame at level σ in the motion detection pyramid.

So far, we have limited the directions of motion to the four cardinal directions, which correspond to motion vectors $(\pm 1, 0)$ and $(0, \pm 1)$. In these cases, eq. A.7 corresponds to correlating an intensity map at time t with a shifted version of the map at time $t - \Delta t$. Shifting by integer pixels is straight forward and easy to implement. It is also possible to consider other directions of motion, e.g., in the diagonal directions with motion vectors $(\pm\sqrt{1/2}, \pm\sqrt{1/2})$. Shifting maps by fractional numbers of pixels is implemented using bilinear interpolation. In our implementation, motion detection with arbitrary motion vectors is possible.

We solve the boundary problem by setting pixels that are shifted into the image to an initial value of zero, and by subsequently attenuating the boundaries in the motion opponency maps to avoid saliency artifacts at the image border.

Allman et al. (1985) report non-classical receptive fields for motion perception in area MT with an excitatory center and an inhibitory surround for a particular direction and speed of visual motion (figure A.4). In their Selective Tuning Model, Tsotsos et al. (1995, 2002, 2005) have modeled these receptive fields using a beam of inhibition around the attended location in a feedback pass.

In the context of sections 2.2 and 2.3, we can model this behavior with the existing center-surround mechanism by applying eq. 2.3 to the motion maps from eq. A.8, redefining L as: $L = L_I \cup L_C \cup L_O \cup L_M$ with $L_M = \{\leftarrow, \rightarrow, \uparrow, \downarrow\}$. Eq. 2.5 can now be applied directly, and eq. 2.6 is extended by a new motion conspicuity map:

$$\mathcal{C}_M = \mathcal{N}\left(\sum_{l \in L_M} \bar{\mathcal{F}}_l\right), \tag{A.9}$$

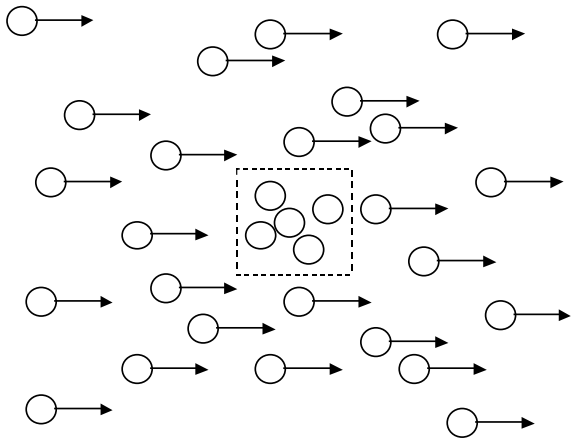

Figure A.4: Illustration of center-surround receptive fields for motion perception. The five dots at the center of the display are salient even though they are stationary because they are surrounded by a field of moving dots.

which contributes to the saliency map, replacing eq. 2.7 by:

$$\mathcal{S} = \frac{1}{4} \sum_{k \in \{I,C,O,M\}} \mathcal{C}_k. \tag{A.10}$$

We have implemented this mechanism for attending to motion as part of the iLab Neuromorphic Vision C++ Toolkit (`http://ilab.usc.edu/toolkit/`), which is available to the public at no cost. Figure A.5 shows an example of motion feature maps (a-d) and the motion conspicuity map (e) for a white bar moving from left to right (f). As expected, $\mathcal{M}_{\rightarrow}$ shows activity at the edges of the bar, while $\mathcal{M}_{\uparrow}$ and $\mathcal{M}_{\downarrow}$ have no activity. The activity in $\mathcal{M}_{\leftarrow}$ is due to aliasing.

The multiscale implementation of the motion detector in a pyramid allows us to detect a large range of speeds. However, this effect is confounded with decreasing spatial resolution for higher levels of the pyramid, leading to difficulties in detecting small, fast moving objects. To decouple speed from spatial resolution, several values for Δx and Δy might be chosen and applied to a pyramid level with sufficient spatial resolution. Furthermore, our model fails to account for the interactions between different motion directions in non-classical receptive fields that were reported by Allman et al. (1985). These interactions would need to be built into the model explicitly.

Our model only detects local motion at various resolutions, equivalent to the spatiotemporal receptive fields in V1. It does not encompass the detection of global motion patterns such as expansion or rotation by areas MT and MST. Tsotsos et al. (2002, 2005) describe detection of such motion patterns as well as mechanisms for attending to them in their Selective Tuning Model.

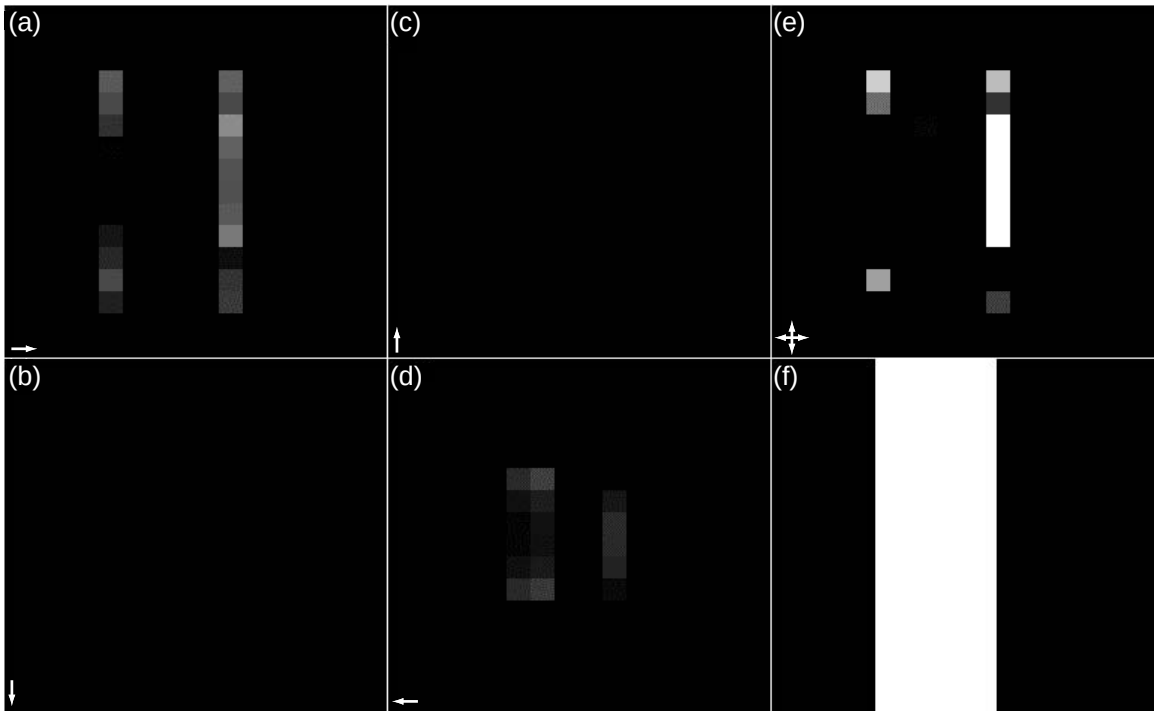

Figure A.5: Feature maps for motion directions right (a), down (b), up (c), left (d), and the motion conspicuity map (e) in response to a rightward moving white bar (f).

A.4 Skin Hue Detection

In chapter 4 we use skin hue as a benchmark for our top-down attention maps because it is known to be a good indicator for the presence of human faces (Darrel et al. 2000). Since we want our model of skin hue to be independent of light intensity, we model it in a simplified color space akin to the CIE color space. If (r, g, b) are the RGB values of a given color pixel, then we compute our (r', g') color coordinates as

$$r' = \frac{r}{r+g+b} \text{ and} \tag{A.11a}$$

$$g' = \frac{g}{r+g+b}. \tag{A.11b}$$

Note that it is not necessary to have a separate value for blue because the blue content of the pixel can be infered from r' and g' at any given light intensity $(r+g+b)$.

We use a simple Gaussian model for skin hue in this color space. For a given color pixel with coordinates $c = (r', g')$, the model's hue response is given by

$$h(c) = \exp\left[-\frac{1}{2}(c-\mu)^T \Sigma^{-1} (c-\mu)\right], \tag{A.12}$$

with $\mu = (\mu_r, \mu_g)$ the center of the distribution and

$$\Sigma = \begin{pmatrix} \sigma_r^2 & \frac{\sigma_r \sigma_g}{\rho} \\ \frac{\sigma_r \sigma_g}{\rho} & \sigma_g^2 \end{pmatrix} \tag{A.13}$$

its covariance matrix with σ_r^2 and σ_g^2 the variances of the r' and g' components, respectively, and ρ their correlation. Substituting eq. A.13 into eq. A.12 yields

$$h(r', g') = \exp\left[-\frac{1}{2}\left(\frac{(r'-\mu_r)^2}{\sigma_r^2} + \frac{(g'-\mu_g)^2}{\sigma_g^2} - \frac{\rho(r'-\mu_r)(g'-\mu_g)}{\sigma_r \sigma_g}\right)\right]. \tag{A.14}$$

To estimate the parameters of the skin hue distribution, we used 1153 color photographs containing a total of 3947 faces from the world wide web[1] and fitted the hue distribution of the faces. The resulting parameters are shown in table A.2. The images used for estimating the skin hue model are a separate set from the set of images used in chapter 4. The images depict humans of many different ages and ethnicities, both female and male. There is a slight bias toward caucasian males, reflecting a general bias of images of humans inthe world wide web. We observed that the skin *hue* does not vary much between different ethnicities, while brightness of the skin shows much more variations.

Table A.2: Parameters of the distribution of skin hue in (r', g') color space.

Parameter	*Value*
μ_r	0.434904
μ_g	0.301983
σ_r	0.053375
σ_g	0.024349
ρ	0.5852

Figure A.6 shows the hue of the training faces and the fitted distribution. An example for applying eq. A.14 to a color image is shown in figure A.7. The skin hue model is implemented as part of the SaliencyToolbox for Matlab (appendix B).

[1] Thanks to Dr. Pietro Perona for providing the images.

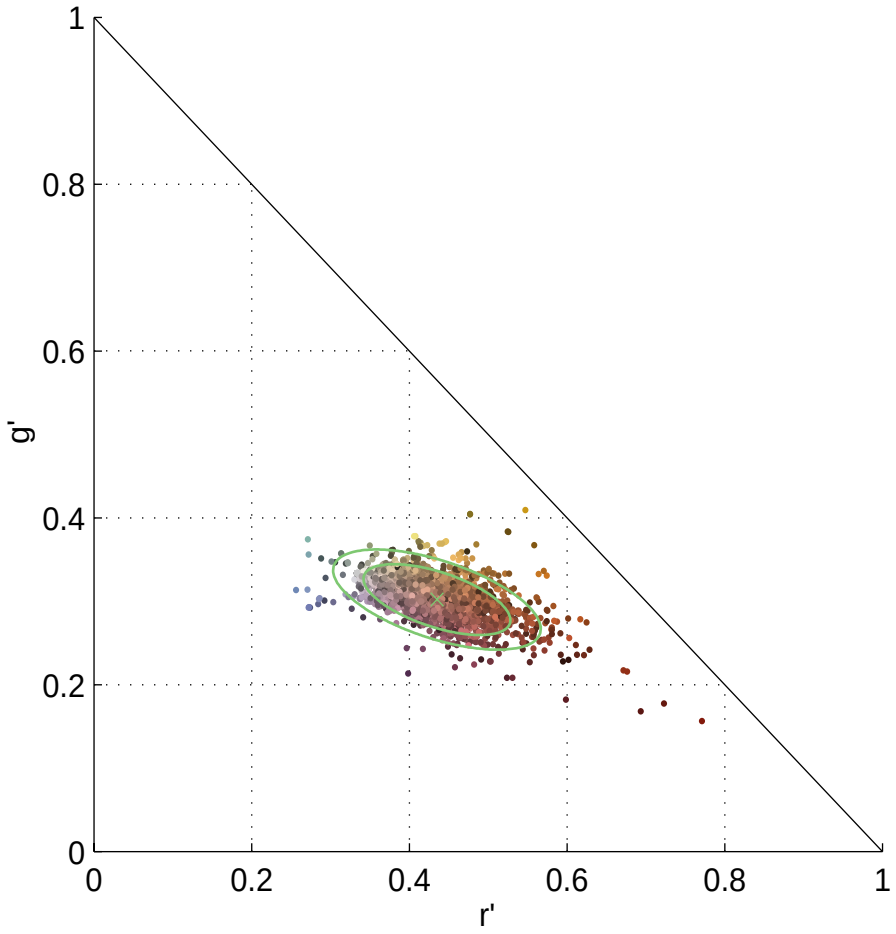

Figure A.6: The Gaussian model for skin hue. The individual training points are derived from 3974 faces in 1153 color photographs. Each dot represents the average hue for one face and is plotted in the color of the face. The green cross represents the mean (μ_r, μ_g), and the green ellipses the 1σ and 2σ intervals of the hue distribution.

Figure A.7: Example of a color image with faces (left) processed with the skin hue model from eq. A.14, using the parameters from table A.2 (right). The color scale on the right reflects how closely hue matches the mean skin hue, marked with a green cross in figure A.6. Note that face regions show high values, but other skin colored regions do as well, e.g. arms and hands or the orange T-shirt of the boy on the right.

Appendix B

The SaliencyToolbox

B.1 Introduction

The SaliencyToolbox is a collection of Matlab functions and scripts for computing the saliency map for an image, for determining the extent of a proto-object as described in chapter 2, and for serially scanning the image with the focus of attention. Being mostly written in Matlab, the code is easily accessible, easy to experiment with, and platform independent.

Major parts of the code are reimplemented from the *iLab Neuromorphic Vision C++ Toolkit* (iNVT) at Laurent Itti's lab at the University of Southern California (`http://ilab.usc.edu/toolkit`). The iNVT code base contains much functionality beyond the actual saliency computations. Unfortunately, its feature richness (contained in 360,000 lines of code) makes the code increasingly difficult to understand for novices. The SaliencyToolbox complements the iNVT code in that it is more compact (about 5,000 lines of code) and easier to understand and experiment with. The SaliencyToolbox only contains the core functionality for attending to salient image regions. Although most time critical processing steps are coded in C++ mex files, processing an image with the SaliencyToolbox in Matlab takes longer than with the iNVT code. Whenever processing speed or feature richness are paramount, the iNVT code should be preferred. For computing the saliency map or attending to salient proto-objects in an image in a transparent and platform independent way, the SaliencyToolbox is a good choice.

The SaliencyToolbox requires a Matlab Release 13 or 14[1] and the Matlab Image Processing Toolbox. Most time critical parts of the code are coded in C++ mex files. Pre-compiled binaries of the mex files are included for Microsoft Windows, Mac OS X, Linux 32 bit Intel/AMD, and Linux 64 bit AMD Opteron. The source code can be compiled on any system with the GNU C compiler gcc (see section B.4 for details).

The SaliencyToolbox is licensed under the GNU General Public License (`http://www.gnu.org/copyleft/gpl.html`). Some portions of the code are covered under two U.S. patent applications.

[1] Other versions might work but were not tested.

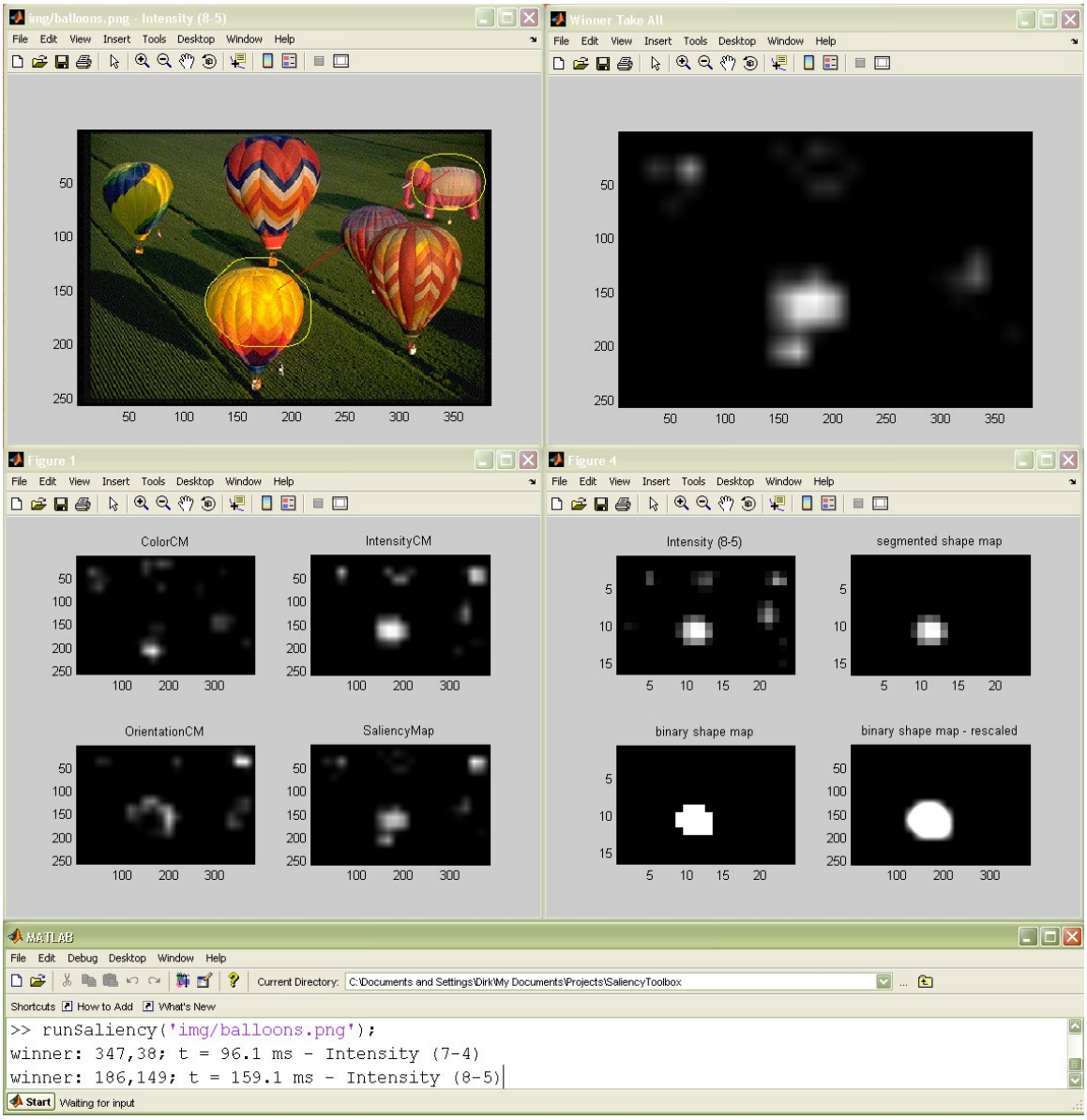

Figure B.1: Screen shot of a typical display while running the SaliencyToolbox.

(Koch and Itti 2001; Rutishauser et al. 2004b). Since the code and the documentation are evolving, please refer to the web site (`http://www.saliencytoolbox.net`) for the most recent version.

B.2 Installation

The code can be downloaded free of charge from `http://www.saliencytoolbox.net`. Unpacking the code creates a directory structure under SaliencyToolbox. Simply add the SaliencyToolbox directory with its subdirectories to your Matlab path:

```
addpath(genpath('<your SaliencyToolbox path>'));
```

If access to the toolbox is desired every time Matlab starts, the above command should be places into your startup.m file, which is located in `~/matlab/startup.m` for Linux, Mac OS X and other Unix flavors, and in the "Start in" directory for your Matlab desktop shortcut under Microsoft Windows.

B.3 Quick Start

In Matlab, change to the SaliencyToolbox directory, then type:

```
runSaliency('img/balloons.png');
```

After a few moments, you should see four figure windows with various intermediate results, and in the Matlab window you will see details about the most salient location, which is also marked in the image (figure B.1). You can now hit "Return" to go to the next most salient location and so forth. To quit, simply enter "q" and press "Return".

If you receive the following fatal error: "MEX file xxx could not be found," then you need to compile the mex files for your system (section B.4).

The `SaliencyToolbox/img` directory contains a few example images. The `runSaliency` function also takes an optional second argument, a `saliencyParams` structure. Start exploring the documentations for `runSaliency`, `defaultSaliencyParams`, and `dataStructures` to get an idea of what is happening. It may be a good idea to make a copy of `runSaliency.m` and start dissecting and adapting it for your purpose.

For more feedback on what is happening at each time step, try the following:

```
declareGlobal;
DEBUG_FID = 1;
runSaliency('img/balloons.png');
```

See documentation for `initializeGlobal`, `declareGlobal`, and `debugMsg` for what is happening here.

B.4 Compilation

Most users do not need to compile the mex files. Binaries for the most common architectures are included with the toolbox. Compilation may become necessary if the binaries for your operating system and CPU combination are not in the `SaliencyToolbox/bin` directory yet. In this case, please send me a note once you have successfully compiled your mex files, and I may include the binaries for your system in the next release. Compilation is also necessary, of course, if you modify the C++ code of the mex files.

B.4.1 Linux, Mac OS X, and other Unix flavors

This requires the GNU gcc compiler, version 3.2.3, if possible. The compiler should be named "gcc-3" and its C++ equivalent "g++-3". Create an alias or link if your compiler is called differently. Check by typing:

```
gcc-3 --version
```

The 3.3 variants in Fedora Core and OS X work as well. Gcc 3.4.x definitely does NOT work for mex files; they will not link correctly at Matlab runtime. Gcc versions before 3.0 will not work because they do not fully implement the standard template library. Gcc 4.x does not appear to work, either.

The `mex` shell script that comes with Matlab needs to be in the executable path. The `mex` scripts of Matlab releases 13 and earlier do not understand the "-cxx" option to signal C++ code; release 14 requires it. Hence, if your Matlab version is R13 or older, you need to edit two lines around line 25 of your `SaliencyToolbox/mex/Makefile` to this:

```
#MEXFLAGS := -cxx
MEXFLAGS :=
```

Now, change into directory `SaliencyToolbox/mex` and type:

```
make
```

This will create the binaries in `SaliencyToolbox/bin`. If you get a message saying that nothing needs to be done, but you are sure that you need to recompile the code, then use this command:

```
make clean all
```

B.4.2 Microsoft Windows

To compile the code under Windows, MinGW (minimalistic GNU for Windows) and MSYS (Minimalistic SYStem) need to be installed. This is free software in the public domain. Follow these steps to install a working environment for compiling mex files (all downloads are available at `http://www.mingw.org/download.shtml`):

(i) Download mingw-runtime-3.8.tar.gz and unpack into a new folder `c:\mingw`.

(ii) Download binutils-2.15.91-20040904-1.tar.gz and unpack into `c:\mingw`.

(iii) Download gcc-3.2.3-20030504-1.tar.gz and unpack into `c:\mingw`. If you are asked if you wish to overwrite some existing files, click on "yes to all".

(iv) Download w32api-3.3.tar.gz and unpack into `c:\mingw`.

(v) Download MSYS-1.0.10.exe and run the installer, install into `c:\msys`.

(vi) During the postinstall, answer "y" on the question if you have mingw, then enter `/c/mingw` as its installation path.

Start your newly installed MSYS environment, which will give you a Unix-like shell, and change the directory to `SaliencyToolbox/mex`. Make sure that the global environment variable `MATLABROOT` is set to the Matlab installation directory, e.g., by typing

```
export MATLABROOT=/c/MATLAB7
```

Now you can compile the code by typing

```
make
```

which creates the Windows `.dll` files in `SaliencyToolbox/bin`. If you get a message saying that nothing needs to be done, but you are sure that you need to recompile the code, then use this command:

```
make clean all
```

B.5 Generating the Documentation

In order to re-create the documentation for the C++ source code for the mex files, you need to have doxygen and graphviz (for the `dot` command) installed and in your executable path. Then change to the `SaliencyToolbox/mex` directory and type:

```
make doc
```

This will create the documentation in `SaliencyToolbox/doc/mexdoc`.

The documentation for the m-files is generated from within Matlab using the m2html toolbox (`http://www.artifact.tk/software/matlab/m2html/`). Make sure that m2html is in your Matlab path, then change to the SaliencyToolbox base directory and type:

```
STBgenerateDoc;
```

This creates the documentation for the m-files in `SaliencyToolbox/doc/mdoc`.

References

E. H. Adelson and J. R. Bergen. Spatiotemporal energy models for the perception of motion. *Journal of the Optical Society of America A*, 2(2):284–299, 1985.

J. Allman, F. Miezin, and E. McGuinness. Direction- and velocity-specific responses from beyond the classical receptive field in the middle temporal visual area (MT). *Perception*, 14(2):105–126, 1985.

A. Allport, E. A. Styles, and S. L. Hsieh. Shifting intentional set – exploring the dynamic control of tasks. In C. Umilta and M. Moscovitch, editors, *Attention and Performance XV*, pages 421–452. MIT Press, Cambridge, MA, 1994.

E. M. Altmann. The preparation effect in task switching: carryover of SOA. *Memory and Cognition*, 32(1):153–163, 2004.

Y. Amit and M. Mascaro. An integrated network for invariant visual detection and recognition. *Vision Research*, 43(19):2073–2088, 2003.

D. H. Ballard. Generalizing the Hough transform to detect arbitrary patterns. *Pattern Recognition*, 13(2):111–122, 1981.

K. Barnard, P. Duygulu, R. Guru, P. Gabbur, and D. Forsyth. The effects of segmentation and feature choice in a translation model of object recognition. In *International Conference on Computer Vision and Pattern Recognition*, 2003.

D. H. Brainard. The psychophysics toolbox. *Spatial Vision*, 10(4):433–436, 1997.

J. Braun. Visual-search among items of different salience – removal of visual-attention mimics a lesion in extrastriate area V4. *Journal of Neuroscience*, 14(2):554–567, 1994.

H. Bülthoff, J. Little, and T. Poggio. A parallel algorithm for real-time computation of optical flow. *Nature*, 337(6207):549–555, 1989.

P. J. Burt and E. H. Adelson. The Laplacian Pyramid as a compact image code. *IEEE Transactions on Communications*, COM-31(4):532–540, 1983.

L. Chelazzi, E. K. Miller, J. Duncan, and R. Desimone. Responses of neurons in macaque area V4 during memory-guided visual search. *Cerebral Cortex*, 11(8):761–72, 2001.

D. Chung, R. Hirata, T. N. Mundhenk, J. Ng, R. J. Peters, E. Pichon, A. Tsui, T. Ventrice, D. Walther, P. Williams, and L. Itti. A new robotics platform for neuromorphic vision: Beobots. In *Lecture Notes in Computer Science*, volume 2525, pages 558–566. Springer, Berlin, Germany, 2002.

J. J. Clark and N. J. Ferrier. Control of visual attention in mobile robots. In *IEEE International Conference on Robotics and Automation*, volume 2, pages 826–831, 1989.

T. Clarke. Robots in the deep. *Nature*, 421(30):468–470, 2003.

C. E. Connor, D. C. Preddie, J. L. Gallant, and D. C. van Essen. Spatial attention effects in macaque area V4. *Journal of Neuroscience*, 17(9):3201–3214, 1997.

T. Darrel, G. Gordon, M. Harville, and J. Woodfill. Integrated person tracking using stereo, color, and pattern detection. *International Journal of Computer Vision*, 37(2):175–185, 2000.

R. De Jong. An intention-activation account of residual switch costs. In S. Monsell and J. Driver, editors, *Control of Cognitive Processes: Attention and Performance XVIII*, pages 357–376. MIT Press, Cambridge, MA, 2000.

G. C. DeAngelis, J. G. Robson, I. Ohzawa, and R. D. Freeman. Organization of suppression in receptive fields of neurons in cat visual cortex. *Journal of Neurophysiology*, 68(1):144–163, 1992.

G. Deco and B. Schürmann. A hierarchical neural system with attentional top-down enhancement of the spatial resolution for object recognition. *Vision Research*, 40(20):2845–2859, 2000.

A. Delorme, G. Richard, and M. Fabre-Thorpe. Ultra-rapid categorisation of natural scenes does not rely on colour cues: a study in monkeys and humans. *Vision Research*, 40(16):2187–2200, 2000.

R. Desimone and J. Duncan. Neural mechanisms of selective visual-attention. *Annual Review of Neuroscience*, 18:193–222, 1995.

S. Dickinson, H. Christensen, J. K. Tsotsos, and G. Olofsson. Active object recognition integrating attention and viewpoint control. *Computer Vision and Image Understanding*, 63(67-3):239–260, 1997.

J. Duncan. Selective attention and the organization of visual information. *Journal of Experimental Psychology: General*, 113(4):501–517, 1984.

J. Duncan. Integrated mechanisms of selective attention. *Current Opinion in Biology*, 7:255–261, 1997.

D. Edgington, D. Walther, K. A. Salamy, M. Risi, R.E. Sherlock, and C. Koch. Automated event detection in underwater video. In *MTS/IEEE Oceans*, San Diego, California, 2003.

R. Egly, J. Driver, and R. D. Rafal. Shifting visual attention between objects and locations: evidence from normal and parietal lesion subjects. *Journal of Experimental Psychology General*, 123(2): 161–177, 1994.

W. Einhäuser, W. Kruse, K. P. Hoffmann, and P. König. Differences of monkey and human overt attention under natural conditions. *Vision Research*, 46(8-9):1194–1209, 2006.

C. W. Eriksen and J. D. St. James. Visual attention within and around the field of focal attention: A zoom lens model. *Perception and Psychophysics*, 40(4):225–240, 1986.

M. Fabre-Thorpe, G. Richard, and S. J. Thorpe. Rapid categorization of natural images by rhesus monkeys. *Neuroreport*, 9(2):303–308, 1998.

T. Fawcett. ROC Graphs: Notes and practical considerations for data mining researchers. *HP Technical Report*, 4, 2003.

L. Fei-Fei, R. VanRullen, C. Koch, and P. Perona. Why does natural scene categorization require little attention? Exploring attentional requirements for natural and synthetic stimuli. *Visual Cognition*, 12(6):893–924, 2005.

R. Fergus, P. Perona, and A. Zisserman. Object class recognition by unsupervised scale-invariant learning. In *International Conference on Computer Vision and Pattern Recognition*, volume 2, pages 264–271, 2003.

D. J. Freedman, M. Riesenhuber, T. Poggio, and E. K. Miller. A comparison of primate prefrontal and inferior temporal cortices during visual categorization. *Journal of Neuroscience*, 23(12):5235–5246, 2003.

S. Frintrop, G. Backer, and E. Rome. Selecting what is important: Training visual attention. In *Proceedings of the 28th German Conference on Artificial Intelligence (KI '05)*, Koblenz, Germany, 2005.

S. P. Gandhi, D. J. Heeger, and G. M. Boynton. Spatial attention affects brain activity in human primary visual cortex. *Proceedings of the National Academy of Sciences of the USA*, 96(6):3314–3319, 1999.

S. Grossberg and R. D. Raizada. Contrast-sensitive perceptual grouping and object-based attention in the laminar circuits of primary visual cortex. *Vision Research*, 40(10-12):1413–1432, 2000.

F. Hamker. The emergence of attention by population-based inference and its role in distributed processing and cognitive control of vision. *Computer Vision and Image Understanding*, 100(1-2): 64–106, 2005a.

F. H. Hamker. The reentry hypothesis: the putative interaction of the frontal eye field, ventrolateral prefrontal cortex, and areas V4, IT for attention and eye movement. *Cerebral Cortex*, 15(4): 431–447, 2005b.

C. J. Harris and M. Stephens. A combined corner and edge detector. In *4th Alvey Vision Conference*, pages 147–151, 1988.

B. Hassenstein and W. Reichardt. Systemtheoretische Analyse der Zeit-, Reihenfolgen und Vorzeichenauswertung bei der Bewegungsperzeption der Rüsselkäfers Chlorophanus. *Zeitschrift für Naturforschung*, 11b:513–524, 1956.

J. B. Hayet, F. Lerasle, and M. Devy. Visual landmark detection and recognition for mobile robot navigation. In *International Conference on Computer Vision and Pattern Recognition*, volume 2, pages 313–318, 2003.

O. Hershler and S. Hochstein. At first sight: a high-level pop out effect for faces. *Vision Research*, 45(13):1707–1724, 2005.

S. Hochstein and M. Ahissar. View from the top: Hierarchies and reverse hierarchies in the visual system. *Neuron*, 36(5):791–804, 2002.

C. P. Hung, G. Kreiman, T. Poggio, and J. J. DiCarlo. Fast readout of object identity from macaque inferior temporal cortex. *Science*, 310(5749):863–866, 2005.

L.M. Hurvich and D. Jameson. An opponent-process theory of color vision. *Psychological Review*, 64:384–404, 1957.

J. Intriligator and P. Cavanagh. The spatial resolution of visual attention. *Cognitive Psychology*, 43 (3):171–216, 2001.

L. Itti. *Models of bottom-up and top-down visual attention.* PhD thesis, California Institute of Technology, 2000.

L. Itti. Quantifying the contribution of lowlevel saliency to human eye movements in dynamic scenes. *Visual Cognition*, 12(6):1093–1123, 2005.

L. Itti and C. Koch. Computational modelling of visual attention. *Nature Reviews Neuroscience*, 2 (3):194–203, 2001a.

L. Itti and C. Koch. Feature combination strategies for saliency-based visual attention systems. *Journal of Electronic Imaging*, 10(1):161–169, 2001b.

L. Itti, C. Koch, and E. Niebur. A model of saliency-based visual attention for rapid scene analysis. *IEEE Transactions on Pattern Analysis and Machine Intelligence*, 20(11):1254–1259, 1998.

M. Jägersand. Saliency maps and attention in scale and spatial coordinates: an information theoretic approach. In *IEEE International Conference on Computer Vision*, pages 195–202, 1995.

A.T. Jersild. Mental set and shift. *Archives of Psychology*, 89:5–82, 1927.

T. Kadir and M. Brady. Scale, saliency and image description. *International Journal of Computer Vision*, 30(2):77–116, 2001.

D. Kahneman and A. Treisman. Changing views of attention and automaticity. In R. Parasuraman and Daviesm D. A., editors, *Varieties of attention*, pages 29–61. Academic Press, New York, 1984.

D. Kahneman, A. Treisman, and B. J. Gibbs. The reviewing of object files: object-specific integration of information. *Cognitive Psychology*, 24(2):175–219, 1992.

R. E. Kalman and R. S. Bucy. New results in linear filtering and prediction theory. *Journal of Basic Engineering*, 83(3):95–108, 1961.

S. Kastner, P. De Weerd, R. Desimone, and L. G. Ungerleider. Mechanisms of directed attention in the human extrastriate cortex as revealed by functional MRI. *Science*, 282(5386):108–111, 1998.

D. Y. Kimberg, G. K. Aguirre, and M. D'Esposito. Modulation of task-related neural activity in task-switching: an fMRI study. *Cognitive Brain Research*, 10(1-2):189–196, 2000.

T. Kirubarajan, Y. Bar-Shalom, and K.R. Pattipati. Multiassignment for tracking a large number of overlapping objects. *IEEE TAES*, 37(1):2–21, 2001.

T. Kleinsorge. Hierarchical switching with two types of judgment and two stimulus dimensions. *Experimental Psychology*, 51(2):145–149, 2004.

C. Koch and L. Itti. Computation of intrinsic perceptual saliency in visual environments, and applications, U.S. patent application 09/912,225, July 23 2001.

C. Koch and S. Ullman. Shifts in selective visual-attention – towards the underlying neural circuitry. *Human Neurobiology*, 4:219–227, 1985.

I. Koch. Sequential task predictability in task switching. *Psychonomic Bulletin and Review*, 12(1): 107–112, 2005.

A. F. Kramer and A. Jacobson. Perceptual organization and focused attention: the role of objects and proximity in visual processing. *Perception and Psychophysics*, 50(3):267–284, 1991.

D. K. Lee, L. Itti, C. Koch, and J. Braun. Attention activates winner-take-all competition among visual filters. *Nature Neuroscience*, 2(4):375–381, 1999.

S. I. Lee and S. Y. Lee. Top-down attention control at feature space for robust pattern recognition. In *Biologically-Motivated Computer Vision*, Seoul, Korea, 2000.

S. Y. Lee. Top-down selective attention for robust perception of noisy and confusing patterns. In *International Conference on Artificial Intelligence and Soft Computing*, Zakopane, Poland, 2004.

G. E. Legge, D. G. Pelli, G. S. Rubin, and M. M. Schleske. The psychophysics of reading. *Vision Research*, 25(2):239–252, 1985.

F. F. Li, R. VanRullen, C. Koch, and P. Perona. Rapid natural scene categorization in the near absence of attention. *Proceedings of the National Academy of Sciences of the USA*, 99(14):9596–9601, 2002.

N. K. Logothetis, J. Pauls, H. H. Bülthoff, and T. Poggio. View-dependent object recognition by monkeys. *Current Biology*, 4(5):401–414, 1994.

D. G. Lowe. Towards a computational model for object recognition in IT cortex. In *Biologically Motivated Computer Vision*, pages 20–31, 2000.

D. G. Lowe. Distinctive image features from scale-invariant keypoints. *International Journal of Computer Vision*, 60(2):91–110, 2004.

D. G. Lowe. Object recognition from local scale-invariant features. In *International Conference on Computer Vision*, pages 1150–1157, 1999.

S. J. Luck, L. Chelazzi, S. A. Hillyard, and R. Desimone. Neural mechanisms of spatial selective attention in areas V1, V2, and V4 of macaque visual cortex. *Journal of Neurophysiology*, 77(1): 24–42, 1997.

R. Manduchi, P. Perona, and D. Shy. Efficient deformable filter banks. *IEEE Transactions on Signal Processing*, 46(4):1168–1173, 1998.

D. Martin, C. Fowlkes, and J. Malik. Learning to detect natural image boundaries using local brightness, color and texture cues. *IEEE Transactions on Pattern Analysis and Machine Intelligence*, 26(5):530–549, 2004.

C. J. McAdams and J. H. R. Maunsell. Attention to both space and feature modulates neuronal responses in macaque area V4. *Journal of Neurophysiology*, 83(3):1751–1755, 2000.

C. J. McAdams and R. C. Reid. Attention modulates the responses of simple cells in monkey primary visual cortex. *Journal of Neuroscience*, 25(47):11023–11033, 2005.

N. Meiran. Modeling cognitive control in task-switching. *Psychological Research – Psychologische Forschung*, 63(3-4):234–249, 2000.

N. Meiran. Reconfiguration of processing mode prior to task performance. *Journal of Experimental Psychology – Learning Memory and Cognition*, 22(6):1423–1442, 1996.

E. Mellinger, A. Pearce, and M. Chaffey. Distributed multiplexers for an ROV control and data system. In *MTS/IEEE Oceans*, Brest, France, 1994.

F. Miau and L. Itti. A neural model combining attentional orienting to object recognition: Preliminary explorations on the interplay between where and what. In *IEEE Engineering in Medicine and Biology Society*, 2001.

F. Miau, C. Papageorgiou, and L. Itti. Neuromorphic algorithms for computer vision and attention. In *SPIE 46 Annual International Symposium on Optical Science and Technology*, volume 4479, pages 12–23, 2001.

R. Milanese, H. Wechsler, S. Gill, J.-M. Bost, and T. Pun. Integration of bottom-up and top-down cues for visual attention using non-linear relaxation. In *International Conference on Computer Vision and Pattern Recognition*, pages 781–785, 1994.

S. Monsell. Task switching. *Trends in Cognitive Sciences*, 7(3):134–140, 2003.

C. M. Moore, S. Yantis, and B. Vaughan. Object-based visual selection. *Psychological Science*, 9 (2):104–110, 1998.

J. Moran and R. Desimone. Selective attention gates visual processing in the extrastriate cortex. *Science*, 229(4715):782–784, 1985.

G. Mori, X. Ren, A. A. Efros, and J. Malik. Recovering human body configurations: Combining segmentation and recognition. In *International Conference on Computer Vision and Pattern Recognition*, 2004.

B. C. Motter. Neural correlates of attentive selection for color or luminance in extrastriate area V4. *Journal of Neuroscience*, 14(4):2178–2189, 1994.

V. Navalpakkam and L. Itti. Modeling the influence of task on attention. *Vision Research*, 45(2): 205–231, 2005.

J. B. Newman and D. Stakes. Tiburon, development of an ROV for ocean science research. In *Proceedings MTS/IEEE Oceans*, Brest, France, 1994.

D. H. O'Connor, M. M. Fukui, M. A. Pinsk, and S. Kastner. Attention modulates responses in the human lateral geniculate nucleus. *Nature Neuroscience*, 5(11):1203–1209, 2002.

A. Oliva, A. Torralba, M.S. Castelhano, and J.M. Henderson. Top-down control of visual attention in object detection. In *International Conference on Image Processing*, 2003.

B. A. Olshausen, C. H. Anderson, and D. C. Van Essen. A neurobiological model of visual attention and invariant pattern recognition based on dynamic routing of information. *Journal of Neuroscience*, 13(11):4700–19, 1993.

R. J. Peters, A. Iyer, L. Itti, and C. Koch. Components of bottom-up gaze allocation in natural images. *Vision Research*, 45(18):2397–2416, 2005.

M. I. Posner. Orienting of attention. *Quarterly Journal of Experimental Psychology*, 32(1):3–25, 1980.

M. C. Potter and E. I. Levy. Recognition memory for a rapid sequence of pictures. *Journal of Experimental Psychology*, 81(1):10–5, 1969.

R. D. Raizada and S. Grossberg. Context-sensitive bindings by the laminar circuits of V1 and V2: A unified model of perceptual grouping, attention, and orientation contrast. *Visual Cognition*, 8: 431–466, 2001.

R. P. N. Rao. Visual attention during recognition. In *Advances in Neural Information Processing*, 1998.

R. A. Rensink, J. K. Oregan, and J. J. Clark. To see or not to see: The need for attention to perceive changes in scenes. *Psychological Science*, 8(5):368–373, 1997.

J. H. Reynolds, T. Pasternak, and R. Desimone. Attention increases sensitivity of V4 neurons. *Neuron*, 26(3):703–714, 2000.

M. Riesenhuber and T. Poggio. Are cortical models really bound by the "binding problem"? *Neuron*, 24(1):87–93, 111–125, 1999a.

M. Riesenhuber and T. Poggio. Hierarchical models of object recognition in cortex. *Nature Neuroscience*, 2(11):1019–1025, 1999b.

B. H. Robison. The coevolution of undersea vehicles and deep-sea research. *Marine Technology Society Journal*, 33:69–73, 2000.

P. R. Roelfsema, V. A. F. Lamme, and H. Spekreijse. Object-based attention in the primary visual cortex of the macaque monkey. *Nature*, 395(6700):376–381, 1998.

R. D. Rogers and S. Monsell. Costs of a predictable switch between simple cognitive tasks. *Journal of Experimental Psychology – General*, 124(2):207–231, 1995.

E. Rosen. Face representation in cortex: Studies using a simple and not so special model, CBCL Paper #228/AI Memo #2003-010. Technical report, Massachusetts Institute of Technology, June 2003.

A. Rosenfeld and J. L. Pfaltz. Sequential operations in digital picture processing. *Journal of the Association for Computing Machinery*, 13:471–494, 1966.

F. Rothganger, S. Lazebnik, C. Schmid, and J. Ponce. 3D object modeling and recognition using affine-invariant patches and multi-view spatial constraints. In *International Conference on Computer Vision and Pattern Recognition*, volume 2, pages 272–277, 2003.

H. Rowley, S. Baluja, and T. Kanade. Neural network-based face detection. *IEEE Transactions on Pattern Analysis and Machine Intelligence*, 20(1):23–38, 1998.

D. L. Ruderman. Origins of scaling in natural images. *Vision Research*, 37(23):3385–98, 1997.

M. F. Rushworth, T. Paus, and P. K. Sipila. Attention systems and the organization of the human parietal cortex. *Journal of Neuroscience*, 21(14):5262–5271, 2001.

M. F. S. Rushworth, R. E. Passingham, and A. C. Nobre. Components of attentional set-switching. *Experimental Psychology*, 52(2):83–98, 2005.

U. Rutishauser, D. Walther, C. Koch, and P. Perona. Is attention useful for object recognition? In *International Conference on Computer Vision and Pattern Recognition*, volume 2, pages 37–44, 2004a.

U. Rutishauser, D. Walther, C. Koch, and P. Perona. A system and method for attentional selection, U.S. patent application 10/866,311, June 10 2004b.

I. A. Rybak, V. I. Gusakova, A. V. Golovan, L. N. Podladchikova, and N. A. Shevtsova. A model of attention-guided visual perception and recognition. *Vision Research*, 38(15-16):2387–2400, 1998.

J. Saarinen and B. Julesz. The speed of attentional shifts in the visual field. *Proceedings of the National Academy of Sciences of the USA*, 88(5):1812–1814, 1991.

D. Sagi and B. Julesz. Enhanced detection in the aperture of focal attention. *Nature*, 321:693–695, 1986.

K. Schill, E. Umkehrer, S. Beinlich, G. Krieger, and C. Zetzsche. Scene analysis with saccadic eye movements: Top-down and bottom-up modeling. *Journal of Electronic Imaging*, 10(1):152–160, 2001.

C. Schmid. A structured probabilistic model for recognition. In *International Conference on Computer Vision and Pattern Recognition*, volume 2, pages 485–490, 1999.

H. Schneiderman and T. Kanade. A statistical method for 3D object detection applied to faces and cars. In *International Conference on Computer Vision and Pattern Recognition*, pages 746–751, 2000.

T. Serre and T. Poggio. Standard model v2.0: How visual cortex might learn a universal dictionary of shape components [abstract]. *Journal of Vision*, 5(8):742a, 2005.

T. Serre, M. Kouh, C. Cadieu, U. Knoblich, G. Kreiman, and T. Poggio. A theory of object recognition: computations and circuits in the feedforward path of the ventral stream in primate visual cortex, CBCL Paper #259/AI Memo #2005-036. Technical report, Massachusetts Institute of Technology, 2005a.

T. Serre, L. Wolf, and T. Poggio. Object recognition with features inspired by visual cortex. In *IEEE International Conference on Computer Vision and Pattern Recognition*, volume 2, pages 994–1000, San Diego, CA, 2005b.

D. L. Sheinberg and N. K. Logothetis. Noticing familiar objects in real world scenes. *Journal of Neuroscience*, 21(4):1340–1350, 2001.

J. Shi and J. Malik. Normalized cuts and image segmentation. *IEEE Transactions on Pattern Analysis and Machine Intelligence*, 22(8):888–905, 2000.

S. Shomstein and S. Yantis. Object-based attention: sensory modulation or priority setting? *Perception and Psychophysics*, 64(1):41–51, 2002.

G. L. Shulman and J. Wilson. Spatial frequency and selective attention to spatial location. *Perception*, 16(1):103–111, 1987.

E. P. Simoncelli and W. T. Freeman. The steerable pyramid: a flexible architecture for multi-scale derivative computation. In *International Conference on Image Processing*, 1995.

D. J. Simons and D. T. Levin. Failure to detect changes to people during a real-world interaction. *Psychonomic Bulletin and Review*, 5(4):644–649, 1998.

D. J. Simons and R. A. Rensink. Change blindness: past, present, and future. *Trends in Cognitive Sciences*, 9(1):16–20, 2005.

M. H. Sohn, S. Ursu, J. R. Anderson, V. A. Stenger, and C. S. Carter. The role of prefrontal cortex and posterior parietal cortex in task switching. *Proceedings of the National Academy of Sciences of the USA*, 97(24):13448–13453, 2000.

A. Spector and I. Biederman. Mental set and mental shift revisited. *American Journal of Psychology*, 89(4):669–679, 1976.

H. Spitzer, R. Desimone, and J. Moran. Increased attention enhances both behavioral and neuronal performance. *Science*, 240(4850):338–340, 1988.

P. Sudevan and D. A. Taylor. The cueing and priming of cognitive operations. *Journal of Experimental Psychology – Human Perception and Performance*, 13(1):89–103, 1987.

Y. Sun and R. Fisher. Object-based visual attention for computer vision. *Artificial Intelligence*, 20 (11):77–123, 2003.

S. Thorpe, D. Fize, and C. Marlot. Speed of processing in the human visual system. *Nature*, 381 (6582):520–522, 1996.

S. Thorpe, A. Delorme, and R. Van Rullen. Spike-based strategies for rapid processing. *Neural Network*, 14(6-7):715–725, 2001.

A. Torralba, K. Murphy, and W. Freeman. Sharing features: efficient boosting procedures for multiclass object detection. In *IEEE International Conference on Computer Vision and Pattern Recognition*, Washington, DC, 2004.

A. M. Treisman and G. Gelade. A feature-integration theory of attention. *Cognitive Psychology*, 12 (1):97–136, 1980.

J. K. Tsotsos, S. M. Culhane, W. Y. K. Wai, Y. H. Lai, N. Davis, and F. Nuflo. Modeling visual-attention via selective tuning. *Artificial Intelligence*, 78:507–545, 1995.

J. K. Tsotsos, M. Pomplun, Y. Liu, J. C. Martinez-Trujillo, and E. Simine. Attending to motion: Localizing and classifying motion patterns in image sequences. In *Lecture Notes in Computer Science*, volume 2525, pages 439–452. Springer, Berlin, Germany, 2002.

J. K. Tsotsos, Y. Liu, J. C. Martinez-Trujillo, M. Pomplun, E. Simine, and K. Zhou. Attending to visual motion. *Computer Vision and Image Understanding*, 100(1-2):3–40, 2005.

R. VanRullen. On second glance: Still no high-level pop-out effect for faces (in press). *Vision Research*, 2005.

V. N. Vapnik. *Statistical Learning Theory.* John Wiley, New York, NY, 1998.

VARS. Video annotation and reference system: http://www.mbari.org/vars/, 2005.

T. Vetter and V. Blanz. A morphable model for the synthesis of 3D faces. In *SIGGRAPH*, pages 187–194, 1999.

P. Viola and M. J. Jones. Robust real-time face detection. *International Journal of Computer Vision*, 57(2):137–154, 2004.

G. Wagner and R. M. Boynton. Comparison of four methods of heterochromatic photometry. *Journal of the Optical Society of America*, 62(12):1508–1515, 1972.

D. Walther and D. Edgington. The art of seeing jellies. *The Neuromorphic Engineer*, 1:6, 2004.

D. Walther, L. Itti, M. Riesenhuber, T. Poggio, and C. Koch. Attentional selection for object recognition – a gentle way. In *Lecture Notes in Computer Science*, volume 2525, pages 472–479. Springer, Berlin, Germany, 2002a.

D. Walther, M. Riesenhuber, T. Poggio, L. Itti, and C. Koch. Towards an integrated model of saliency-based attention and object recognition in the primate's visual system [abstract]. *Journal of Cognitive Neuroscience*, B14 Suppl. S:46–47, 2002b.

D. Walther, D. R. Edgington, and C. Koch. Detection and tracking of objects in underwater video. In *IEEE International Conference on Computer Vision and Pattern Recognition*, volume 1, pages 544–549, Washington, DC, 2004a.

D. Walther, U. Rutishauser, C. Koch, and P. Perona. On the usefulness of attention for object recognition. In *Workshop on Attention and Perfromance in Computational Vision*, pages 96–103, 2004b.

D. Walther, U. Rutishauser, C. Koch, and P. Perona. Selective visual attention enables learning and recognition of multiple objects in cluttered scenes. *Computer Vision and Image Understanding*, 100(1-2):41–63, 2005a.

D. Walther, T. Serre, T. Poggio, and C. Koch. Modeling feature sharing between object detection and top-down attention [abstract]. *Journal of Vision*, 5(8):1041a, 2005b.

D. Walther, L. Fei-Fei, and C. Koch. Measuring the cost of deploying top-down visual attention (submitted). 2006.

M. Weber, M. Welling, and P. Perona. Unsupervised learning of models for recognition. In *European Conference on Computer Vision*, volume 1842, pages 18–32, 2000.

J. M. Wolfe and T. S. Horowitz. What attributes guide the deployment of visual attention and how do they do it? *Nature Reviews Neuroscience*, 5(6):495–501, 2004.

J. M. Wolfe, T. S. Horowitz, N. Kenner, M. Hyle, and N. Vasan. How fast can you change your mind? The speed of top-down guidance in visual search. *Vision Research*, 44(12):1411–1426, 2004.

N. Yeung, L. E. Nystrom, J. A. Aronson, and J. D. Cohen. Between-task competition and cognitive control in task switching. *Journal of Neuroscience*, 26(5):1429–1438, 2006.

P. Zarchan and H. Musoff. *Fundamentals of Kalman filtering: a practical approach.* Progress in astronautics and aeronautics. American Institute of Aeronautics and Astronautics, Inc., 2000.